Western Graduate&PostdoctoralStudies

Western University

Scholarship@Western

Electronic Thesis and Dissertation Repository

8-24-2023 11:30 AM

Visual Cortical Traveling Waves: From Spontaneous Spiking Populations to Stimulus-Evoked Models of Short-Term Prediction

Gabriel B. Benigno, *The University of Western Ontario*

Supervisor: Muller, Lyle, *The University of Western Ontario*

A thesis submitted in partial fulfillment of the requirements for the Doctor of Philosophy degree in Applied Mathematics

© Gabriel B. Benigno 2023

Follow this and additional works at: https://ir.lib.uwo.ca/etd

Part of the Computational Neuroscience Commons

Recommended Citation

Benigno, Gabriel B., "Visual Cortical Traveling Waves: From Spontaneous Spiking Populations to Stimulus-Evoked Models of Short-Term Prediction" (2023). *Electronic Thesis and Dissertation Repository*. 9607.
https://ir.lib.uwo.ca/etd/9607

This Dissertation/Thesis is brought to you for free and open access by Scholarship@Western. It has been accepted for inclusion in Electronic Thesis and Dissertation Repository by an authorized administrator of Scholarship@Western. For more information, please contact wlswadmin@uwo.ca.

Abstract

Thanks to recent advances in neurotechnology, waves of activity sweeping across entire cortical regions are now routinely observed. Moreover, these waves have been found to impact neural responses as well as perception, and the responses themselves are found to be structured as traveling waves. How exactly do these waves arise? Do they confer any computational advantages? These traveling waves represent an opportunity for an expanded theory of neural computation, in which their dynamic local network activity may complement the moment-to-moment variability of our sensory experience.

This thesis aims to help uncover the origin and role of traveling waves in the visual cortex through three Works. In Work 1, by simulating a network of conductance-based spiking neurons with realistically large network size and synaptic density, distance-dependent horizontal axonal time delays were found to be important for the widespread emergence of spontaneous traveling waves consistent with those in vivo. Furthermore, these waves were found to be a dynamic mechanism of gain modulation that may explain the in-vivo result of their modulation of perception. In Work 2, the Kuramoto oscillator model was formulated in the complex domain to study a network possessing distance-dependent time delays. Like in Work 1, these delays produced traveling waves, and the eigenspectrum of the complex-valued delayed matrix, containing a delay operator, provided an analytical explanation of them. In Work 3, the model from Work 2 was adapted into a recurrent neural network for the task of forecasting the frames of videos, with the question of how such a biologically constrained model may be useful in visual computation. We found that the wave activity emergent in this network was helpful, as they were tightly linked with high forecast performance, and shuffle controls revealed simultaneous abolishment of both the waves and performance.

All together, these works shed light on the possible origins and uses of traveling waves in the visual cortex. In particular, time delays profoundly shape the spatiotemporal dynamics into traveling waves. This was confirmed numerically (Work 1) and analytically (Work 2). In Work 3, these waves were found to aid in the dynamic computation of visual forecasting.

Lay summary

The brain is organized into distinct regions of neurons. Within a single such region, the neurons connect to one another intricately, forming a web-like network called a recurrent network. Through our senses, such as vision, these recurrent networks receive stimulation from the outside world, and use this stimulation to help the organism execute meaningful actions, such as movement. Exactly how the neurons in a recurrent network orchestrate, however, is unclear. Often, the electrical neural activity is observed to show waves traveling across the recurrent network, reminiscent of turbulent water waves that wash up on shore. It is unknown exactly how these traveling waves arise and how useful they are.

In Work 1, large computer simulations of a recurrent network were performed. The results showed that a crucial component to include in the simulation is the communication transmission delays between neuron pairs. With these delays included, the simulated electrical neural activity in the network exhibited traveling waves that agreed with real biological recordings, thereby shedding light on the potential origins of such waves in the brain.

In Work 2, a mathematical description of these waves was sought, since mathematical descriptions permit the deepest understanding of physical phenomena. For this purpose, the Kuramoto model was used. The Kuramoto model is a simple yet powerful mathematical model capable of describing traveling waves. This model included time delays similar to those in Work 1. Thus, a mathematical understanding of traveling waves that emerge from delayed recurrent networks was gained.

In Work 3, we asked how traveling waves in the visual part of brain could help in making predictions. To answer this, we used networks similar to the ones in the prior two Works, which are known to cause traveling waves. We then stimulated the network with frames of a movie, and tasked the network with forecasting what the future movie frames might look like. The network was able to learn how to predict these movies. Successful predictions were tightly linked with traveling waves, thereby supporting that these waves are useful for visual prediction in the brain.

Co-authorship statement

In Work 1 (Chapter 2), I share co-first authorship with Zac Davis and Charlee Fletterman. In a preliminary version of the manuscript, Fletterman and Lyle Muller (the last author) wrote the source code and performed the analyses for a one-dimensional version of the featured two-dimensional network. I am responsible for writing the code for the two-dimensional network. Davis and I completed the corresponding simulations and analyses.

In Work 2 (Chapter 3), I share co-first authorship with Roberto Budzinski and Tung Nguyen. Budzinski and Nguyen conducted the mathematical analyses while I performed extensive simulations and analyses of the Human Connectome Project tractography data (Figure 4 of Chapter 3; and unpublished results including grid searches of the parameter space).

In Work 3 (Chapter 4), I am the sole first author while Lyle Muller is the sole last author. Lyle Muller and I performed the conceptualization, analysis, investigation, and writing of the original draft. Methodological and editing contributions were given by the remaining authors (Roberto Buzinski, Zac Davis, and John Reynolds), while supervision was given by both Lyle Muller and John Reynolds.

Acknowledgements

Science is a team effort. Without the collaborations and contributions from my team, none of the work in this thesis would be possible. Personally, this includes my friends and family. Professionally, this includes my lab-mates; collaborating investigators; and Lyle, my supervisor. Certainly, these two sets have a nonempty intersection, and the past four years have been some of my best. I'm grateful for the memories, experiences, and lessons learned, and I thank everyone for having me on the team.

Contents

Abstract ii

Lay Summary iii

Co-authorship statement iv

Acknowledgements v

Contents vi

1 Introduction 1

2 Spontaneous traveling waves emerge from horizontal fiber time delays and are asynchronous-irregular 4

3 Analytical prediction of spatiotemporal patterns in oscillator networks with distance-dependent time delays 32

4 Waves traveling over a map of visual space can ignite short-term predictions of sensory input 46

5 Discussion 64

- 5.1 Distance-dependent delays induce spontaneous and evoked traveling waves . 64
- 5.2 Spontaneous cortical traveling waves are sparse and may be a dynamic mechanism of gain modulation 65
- 5.3 Evoked traveling waves may enable short-term prediction in individual visual cortical areas 66
- 5.4 Conclusion 67

1 | Introduction

A well accepted hypothesis in computational neuroscience is that cognition emerges from the collective interaction of many neurons networked together in the brain. Considering the neuron as the atomic unit of cognition, the brain may then be thought of as a high-dimensional dynamical system in which the membrane potential of each neuron comprises a separate dimension. The dynamics of neural activity in such a network are called *spatiotemporal dynamics*, reflecting that the neural activity varies in both space and time. It is thus cardinal to understand both the origins and mechanisms of spatiotemporal dynamics in the brain to arrive at a systematic understanding of cognition.

The origins of dynamics in neural networks are intricate (Destexhe et al., 2003). At any given moment in time, a neuron's membrane potential depends on all the synaptic inputs it receives from other neurons. The magnitude of these synaptic inputs is proportional to the number of action potentials fired by the presynaptic neuron. Thus, the postsynaptic membrane potential may be weakly or strongly modulated. Synaptic inputs may be excitatory or inhibitory, meaning they stereotypically increase or decrease the postsynaptic membrane potential, respectively. Furthermore, the overall conductance and current of the postsynaptic neuron depends on the synaptic input, thereby adding another source of variability. All together, the postsynaptic neuron then "spikes" (fires an action potential) if its membrane potential exceeds a threshold. These outgoing spikes are responsible for synaptic inputs to other neurons. At the network level, the complex dynamics of individual neurons combine via immense recurrent connectivity to give rise to especially nontrivial and complex spatiotemporal dynamics.

The activity of cortical neurons is highly variable with respect to spontaneous activity as well as responses to the exact same stimulus. The sources of this variability have been the subject of study for the past several decades. One potential source is the spike-generating mechanism, but Mainen and Sejnowski showed that spike timing is highly reliable *in vitro*, given realistic input current (Mainen and Sejnowski, 1995). Rather, neural variability is generally considered to arise in neural circuits predominantly from the dense synaptic input to individual neurons, which fluctuate from moment to moment. These fluctuations are well explained by two related sources. First, there is an approximate balance between excitatory and inhibitory synaptic inputs (Brunel, 2000). Second, the large barrage of spikes impinging on postsynaptic neurons in neocortex renders conductances to generally remain high, making membrane potential fluctuations mostly just below threshold (the so-called high-conductance state, Destexhe et al., 2003), and excursions in this balance toward threshold lead to spiking. Hence, transient disruptions of the balanced state from changes in the relative proportion of excitatory and inhibitory input (E-I balance) can modulate spiking activity. For example, such dynamics of E-I balance have been found to influence network oscillations (Brunel and Wang, 2003; Atallah and Scanziani, 2009), and E-I shifts can act as a precise mechanism for modulating the membrane potential of individual neurons, possibly subserving neural coding (Denève and Machens, 2016). The mechanisms underlying these shifts in E-I balance are still unresolved, however. Broadly, excursions from the balanced high-conductance state have been postulated to be driven by stochasticity (Shadlen and Newsome, 1998) or by deterministic yet complex dynamics (Van Vreeswijk and Sompolinsky, 1996; Vogels and Abbott, 2005). In the former case of stochastic neural variability, neural coding has been hypothesized to follow a rate code, where local populations of tightly coupled neurons (such as cortical columns) average their spiking activity into stable and reproducible instantaneous firing rates (Shadlen and Newsome, 1998).

Recent technologies like high-density electrode arrays (Jun et al., 2017) and optical imaging (Demas et al., 2021) can directly record neural activity from hundreds to thousands of points simultaneously in the brains of awake, behaving mammals, and these numbers are quickly increasing. These recordings reveal dynamics possessing salient spatiotemporal structure across neural populations, and on the single-trial level. Perhaps the most intriguing and curious example is waves of neural activity that travel across entire regions of cortex at the level of individual trials in awake, behaving mammals. These traveling waves have recently been observed as part of spontaneous cortical activity that impacts evoked activity and perception (Davis et al., 2020). Since spontaneous traveling waves are a phenomenon apparent at the spatial scale of the entire network, their effect on perception challenges existing theories about neural processing at the level of individual neurons, in which different neurons are posited to possess different specialties with respect to the kind of stimulus (Hubel and Wiesel, 1959). Furthermore, the mechanisms behind and roles of spontaneous traveling waves are active areas of research. Similarly, traveling waves have also recently been observed in the activity of evoked responses (Muller et al., 2014), and their origin and computational role also remain unclear.

This thesis reports on three contributions to the understanding of traveling waves in the visual cortex of the brain.

In **Work 1 (Chapter 2)**, my coauthors and I employed a high-resolution, conductance-based spiking network model to investigate the spontaneous activity patterns that emerge under biologically constrained circuit motifs (Davis et al., 2021). We found that, with realistic synaptic density, and in networks on the order of millimeters (containing up to one million neurons), the effects of local connectivity and distance-dependent time delays become meaningful, resulting in "sparsely spiking" spontaneous traveling waves that statistically agree with those observed in vivo (Davis et al., 2020) and with the asynchronous-irregular spiking regime that is known to describe spontaneous cortical activity (El Boustani et al., 2007). Lastly, we show how the high-conductance state associated with the wave activity explains a recent experimental result of traveling waves impacting perceptual sensitivity across the entire marmoset area MT (Davis et al., 2020), and propose it as a mechanism of gain modulation (Chance et al., 2002).

Work 2 (Chapter 3) makes an abstraction relative to Work 1 (Chapter 2), using a network of coupled nonlinear oscillators possessing distance-dependent time delays. Such systems are reminiscent of networked neural systems as they exhibit broadband fluctuations, self-organization, and possess heterogeneous time delays. Using a novel complex-valued formulation of the equation of motion, we obtained a delay operator whose eigenmodes predict the individual traveling waves in the network. Notably, this result allows for such predictions at the level of individual realizations of the network rather than averages of realizations, and was successfully applied to tractography data from the Human Connectome Project.

In **Work 3 (Chapter 4)**, we studied a model of stimulus-evoked traveling waves in a single visual cortical area, and asked how such a system might perform short-term prediction of naturalistic visual inputs (Benigno et al., 2023). We leveraged the analytical insight gained about traveling waves from Work 2, and studied these dynamics under a formulation of a single-layer recurrent neural network. Following training of the network, traveling waves emerge in response to a few input movie frames. These waves facilitate good predictions several frames into the future due only to the intrinsic network state. After shuffling the recurrent connections responsible for the waves and retraining the network, both the traveling waves and prediction performance are lost. These results suggest that traveling waves may be integral in the visual system for processing spatiotemporal inputs represented on dynamic spatial maps.

2 Spontaneous traveling waves emerge from horizontal fiber time delays and are asynchronous-irregular

In the visual cortex, the spontaneous activity of the neurons displays a high degree of variability. This variability is believed to originate from the synaptic inputs in the highly recurrent networks (Destexhe et al., 2003). Although a time series recording at an individual location in the network appears stochastic (Shadlen and Newsome, 1994), simultaneous recordings taken across the network show that the same time series can belong to spatiotemporal dynamics structured as waves traveling across the entire area of the cortex; however, these spontaneous traveling waves were initially only observed while the subject was anesthetized (Arieli et al., 1996; Kenet et al., 2003; Tsodyks et al., 1999). During wakefulness, neural fluctuations are higher in frequency and lower in amplitude (Destexhe et al., 1999), rendering the experimental detection of spontaneous traveling waves in this state more challenging. Lastly, stimulus onset reduces variability in spatiotemporal dynamics (Churchland et al., 2010), and spontaneous traveling waves had been hypothesized to play a minor part in a network's response to stimulus (Sato et al., 2012).

More recently, spontaneous traveling waves have been shown to be present during wakefulness. Moreover, their presence has been shown to impact both the extent of stimulus-evoked response and the visual perception of the subject (Davis et al., 2020). Yet, their mechanistic origins were uncharacterized, and furthermore, it was unclear how their spatiotemporal structure could be reconciled with the low-correlation asynchronous-irregular spiking regime known to pervade cortex during wakefulness (El Boustani et al., 2007). Since the observed propagation speeds in the spontaneous traveling waves in Davis et al., 2020 agree with the measured axonal conduction speeds of unmyelinated horizontal fibres in layer 2/3 (Bringuier et al., 1999; Girard et al., 2001; González-Burgos et al., 2000), we asked whether the spikes traveling along these fibres are a potential source of these waves. To answer this question, we conducted a study of a large network of spiking neurons representing a patch of neocortex. Specifically, we explored this network model at a myriad of physiologically relevant densities of neurons, connection probabilities that depend on distance, balances of excitation and inhibition, and values of synaptic conductance. Notably, these networks possessed time delays of spike propagation proportional to the distance between the synaptic pair of neurons, representing time delays from unmyelinated horizontal axonal fibers. These delays were found to be responsible for the traveling-wave dynamics observed in the model, which agreed with the traveling waves found in vivo. Furthermore, these spontaneous traveling waves were robustly present across the parameter space in this model, and the spatiotemporal dynamics simultaneously exhibited asynchronous-irregular activity.

A priori, the presence of these traveling waves may seem to give rise to spatial correlations in the network that (1) violate the asynchronous-irregular regime of spontaneous waking cortex and (2) have been shown to be detrimental to perception (Nandy et al., 2019). From a coding perspective, spatial correlations of spiking activity may impair perception by limiting the expressibility of the neural system since correlated variability imposes a redundancy on the network representation (Huang et al., 2022). The present model provides an explanation for why traveling waves need not induce correlations in spiking activity. Consistent with the multi-unit recordings in visual cortex of the marmoset, the results here show that individual neurons possessed low probabilities of spiking, despite the presence of waves in the network. Hence, the waves are referred to as sparse waves. In contrast, smaller-scale network models produce dense waves in which individual neurons have high probability of spiking as the wave goes past. Thus, sparse traveling waves can propagate across whole regions of cortex without appreciably increasing spatial correlations at the individual-neuron scale, thereby respecting the asynchronous-irregular spiking regime in local cortical neighbourhoods.

nature COMMUNICATIONS

ARTICLE

https://doi.org/10.1038/s41467-021-26175-1 OPEN

Check for updates

Spontaneous traveling waves naturally emerge from horizontal fiber time delays and travel through locally asynchronous-irregular states

Zachary W. Davis[1,4✉], Gabriel B. Benigno[2,3,4], Charlee Fletterman[1,4], Theo Desbordes[1], Christopher Steward[3], Terrence J. Sejnowski[1,5], John H. Reynolds[1,5✉] & Lyle Muller[2,3,5✉]

Studies of sensory-evoked neuronal responses often focus on mean spike rates, with fluctuations treated as internally-generated noise. However, fluctuations of spontaneous activity, often organized as traveling waves, shape stimulus-evoked responses and perceptual sensitivity. The mechanisms underlying these waves are unknown. Further, it is unclear whether waves are consistent with the low rate and weakly correlated "asynchronous-irregular" dynamics observed in cortical recordings. Here, we describe a large-scale computational model with topographically-organized connectivity and conduction delays relevant to biological scales. We find that spontaneous traveling waves are a general property of these networks. The traveling waves that occur in the model are sparse, with only a small fraction of neurons participating in any individual wave. Consequently, they do not induce measurable spike correlations and remain consistent with locally asynchronous irregular states. Further, by modulating local network state, they can shape responses to incoming inputs as observed in vivo.

---

[1] The Salk Institute for Biological Studies, La Jolla, CA, USA. [2] Department of Applied Mathematics, Western University, London, ON, Canada. [3] Brain and Mind Institute, Western University, London, ON, Canada. [4] These authors contributed equally: Zachary W. Davis, Gabriel B. Benigno, Charlee Fletterman. [5] These authors jointly supervised this work: Terrence J. Sejnowski, John H. Reynolds, Lyle Muller. ✉email: zdavis@salk.edu; reynolds@salk.edu; lmuller2@uwo.ca

Visual cortical neurons exhibit variable fluctuations in their spontaneous activity and stimulus-evoked responses. Rather than being due to noise intrinsic to the neural spiking mechanism[1], which is highly reliable[2], variability is thought to emerge from ongoing synaptic activity in the dense recurrent connectivity of cortical networks[3,4]. When observed from a single point in the cortex, spontaneous fluctuations resemble a broadband temporal noise process[4,5]. Multisite recordings have revealed that these temporal fluctuations can be part of waves traveling across a cortical area[6–10]. Spontaneous traveling waves had largely been observed in slow-wave fluctuations associated with anesthesia, sleep, or low arousal[11–13]. While traveling waves had been theorized to have an impact on cortical computation, it was difficult to identify their role since active cortical states exhibit fluctuations that are more complex, dominated by higher-frequency and lower-amplitude activity[14], making these waves harder to detect. Further, driving input is believed to quench variability in ongoing dynamics[15], calling into question the potential impact of traveling waves on evoked activity[16].

Recent work has shown that spontaneous traveling waves are present in the awake state, that they influence the magnitude of sensory-evoked activity, and that—depending on their retinotopic alignment with sensory input—they can improve perceptual sensitivity[17]. However, the mechanisms that generate them, and whether they are consistent with the asynchronous-irregular spiking dynamics characteristic of awake cortex[18], are unknown. Based on their speed of propagation, we hypothesize that these waves result from action potentials propagating along unmyelinated horizontal fibers. To test this hypothesis, we studied a spiking network model across a range of biologically realistic neuronal densities, distance-dependent connection probabilities, excitatory/inhibitory balances, and synaptic conductance states. Importantly, this model incorporated axonal time delays from conduction along unmyelinated horizontal fibers, which shaped ongoing activity patterns into traveling waves consistent with those observed in vivo. Spontaneous traveling waves were apparent in this network model and occurred consistently across a wide parameter range that produced asynchronous-irregular dynamics.

One might wonder whether the occurrence of these traveling waves induces correlated variability, which has been found to impair perception[19]. Results from the spiking network model show this need not be the case. In both the computational model and multielectrode recordings in the marmoset visual system, we found the change in spiking probability due to the wave was low, only sparsely modulating spiking activity. We thus refer to the model as the sparse-wave model and this regime as the sparse-wave regime. This is in contrast to smaller-scale network models where spikes are strongly coupled to the state of traveling waves, producing strong correlations in spiking activity. Rather, at the scale of entire cortical areas, spontaneous waves can emerge in spatially structured shifts in spiking probability and propagate through sparse spiking activity along horizontal fibers, without inducing changes in pairwise correlations in the activity of individual neurons. Traveling waves can thus coexist with a locally asynchronous-irregular state, conferring their benefits while maintaining the computational advantages of this dynamical regime[20,21].

Results

Spontaneous synaptic fluctuations are comparable to those during stimulus-evoked responses. Previous work has shown that moment-by-moment fluctuations in synaptic input in the cortex can be on the same order of magnitude as during the sustained period of stimulus-evoked responses[6,22–24]. Fluctuating synaptic inputs can have a significant impact on neural excitability[25], gain modulation[26], and readout of sensory information[7]. To understand the impact of the spontaneous network state on evoked responses in the awake visual cortex, we recorded spontaneous and stimulus-evoked activity from chronically implanted multielectrode Utah arrays (Blackrock Microsystems) in area MT of two common marmosets (*Callithrix jacchus*; data previously reported by Davis et al.[17]). Spontaneous multiunit activity recorded from a single electrode while a marmoset fixated a fixation point was characterized by a low, irregular firing rate. The appearance of a highly salient stimulus (10% Michelson contrast drifting Gabor) within the multiunit receptive field evoked a robust response (Fig. 1a). When measured over many repeated presentations of the stimulus, the mean multiunit firing rate rose from 13 ± 1.6 sp/s during fixation, to 97 ± 5.7 sp/s in response to the stimulus ($N = 40$ trials over three recording sessions). These evoked spiking responses were variable from trial to trial (mean fano factor = 1.01 ± 0.01 SEM, 40–240 ms after stimulus onset), consistent with previous observations[15,27,28].

This variability is partly the result of ongoing spontaneous fluctuations in synaptic activity in the local population at the time of the evoked spiking response[6,7]. These fluctuating synaptic inputs, in turn, contribute to the local field potential (LFP)[29,30]. When averaged across high-contrast trials, the LFP had a robust negative deflection aligned to the stimulus-evoked spiking response, while the pre-stimulus period was flat (black line, Fig. 1a). However, at the single-trial level, the stimulus-evoked LFP response was similar in magnitude to the spontaneous fluctuations occurring during fixation (right panel, Fig. 1a). The relative power between the LFP just prior to the stimulus (−200 to 0 ms) and following stimulus onset (+50 to +250 ms) across single trials had a small but significant difference from 0 dB, which represents parity between spontaneous and stimulus-evoked fluctuations (median 1.89 dB, $p = 0.00005$ two-tailed Wilcoxon's rank-sum test).

While strong, high-contrast visual stimulation evoked slightly stronger LFP fluctuations than intrinsic network fluctuations, the distinction disappears in the context of weak visual inputs (Fig. 1b). When the marmoset was presented a faint stimulus that was detected ~50% of the time (<2% Michelson contrast), the evoked spiking response was significantly weaker and more variable (mean = 68 ± 4.4 sp/s, $p = 0.0009$; fano factor = 1.54 ± 0.14, $p = 0.002$, two-tailed Wilcoxon's rank-sum test). This corresponded with a weaker average LFP response, and the trial-by-trial relative power between spontaneous and evoked fluctuations was not significantly different from 0 dB (median = 1.23 dB, $p = 0.07$ two-tailed Wilcoxon's rank-sum test).

Given the comparable magnitude of spontaneous LFP fluctuations to responses evoked by weak sensory inputs, we hypothesized that much of the variability in neuronal spiking could be explained by the state of the local network since the synaptic drive (manifested in the LFP) during spontaneous and evoked activity is roughly equal[22,23]. We recently reported that spontaneous LFP fluctuations in the awake cortex are organized into waves that travel across an entire cortical area (Fig. 1c and Supplemental Movie S1). They modulate spontaneous spiking probability (Fig. 1d), and they directly impact the magnitude of stimulus-evoked responses depending on their alignment with neuronal receptive fields (Fig. 1e). We found that, rather than acting as a source of noise that impairs perception, spontaneous waves can—depending on their spatiotemporal alignment with a visual stimulus—improve the monkeys' ability to detect the stimulus. We thus sought to understand what mechanisms might generate traveling waves in the cortex and test whether they represent an operating regime either consistent with or distinct

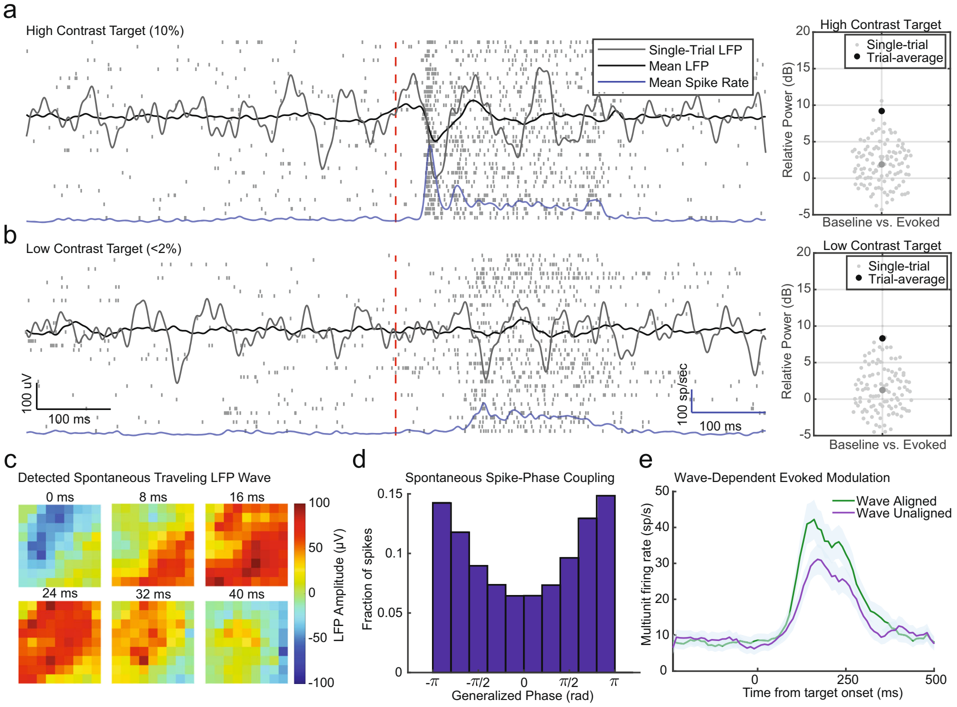

Fig. 1 Spontaneous network fluctuations are of similar magnitude to stimulus-evoked responses in vivo. a Spike raster for repeated presentations ($N = 40$) of a high-contrast (10% Michelson contrast) drifting Gabor recorded from area MT of a fixating marmoset (stimulus-onset, red line; mean response, blue line). A single-trial LFP trace is plotted in gray, and the average LFP response is plotted in black. The relative power between baseline (−200 ms to stimulus-onset) and evoked fluctuations (stimulus-onset + 50–250 ms) significantly favored the evoked response (right panel; $N = 110$ trials; median = 1.89 dB, $p = 0.000019$, two-tailed Wilcoxon's ranked-sum test). **b** Same as in (**a**), but for a low contrast stimulus (<2% Michelson contrast). The relative power between baseline and evoked LFP fluctuations was not statistically different from parity (median = 1.23 dB, $p = 0.087$ two-tailed Wilcoxon's ranked-sum test). **c** An example of spontaneous LFP fluctuations structured as a traveling wave recorded from a spatially distributed multielectrode array in marmoset area MT. **d** Histogram of spontaneous spike probability as a function of the generalized phase of the LFP during fixation. **e** The average evoked response to low contrast stimuli was stronger when a more excitable phase ($\pm\pi$ rad) of a spontaneous traveling wave aligned with the retinotopic location of the target (aligned, green line) as compared to when a less excitable phase (0 rad) was aligned (unaligned, purple line; $N = 43$ wave and non-wave trials; shaded region SEM; $p = 0.0000015$ two-tailed Wilcoxon's rank-sum test). Data for panels **c**–**e** modified from Davis et al.[17] with permission.

from the irregular, asynchronous activity patterns classically observed in silico[31,32] and in vivo[21,33].

Spontaneous traveling waves can emerge in network models without altering individual neuron spiking statistics. To address this question, we studied large-scale spiking network models composed of leaky integrate-and-fire (LIF) neurons with balanced excitation and inhibition and conductance-based synapses. When neuronal interactions are modeled as conductances, taking into account the time-dependent driving forces and channel activations at the synapse, spiking network models can enter into states of self-sustained activity[34,35]. Asynchronous-irregular activity[32] in these self-sustained states, generated without external drive, results naturally from the recurrently generated fluctuations intrinsic to the dynamics of the system[34,35]. These dynamics are characterized by low, variable firing rates, weak pairwise correlations, and coefficient of variation (CV) near unity. These self-sustained states provide an opportunity to study spiking network dynamics that are structured by the recurrent activity of the network itself, rather than dominated by random external Poisson synaptic input[20], and are well suited to model the spontaneous background activity observed in the cortex during active perception.

We first studied a two-dimensional (2D) conductance-based spiking network model with over 1,000,000 neurons distributed over a 6×6 mm^2 area consisting of 80% excitatory and 20% inhibitory neurons, randomly connected with 3000 synapses per cell, yielding a sparsely connected network (Fig. 2a). We eliminated the outer millimeter from analysis, yielding a 4×4 mm^2 area with 450,000 neurons. These values were selected to approximate the density and connectivity of neurons in cortical layer 2/3 of area MT in the common marmoset[36,37]. This randomly connected network generated self-sustained activity with spontaneous spiking fluctuations consistent with the asynchronous-irregular regime[32,38] and lacked any spatiotemporal structure (Fig. 2b, c). A simulated LFP was calculated from summed excitatory and inhibitory synaptic activity over adjacent, nonoverlapping pools of 10×10 neurons (corresponding to 67.8×67.8 µm^2)[39] and was used to estimate the local excitability state at each point in the network for comparison to the electrophysiological recordings. The LFP was homogeneous across the network, as would be expected from pools of neurons receiving synaptic input from random positions in the network (Fig. 2c and Supplemental Movie S2).

To test whether topographic connections with transmission delays were sufficient to generate spontaneous traveling waves in

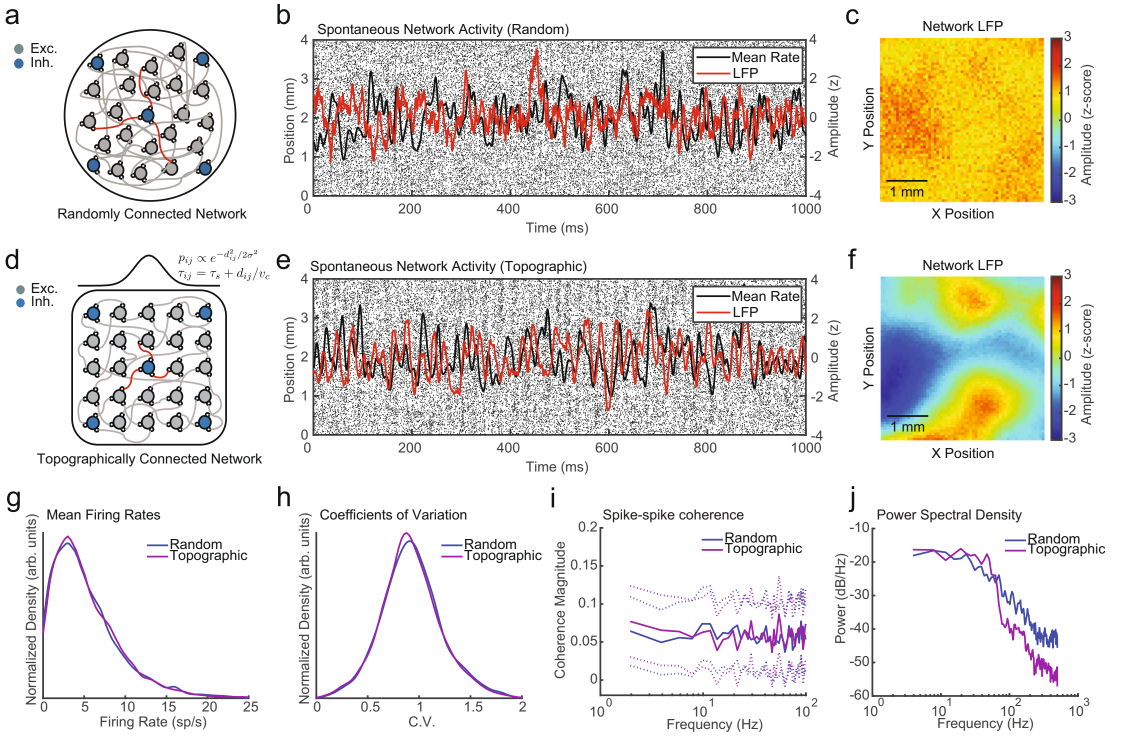

Fig. 2 Topographically connected networks produce structured fluctuations without altering neuronal spiking dynamics. a Schematic diagram of a 2D spiking network model with 80% excitatory (gray) and 20% inhibitory (blue) neurons wired with a uniformly random connection probability. **b** Spike rasters from 10,000 excitatory neurons along a 1D slice arranged by linear distance in the network. LFP fluctuations calculated from summed synaptic currents for a single 10 × 10 neuron pool is plotted in red. The mean spike rate within one neuron pool is shown in black. **c** Spatial organization of LFP amplitude for each neuron pool in the network plotted at one time point. **d** Network schematic as in (**a**), but the network was topographically connected with probabilities drawn from a Gaussian ($\sigma = 400\,\mu$m), and activity had a distance-dependent transmission delay (0.2 m/s). **e** Spike rasters as in (**b**), but sparse structured fluctuations were apparent across the network. **f** Spatial LFP amplitude as in (**c**), but the LFP was heterogeneous across the network with topographic structure. **g** The distribution of single-unit mean firing rates did not differ between the random (blue line) and topographic networks (purple line; $N = 5000$ neurons; $p = 0.28$, two-tailed Wilcoxon's rank-sum test). **h** The distribution of single-unit CV did not differ between the random and topographic networks ($p = 0.11$). **i** Pairwise spike coherence did not differ between the random (blue line) and topographic networks (purple line; $N = 10$ paired adjacent neuron pools; CI test, $\alpha = 0.05$; dotted lines 95% CI). **j** Power spectral density for LFP from the random and topographically connected networks.

the network, as a refinement to the model described in Fig. 2a, two key elements were introduced: (1) connection probability decayed as a Gaussian with the distance between neurons ($\sigma = 400\,\mu$m)[40,41] to mimic the topographic connectivity in cortex and (2) action potentials activated synaptic currents after a time delay determined by the distance between neurons to simulate the conduction velocity of horizontal fibers in the cortex ($v_c = 0.2$ m/s;[42] Fig. 2d). This network also produced self-sustained, spontaneous fluctuations, but spiking activity was weakly organized into bands that moved across the network as traveling waves (rasters, Fig. 2e). LFP fluctuations were heterogeneous across the network and exhibited organized spatial structure with localized regions coordinated in amplitude (Fig. 2f and Supplemental Movie S3).

To test whether the presence of these organized topographic fluctuations altered the asynchronous-irregular dynamics of individual neurons in the network, we compared the firing rates and CV across a randomly selected population of excitatory neurons ($N = 5000$). There was no difference in the distribution of firing rates across the networks (mean rate = 5.23 vs. 5.27 sp/s; $p = 0.28$, two-tailed Wilcoxon's rank-sum test; Fig. 2g) or in the distribution of CV (mean CV = 0.93 vs. 0.92; $p = 0.11$, two-tailed Wilcoxon rank-sum test; Fig. 2h). Therefore, individual neurons maintained their asynchronous and irregular firing states while the topographically connected network produced spontaneous traveling waves.

While one might expect the organized bands of spiking activity would result in increased correlations across neurons, we found no evidence that this was the case. The introduction of topographic connections did not affect pairwise correlations, as the degree of spike–spike coherence between the randomly and topographically connected networks was indistinguishable (Fig. 2i). No change in coherence occurred despite the topographically connected network producing increased power in lower frequencies (30–50 Hz) and reduced power in higher frequencies (>60 Hz) relative to the randomly connected network (Fig. 2j). The spatiotemporal structure could, therefore, exist in these networks without disrupting CV or pairwise coherence because the spiking probability was only weakly modulated by the presence of traveling waves. The probability of a neuron firing a spike at any given millisecond was low, and the peak of a traveling wave only marginally increased spiking probability (2.33%

increase), resulting in only a small fraction of neurons spiking during the peak of any given wave. We, therefore, refer to this as the "sparse-wave" network regime. If it were the case that neurons strongly participated in these fluctuations, then they would show a degree of coherence in the range of frequencies dominated by those fluctuations. To demonstrate this, we simulated a smaller network with fewer neurons and denser connections (model parameters Table S1), which generated spontaneous fluctuations that strongly regulated spiking activity. This "dense-wave" network did strongly modulate spiking activity during traveling waves (26.48% increase in spiking probability), which produced strong spike–spike coherence in the frequency band dominated by fluctuations in the LFP (Fig. S1). This increase in correlation was greatest for nearby locations in the network and was negatively correlated with distance (Pearson's $r = -0.72$; Fig. S2). Thus, unlike in the dense-wave network, traveling waves in the sparse-wave regime do not necessarily induce pairwise correlation across the network.

Topographic connectivity and distance-dependent delays are necessary to generate spontaneous waves. As hypothesized, the addition of topographic connections and conduction delays was sufficient to produce clear spatiotemporal organization in the network activity (Fig. 3a). In order to detect traveling waves, we utilized the property that activity patterns propagating at a fixed speed in the network will produce a band at a constant slope in the 2D space–time fast Fourier transform (FFT)[43]. Importantly, although the power spectral density at each point in the network had broad-spectral power (Fig. 2j), the 2D space–time FFT revealed a clear spectral peak (Fig. 3b), whose slope in relation to the temporal and spatial frequencies was dependent on the axonal conduction speed. To classify these activity patterns as traveling waves and quantify their properties relative to cortical recordings from the marmoset cortex, we applied the same analysis technique developed for the experimental recordings (generalized phase, GP[17]) to the simulated LFP in each 10×10 neuronal pool. We then adapted a technique previously developed for detecting

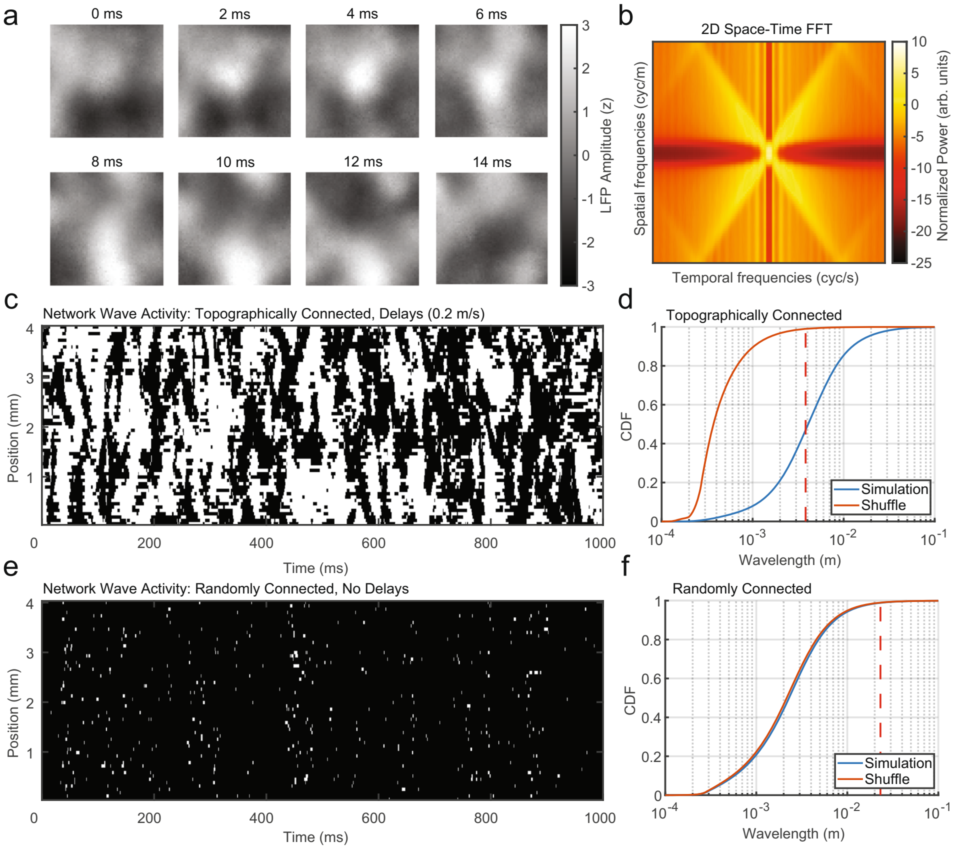

Fig. 3 Spontaneous topographic network fluctuations travel as waves. a Time series of simulated LFP activity from the topographically connected network in Fig. 2. Regional peaks and troughs moved coherently across the network as traveling waves. **b** 2D (space–time) FFT reveals a concentration of spatiotemporal energy along temporal (*x*-axis) and spatial (*y*-axis) frequencies reflecting the flow of activity across the network. **c** The presence of significant wave activity for a linear slice through the large-scale 2D network model. Significant (white) wave values were defined as estimated wavelengths that exceeded the 99th percentile of the spatially shuffled wavelength distribution (48.53% of network activity). **d** Cumulative distribution functions (CDFs) of the observed wavelengths (blue) and wavelengths after spatially shuffling the LFP pool locations (red, 99th percentile, red dashed line). **e** The randomly connected network had few points that were classified as traveling waves (1.12% of network activity). **f** Wavelength CDFs as in (**d**) for the randomly connected network and its shuffle.

traveling waves in noisy multielectrode recordings[44,45]. We estimated the gradient of the phase at each moment in time and calculated putative wavelengths. We then identified places and times in the network where there was significant spatial organization. Significance was determined by comparing the observed wavelengths to the wavelength distribution after a spatial shuffle of electrode positions, with the 99th percentile of the shuffle distribution taken as the threshold criterion (Fig. 3c, d). This approach provides a sensitive and robust means to detect traveling waves from moment to moment[44,45]. We found significant wave activity in the topographically connected network ~50% of the time, whereas the presence of significantly structured wave organization was absent from networks with random connections and no delays (Fig. 3e) as the distribution of putative wavelengths was similar to the shuffled distribution (Fig. 3f).

We also explored the sufficiency of topographic connections and conduction delays in generating waves separately (Fig. S3). A topographic network lacking transmission delays produced spatially organized activity, but there was no spectral line in the 2D FFT consistent with traveling waves (Fig. S3b). Conversely, delays in an otherwise randomly connected network did not generate large-scale spatially organized activity, but did have a clear spectral line consistent with propagating activity (Fig. S3c). From this, we conclude that, in our framework, topographic connectivity is necessary for the emergence of large-scale spatially organized activity, and transmission delays are necessary for the regular flow of activity over space and time. Both topography and delays together are necessary in our network framework to produce spatiotemporal dynamics that travel over the network consistent with the traveling waves we observed in our cortical recordings. These results were consistent in a simpler one-dimensional (1D) network model where the emergence of traveling waves required both topographic connections and transmission delays (Fig. S4).

Spontaneous waves occur throughout the asynchronous-irregular regime. In the example network, topographic connections with axonal conduction delays were sufficient to induce large-scale waves of activity without disrupting the fine-scale asynchronous-irregular dynamics of individual neurons. Does the presence of traveling waves generalize across all networks with asynchronous-irregular activity, topographic connections, and axonal conduction delays[35,38]? We scanned across 2500 combinations of different excitatory and inhibitory (E/I) conductances in the topographically connected model and found 601 combinations that produced self-sustained spiking activity. We then identified networks with asynchronous-irregular spiking dynamics, defined as networks with mean excitatory firing rates between 1 and 25 sp/s and mean CV between 0.7 and 1.4[38]. Approximately 99% (599 out of 601) of the networks that generated self-sustained activity were classified as asynchronous irregular. We then measured the percentage of time each network's activity was significantly organized into traveling waves. Waves were present across the entire range of asynchronous-irregular networks (Fig. 4a). The strength of wave activity was negatively correlated with the magnitude of E/I conductance (Pearson's $r = -0.55 \pm 0.002$, 95% confidence interval (CI)) indicating weaker synapses led to stronger wave activity. The average wavelength was positively correlated with synaptic strength (Pearson's $r = 0.72 \pm 0.001$; Fig. 4b), indicating stronger synaptic weights lead to more synchronous network dynamics. These results demonstrate that spontaneous traveling waves are a general property of topographic connectivity and are entirely consistent with locally asynchronous-irregular states.

How important is network scale in generating traveling waves? To answer this question, we simulated networks ranging from 0.5 to 4 mm in width, holding neuronal and connection density constant. For small networks (~0.5 mm), a very limited range of the E/I space produced self-sustained and asynchronous network dynamics. As network size grew, the asynchronous-irregular parameter space grew as well, extending to include smaller and smaller combinations of E/I synaptic strength[18] (Fig. 4c). It was thus necessary to simulate spiking network models at sufficient spatial scales (>1 mm) to generate asynchronous-irregular activity in networks with conductances resembling those estimated in vivo[18]. At small network scales, wavelength distributions during asynchronous-irregular dynamics were not distinct from the spatial shuffle, and the parameters that favored longer wavelengths did not produce asynchronous-irregular activity. Only at larger network scales did wave activity become strongly apparent (Fig. 4d).

Network connectivity determines wave properties. What effect did our chosen parameters for connection distance and conduction velocity have on wave properties? We hypothesized the spatial extent of connections and the conduction speed of spikes directly control the wavelength and propagation speed, respectively, of traveling waves in the model. To test these predictions, we simulated networks with various values of standard deviation (σ_s) for the Gaussian connection probability distribution. Consistent with our hypotheses, the distribution of significant wavelengths increased with larger connection distances (Fig. 5a and Supplemental Movies S4 and S5), and increasing the conduction velocity created a corresponding increase in the propagation speed reflected in the slope of the spectral line in the space–time FFT (Fig. 5b). Thus, the macroscopic features of spontaneous traveling waves were directly related to specific network structures in the model.

Are these waves only possible with perfectly Gaussian connection profiles and uniform conduction velocity, or can they tolerate a broad range of values similar to those observed in vivo? To test this, we simulated the example model in Fig. 2, with 10% of the connections randomly rewired with uniform probability across the network, generating long-range connections[46,47]. The conduction velocity along each connection was drawn from the range of conduction speeds observed for unmyelinated horizontal fibers in the cortex (0.1–0.6 m/s[42,48,49]). Spontaneous traveling waves persisted under these network conditions (Fig. 5c, d), indicating that the presence of waves was not limited to a fixed or limited set of homogeneous network properties, but instead also occurred in networks with large heterogeneity, as in the cortex.

Network simulations are consistent with traveling waves in vivo. How well do the dynamics observed in our simulations match the dynamics observed in electrophysiological recordings of the cortex? To test this, we compared the model results to the data recorded from marmoset MT, while monkeys fixated a spot at the center of an otherwise gray computer screen. We measured the mean firing rates (Fig. 6a) and CV (Fig. 6b) across the population of single- and multiunit activity over multiple recording sessions. The distributions of firing rates and CV were qualitatively similar between the recorded data and the sparse-wave model, suggesting that the spontaneous dynamics in the cortical recordings are also consistent with the asynchronous-irregular regime.

We next measured the distribution of estimated wavelengths in the data and compared this to the wavelength distribution in the model. LFP data in the cortex are not independent across electrodes (as it is in our simulation), but rather pools signals from a cortical volume of ~250 μm in a radius around the electrode tip[29,30] and has correlations that fall off with distance[14].

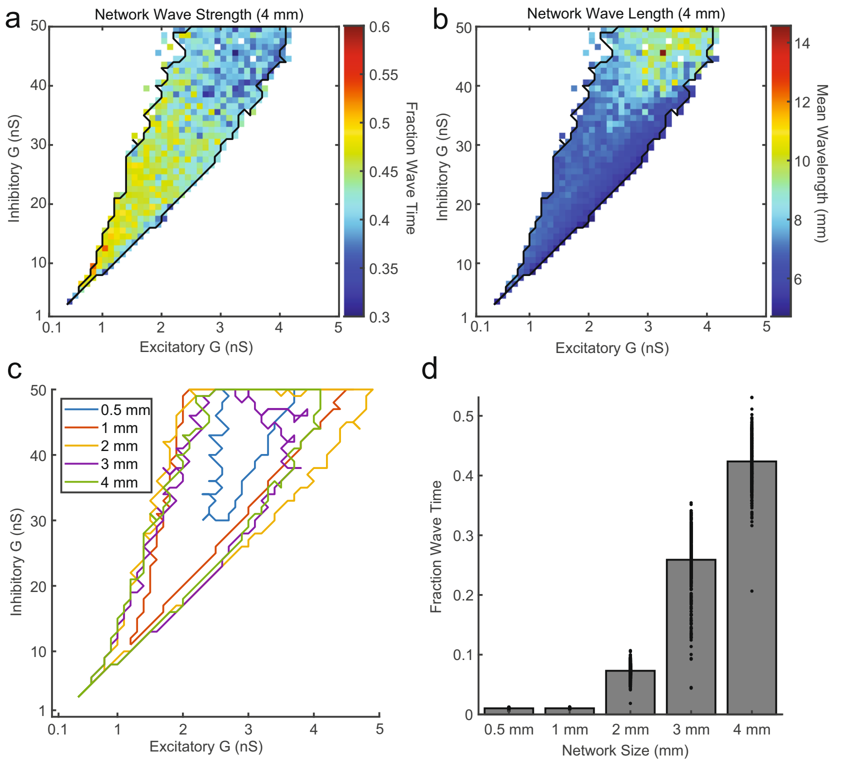

Fig. 4 Spontaneous traveling waves emerge in network regimes consistent with asynchronous-irregular dynamics. a The percentage of wave-like activity across ranges of excitatory and inhibitory conductances for 4 mm width topographic network simulations. Each pixel is one simulation of a network as described in Fig. 2d, but with the excitatory and inhibitory conductances corresponding to its *x* and *y* coordinate, respectively. Networks consistent with asynchronous-irregular spiking dynamics fall within the black border. White pixels are networks that did not self-sustain or had extremely low/high mean firing rates (FR < 1 or FR > 25 sp/s). **b** Same as (**a**), but the mean of the wavelength distribution is plotted. **c** The region of the parameter space that exhibited asynchronous-irregular activity grew to include smaller synaptic conductances with the size of the network (width 0.5 mm to 4 mm). **d** The fraction of wave activity present across all self-sustained and asynchronous-irregular networks grew with the size of the simulated network ($N = 163$, 532, 752, 540, and 599 stable A–I simulations for sizes 0.5, 1, 2, 3, and 4 mm respectively).

To emulate these properties of cortical LFP recordings, we applied a smoothing kernel that expanded the area of integration from each simulated LFP point and reduced the independence of the signal. After smoothing our simulated LFP and quantifying wave properties, the distribution of simulated wavelengths closely approximated the distribution observed in the cortex (dotted gray and blue lines, Fig. 6c). Similarly, the distribution of observed speeds in both the network simulation and the data covered the range of conduction velocities in the horizontal fibers, peaking at ~0.2 m/s (Fig. 6d). Thus, across four different measures (spike rate, spike variability, wave size, wave velocity), the distributions characterizing activity in the network model were in close alignment with experimental recordings.

Neurons sparsely participate in waves due to weak coupling to synaptic fluctuations. How does activity in the sparse- and dense-wave networks affect the membrane potentials at the level of individual neurons? To answer this question, we studied the membrane potential distributions of individual neurons in each network. In the sparse-wave model, membrane potential fluctuations were Gaussian and close to the spiking threshold, consistent with the fluctuation-driven regime[50] (black line, Fig. 7a). This was in contrast to the skewed distribution of membrane potentials in the dense-wave network, which was consistent with a synaptic drive to neurons that is clustered and strongly correlated[51] (purple line, Fig. 7a).

In the sparse-wave network model, stochastic fluctuations in the membrane potential produced sparse and irregular spiking activity. These fluctuations were driven by shifts in excitatory-inhibitory balance across the local population, which, due to the topographic network connections, were shared by adjacent populations and carried by spikes across horizontal connections. These summed currents in our estimate of the LFP reflect the total synaptic input in the local population, which exhibited a counter phase relationship with the relative E/I balance: the inhibition-dominated E/I regime produced positive LFP potentials, and the excitation-dominated E/I regime produced negative LFP potentials (Fig. 7b, c). This leads to the mechanistic observation that when the conductances are high, the z-scored LFP is positive and the balance is dominated by the shunting effects of inhibition. When the conductances are low, the z-scored LFP is negative and the balance is shifted to excitation, producing more spiking activity. This relationship mechanistically accounts for the phase-dependent relationship of spiking to the LFP in our cortical recordings.

To demonstrate that simulated neurons are sparsely modulated by traveling waves, we measured the LFP phase at which each spike occurred (10 bins from $-\pi$ to π; Fig. 7d) across network

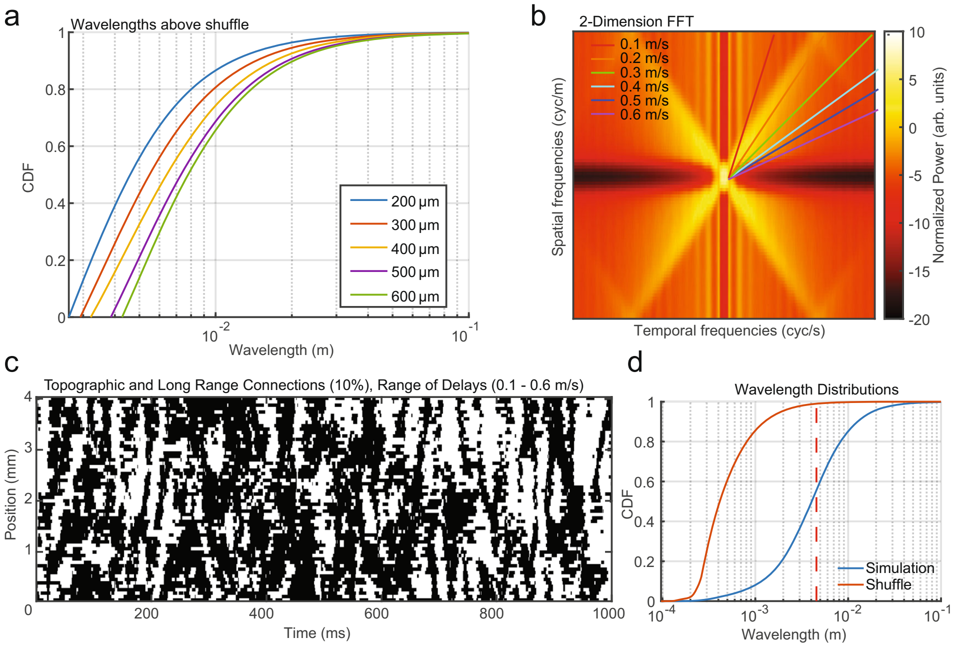

Fig. 5 Wavelength and speed distributions change with connection distance and conduction velocity parameters. a Distribution of wavelengths exceeding the 99th percentile of a spatial shuffle for networks simulated across a range of Gaussian sigma values for the topographic connection probability. **b** 2D FFT for the topographic network with delays produced by 0.2 m/s conduction velocities. The colored lines match the slopes of the concentration of spatiotemporal energy across different simulations with conduction velocities ranging from 0.1 to 0.6 m/s. **c** Significant wavelengths (white pixels) were strongly present in a network with a mix of topographically (90%) and randomly (10%) connected projections and a range of conduction velocities (0.1–0.6 m/s). **d** CDFs for the simulation in (**c**) and its shuffle (blue and red, respectively).

simulations with varying E/I synaptic conductances. The degree of spike-phase modulation was significant across the entire parameter space, with spikes more likely during phases closer to $\pm\pi$. The magnitude of this modulation was correlated with the magnitude of E/I conductances (Pearson's $r = 0.78 \pm 0.001$, 95% CI; $N = 599$ simulations), with stronger synaptic weights driving stronger coupling of spiking activity to LFP fluctuations indicating denser and more synchronous spiking waves. This result highlights the importance of large-scale network simulations that can produce stable A–I spiking dynamics with weaker synaptic weights to see sparse modulations of spiking probability by traveling waves. We chose a point among these small conductance values (1 nS G_e, 10 nS G_i; same values for the topographic network in Fig. 2), to compare the degree of coupling between the model and the cortical recordings. There was no difference between the magnitude of spike-phase modulation observed in the sparse-wave network model and the recorded data ($N = 22$ matched resamplings; model spike-phase index = 0.15 ± 0.001 SEM; cortex spike-phase index = 0.16 ± 0.005; $p = 0.18$, two-tailed Wilcoxon's rank-sum test), although the preferred phase-angle differed slightly between the data and model (data-preferred phase = 3.05 rad, model-preferred phase = −2.27 rad).

While there was a similar degree of spike-phase modulation between the cortical data and the sparse-wave model (Fig. 7e, f), the modulation was significantly stronger in the dense-wave model ($N = 10$ resamples; spike-phase index = 0.44 ± 0.01, $p = 0.000085$, two-tailed Wilcoxon's rank-sum test; Fig. 7g). The phase distribution also differed strongly in peak phase angle (dense-preferred phase = −1.11 rad). In addition, the randomly connected network showed no spike-phase relationship ($N = 22$ resamples; spike-phase index = 0.03 ± 0.001 SEM, Fig. S5), as expected from a network where the neurons in the LFP pool draw from inputs distributed throughout the entire network. These results demonstrate that—in the simulated large-scale spiking networks—spatiotemporal organization emerges from weak modulations of spiking probability that produces sparse, phase-modulated spiking activity traveling along topographically distributed horizontal fibers. The presence of a similar spike-phase relationship in vivo, particularly for model conductance states that corresponded to experimental estimates of neuronal conductance states[18], demonstrates that the sparse-wave regime in the model is consistent with the properties of waves observed in the experimental recordings.

Spontaneous traveling waves modulate responses to inputs. Finally, we hypothesized the state of network fluctuations in the sparse-wave network model would modulate the magnitude of responses evoked by feed-forward inputs, as previously studied for synaptic noise[4,26] and contextual gain control by visual stimuli[52–55]. To test this, we stimulated one 10 × 10 neuron pool in the sparse-wave network with a 20 Hz Poisson spike train on 100 afferent synapses to mimic feed-forward stimulus input to the network. We stimulated for 10 ms, aligned either to the depolarized or hyperpolarized state of network fluctuations defined, respectively, by the most and least probable phases for spikes to occur according to the network's spontaneous spike-phase distribution. When spiking inputs were aligned to the depolarized state, the evoked spiking responses were boosted (blue lines, Fig. 8a) relative to weaker responses when inputs were aligned to the hyperpolarized state (red lines, Fig. 8a). These effects were consistent with wave-modulated visual responses to motion stimuli observed in area MT in vivo (cf. Fig. 1e). In

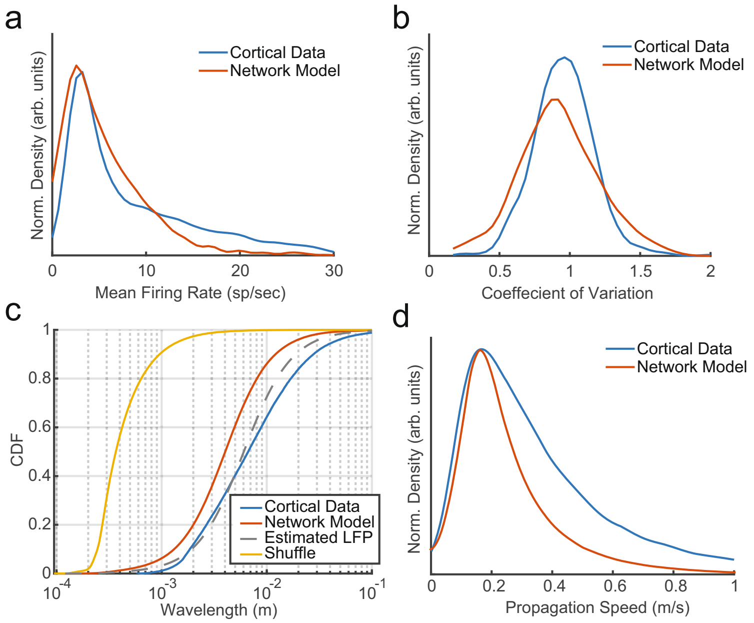

Fig. 6 Simulated network dynamics approximate dynamics observed in cortical recordings of area MT. a Distribution of unit mean firing rates across the topographic network simulation in Fig. 2d (red) and the distribution observed across single- and multiunits recorded from area MT of awake, behaving marmosets (blue). **b** The distributions of CV for simulated (red) and recorded cortical data (blue). **c** CDFs of wavelengths for the simulation in Fig. 5c (red), its shuffle (yellow), and the observed distribution recorded in the cortex (blue). Simulated wavelengths were more similar to observed wavelengths in vivo after applying a smoothing kernel across space in the simulated network to approximate the estimated spatial integration of the LFP in electrophysiological recordings (250 μm, gray dashed line). **d** Wave speed distributions for the simulation in Fig. 5c (red), and recorded cortical data (blue) covered a range consistent with axonal conduction velocities (0.1–0.6 m/s).

contrast, equal stimulation in either state of the dense-wave network produced little effect (red and blue lines, Fig. 8b).

To quantify the effect of the traveling waves on evoked responses in each network, we then calculated the gain modulation, which is the ratio of firing rates during the stimulus-evoked response divided by that of the no-stimulus case (Fig. 8c). Across repeated input stimulations, input gain was significantly stronger for the depolarized state relative to the hyperpolarized state in the sparse-wave network ($N = 40$ stimulations; depolarized state = 3.09 ± 0.09; hyperpolarized state = 2.11 ± 0.05, mean ± standard deviation; $p = 3.57 \times 10^{-8}$, two-tailed Wilcoxon's signed-rank test). In contrast, in the dense-wave network, the strong spontaneous fluctuations shunted the incoming spikes, resulting in very weak evoked responses that did not significantly differ depending on network state (depolarized state = 1.11 ± 0.05; hyperpolarized state = 1.10 ± 0.04; $p = 0.20$; two-tailed Wilcoxon's signed-rank test). The increase in gain that occurs in the sparse-wave network mirrors our observations of wave-dependent sensitivity in awake monkeys performing a threshold detection task[17]. Thus, the sparse-wave model offers a mechanistic account for observed phase-dependent modulations of weak sensory responses by traveling waves measured in vivo that a network characterized by dense-wave dynamics fails to replicate.

Discussion

The present work builds on and seeks to explain our recent finding that spontaneous fluctuations in cortical activity modulate the moment-to-moment processing of sensory information in a manner that affects perceptual sensitivity. These fluctuations are neither synchronous across the cortical surface nor independent noise processes. Rather, they are often structured as traveling waves. The model presented here shows that distance-dependent conduction delays in topographic, conductance-based spiking network models are sufficient to account for our results in vivo. Waves occur spontaneously, without requiring a driving input, and they occur robustly, in the sense that they are generated across a wide parameter space and in the sense that they occur across the entire space of E/I conductances that gives rise to asynchronous-irregular activity dynamics. The properties of these waves depend systematically on the scales of distance-dependent connections and the speeds of action-potential propagation. The waves were well-matched to those observed in cortical recordings from behaving marmosets[17] for speeds consistent with the conduction velocity of unmyelinated horizontal fibers. Neurons sparsely participated in these waves at the scales of neuronal density and connectivity found in the cortex. The spiking sparseness of the waves allowed them to occur without disturbing the asynchronous-irregular dynamics that are observed in cortical activity and have advantages for neural computation[3,20,21,56,57]. These sparse-wave networks remain sensitive to spiking inputs, producing evoked responses modulated in a phase-dependent manner, as observed in vivo. This is in contrast to smaller-scale networks that exhibit dense waves that drive correlated fluctuations across the population and render the network insensitive to spiking inputs.

These results demonstrate the importance of considering distance-dependent time delays in neural systems. When considered at the scales of entire cortical areas, individual horizontal fibers can span distances ranging from hundreds of microns to several millimeters[46,47], with axonal conduction delays on the order of tens of milliseconds[42,48]. While previous spiking network models that considered relatively smaller spatial scales (from

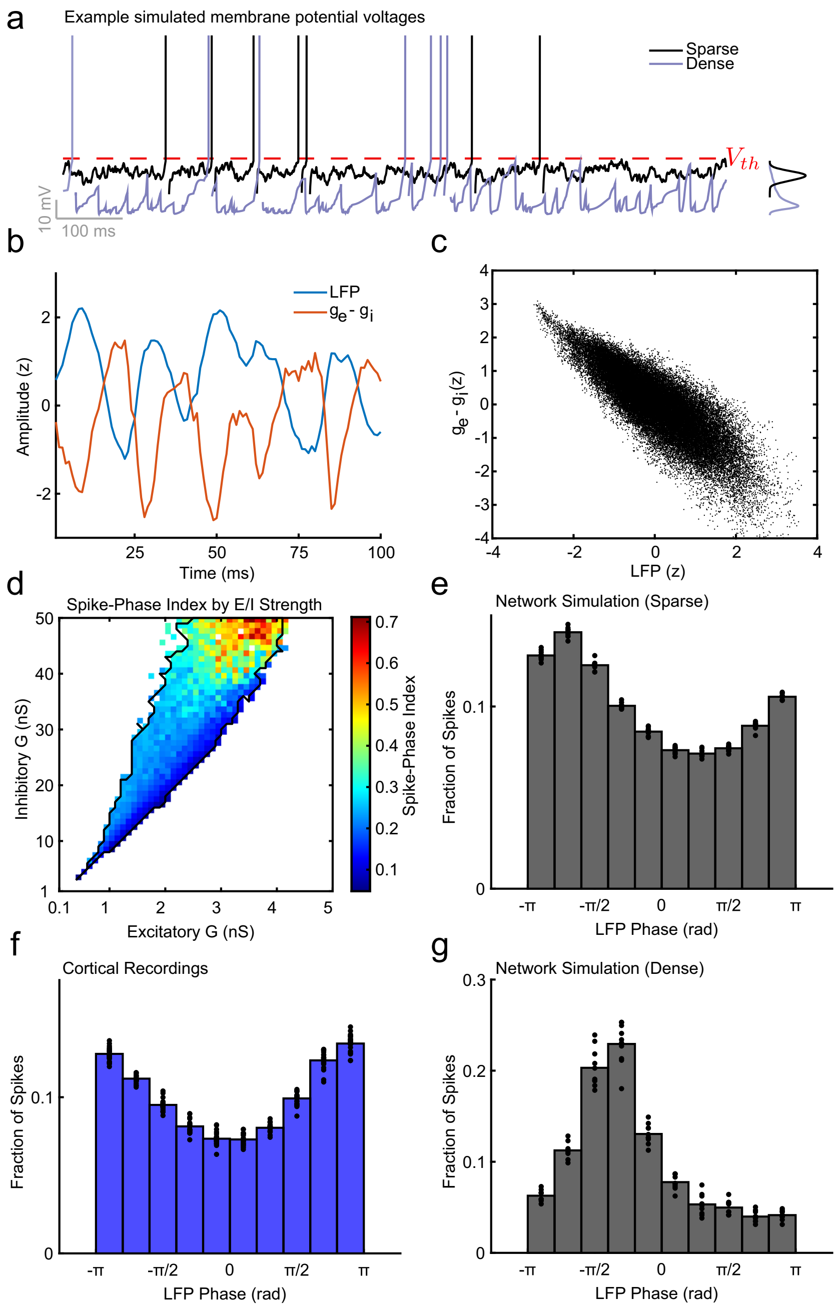

100 μm to 1 mm of cortex) held that the contribution of axonal delays was negligible in their effects on the temporal properties of spiking networks[58], other studies have found fixed delays can have profound effects[59–67]. The effects of fixed and distance-dependent delays have been extensively studied in neural field equations[68–77]; however, in these averaged population models the connection between single-unit and population activity is difficult to study because single-unit information is lost. Finally, traveling waves have been described in smaller-scale topographic spiking network models that lack distance-dependent delays, but these networks only produced dense waves of strongly correlated spiking activity[78–80]. In this work, our large-scale spiking model provides the insight that distance-dependent delays on scales relevant to a large extent of a visual region in the cortex provide a fundamental mechanism to shape spontaneous activity into waves throughout the state of balanced excitation and inhibition. Further, instead of being inconsistent with asynchronous-irregular states, as with previous models of traveling waves in spiking networks, spontaneous waves can travel across these large-scale spiking networks while local networks remain locally

Fig. 7 Spontaneous waves reflect structured fluctuations in E/I balance that sparsely modulate spike probability. a Membrane voltage for a simulated neuron in either the sparse-wave network (black line) or dense-wave network (purple line) calculated from the summed excitatory and inhibitory synaptic currents received by that neuron. Spiking activity occurred when the voltage crosses the threshold (V_{th} red line). The distribution of membrane potentials over the interval for the sparse and dense networks is plotted on the right. **b** The amplitude of the simulated LFP (blue line) and the relative level of excitatory and inhibitory conductance (red line) over a 10 × 10 neuron pool were counter phase. **c** Scatter plot of LFP and $g_e - g_i$ difference revealed a significant negative correlation ($N = 50{,}000$ time points; Pearson's $r = -0.83$; CI test, $\alpha = 0.01$). **d** Spike-phase coupling was significant across networks in the asynchronous-irregular regime, and the degree of coupling was correlated with the magnitude of synaptic conductance ($N = 599$ simulations; Pearson's $r = 0.78 \pm 0.001$, 95% CI). **e** Histogram showing the fraction of spikes that occurred during each phase of the simulated LFP in the topographically connected network. Spike probability was modulated by the LFP phase ($N = 22$ resamples vs. shuffle; spike-phase index = 0.15). **f** Same as in (**e**), but for recorded cortical data. Spike probability was similarly modulated (spike-phase index = 0.16; $N = 22$ recording sessions vs. shuffle). **g** The dense-wave network simulation had a significantly stronger spike-phase relationship ($N = 10$ resamples; spike-phase index = 0.44, $p = 0.0000085$, two-tailed Wilcoxon's rank-sum test).

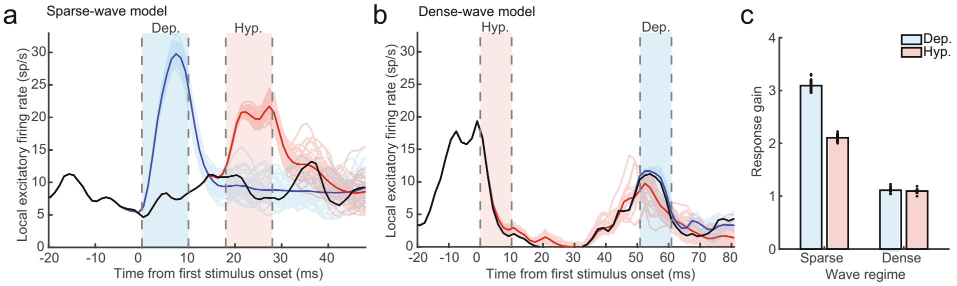

Fig. 8 The sparse-wave network regime boosts spike inputs while the dense-wave network shunts. a A 0.2 × 0.2 mm^2 pool in the sparse-wave network model received a 20 Hz Poisson spike train input for 10 ms aligned either to a period of depolarization (blue shaded region) or hyperpolarization (red shaded region) as defined by the spike-LFP phase relationship. The dark blue and red lines are the mean evoked firing rate after receiving the spiking input in either the depolarized or hyperpolarized phase respectively (light blue and red lines represent $N = 40$ individual trials). The black line is the firing rate of the neuron pool when no input was given. **b** Same as (**a**), but the inputs were delivered to the dense-wave network. The evoked responses were much weaker as the network shunted the currents evoked by the incoming spikes. **c** The response gain between the distributions of spontaneous and evoked activity across $N = 40$ presentations of spiking input. In the sparse-wave network (left bars), inputs during the depolarized state had larger relative responses as compared to inputs during the hyperpolarized state (3.09 ± 0.09 compared to 2.11 ± 0.05 mean ± standard deviation; $p = 3.57 \times 10^{-8}$, two-tailed Wilcoxon's signed-rank test). In contrast, the dense-wave network (right bars) responses did not differ in their response gain during the hyperpolarized and depolarized states (1.10 ± 0.04 and 1.11 ± 0.05, respectively; $p = 0.20$).

asynchronous. Thus, not only are spontaneous traveling waves consistent with the asynchronous-irregular regime, they are a necessary consequence of topographic connectivity and distance-dependent delays in cortex across conditions that yield asynchronous-irregular spiking.

Critically, the waves we observe sparsely modulate the background spiking probability of neurons in the network, allowing them to maintain locally asynchronous-irregular dynamics. These sparse-wave dynamics only become apparent when networks are modeled at sufficient scales, in particular hundreds of thousands of neurons over an area a few millimeters across. Our custom software implementation allowed for the simulation of networks with ~100,000 to 1,000,000 neurons, each with 3000 outgoing synapses per cell, addressing in the largest networks over 60 GB of RAM. Importantly, while the cells in our network models have a large number of synapses per cell, the number of possible connection partners is high such that the network connectivity remains sparse. In these networks, the large number of synapses per cell allows the network to achieve self-sustained asynchronous-irregular activity when synaptic conductances are on the order observed in cortex[35,81]. Importantly, the sparse waves we observe here may be related to the concept of sparse synchrony[82–84], which has been shown to facilitate information transfer across areas during narrowband oscillations. Sparse waves may reflect this principle unfolding over both space and time, while also being consistent with the more generally occurring broad-spectral fluctuations during spontaneous awake activity in vivo.

Our findings that traveling waves need not induce pairwise correlations may at first appear to differ from recent work by Huang et al. (2019), in which traveling waves emerged from different spatial and temporal scales of excitation and inhibition and drove shared variability in ongoing dynamics. We do not view these findings as mutually exclusive. The work of Huang et al. offers a mechanistic explanation for a source of shared variability that occurs particularly in low-frequency fluctuations in the sensory cortex[85]. This shared variability has been shown in theoretical[86–88] and experimental studies[19] to have deleterious effects on sensory processing and has been observed experimentally to be reduced by attention[85,89]. In contrast, our model does not generate strong low-frequency dynamics, but instead seeks to describe traveling waves that occupy higher-frequency ranges (above 10 Hz) that our model suggests propagate through horizontal connectivity. Separate mechanisms could underlie the generation of low-frequency correlated variability and higher-frequency traveling waves, the latter of which have recently been shown to have phase-dependent benefits for visual detection[17]. One critical difference between the two models, however, is their relative scale, leaving open the question as to whether the differences in spiking correlation are due to fundamental mechanisms or network size. Additional research is necessary to understand how such mechanisms may interact in large-scale network models to better recapitulate the broader space of cortical dynamics observed in vivo.

Unlike the outsized conductances typically used in smaller network simulations, the large-scale networks simulated here enabled us to incorporate E/I synaptic strengths that were similar to those observed experimentally, leading to total E/I conductances on the order of the leak conductance[18,90]. This is advantageous because the larger conductances needed in smaller networks yield unrealistic coupling of spiking activity to synaptic fluctuations and shunt driving inputs[91], as illustrated in the dense-wave model. By scaling our model to realistic neuronal densities on a spatial scale over several millimeters of the cortex (450,000 neurons over 16 mm^2 in the case studied here), the sparse-wave model sustains irregular activity, with strengths of individual synaptic inputs down to 0.5 and 4 nS for excitatory connections and inhibitory connections respectively. At these spatial scales and synaptic conductances, waves are present about 50% of the time, similar to what we find in the neocortex, and the wavelengths closely approximate those we find in vivo.

It is important to recognize that, while our network model of a cortical sheet generates self-sustained activity intrinsically, cortical circuits in vivo are driven by inputs from other cortical areas and subcortical structures, particularly the thalamus. Thalamic inactivation has been shown to severely attenuate the spontaneous firing rates of cortical neurons[92,93], raising the question as to whether spontaneous traveling waves in vivo also involve interactions between cortical and subcortical areas. In this work, our objective was to study whether or not topographic connectivity with conduction delays was sufficient to generate spontaneous waves, as well as to ask whether waves were compatible with asynchronous-irregular dynamics. We, therefore, chose to use the simplest model we could to test what parameters might recapitulate the properties of waves we had observed in the cortex. Undoubtedly, the massive connectivity across cortical areas and subcortical structures impact the features of spontaneous activity in the cortex, and understanding their contribution to the properties of intrinsic traveling waves will be an important avenue of future study.

Traveling waves of neural activity in the awake cortex have been observed under stimulus-evoked[44,94,95], behavior-evoked[96–98], and spontaneous conditions[17]. The fundamental neural circuit mechanism for these waves, however, had remained unclear. Our modeling results suggest that the spontaneous LFP fluctuations we observe traveling as waves in the cortex during active vision result from sparse waves of spiking activity traveling unmyelinated horizontal fibers. The sparse-wave model, which produces activity patterns consistent with the spiking activity observed in vivo, posits that these waves arise from the time delays inherent in communicating spikes across topographic connections within a cortical area. Further, observations from the model suggest that as these sparse waves traverse the massive recurrent connectivity within cortical areas[3,36,99,100], they produce subthreshold shifts in the local E-I balance that, collectively, modulate cortical excitability. Thus, the model offers an explanation for our empirical finding that perceptual sensitivity varies over space and time depending on the alignment of wave phase[17]. Importantly, these traveling waves need not introduce correlated variability believed to harm perceptual sensitivity; instead, the sparse-wave state weakly modulates the background spiking probability in locally asynchronous-irregular neuron pools. Rather than a source of noise, as would be predicted if waves modulated activity akin to the dense-wave regime, the presence of these sparse waves can boost weak inputs that would otherwise have been imperceptible. These results indicate these traveling waves may be a network mechanism that can improve perceptual processing when aligned to the source of feed-forward signals, without disrupting the computational benefits of the irregular spiking dynamics of individual neurons.

Methods

In vivo cortical recordings. The methods for the recordings and behavioral task used in this work was identical to work previously published[17], which provided the physiology and behavioral data used in this work. Two marmoset monkeys (*C. jacchus*), one male (monkey W) and one female (monkey T), were surgically implanted with a headpost for head stabilization during eye-tracking. The headpost housed an Omnetics connector for a 64-channel multielectrode recording array (Utah array, Blackrock Microsystems), which was implanted in a 7 × 10 mm^2 craniotomy over area MT (stereotaxic coordinates 2 mm anterior, 12 mm dorsal). Monkey W was implanted with an 8 × 8 recording array with channel spacing of 400 μm and monkey T was implanted with a 9 × 9 array with alternating channels removed yielding a channel spacing of 800 μm. Both arrays had a pitch depth of 1.5 mm. The arrays were chronically implanted over area MT using a pneumatic inserter wand. The craniotomy was closed with Duraseal (Integra Life Sciences, monkey W) or Duragen (Integra Life Sciences, monkey T), and covered with a titanium mesh embedded in dental acrylic. All surgical procedures were performed with the monkeys under general anesthesia in an aseptic environment in compliance with NIH guidelines. All experimental methods were approved by the Institutional Animal Care and Use Committee (IACUC) of the Salk Institute for Biological Studies and conformed to NIH guidelines.

Marmosets entered a custom-built marmoset chair that was placed inside a Faraday box with a liquid crystal display (LCD) monitor (ASUS VG248QE) at a distance of 40 cm. The monitor refresh rate was 100 Hz and gamma corrected with a mean gray luminance of 75 cd/m^2. Electrode voltages were recorded at 30 kHz from the Utah arrays using two Intan RHD2132 amplifiers connected to an Intan RHD2000 USB interface board. The marmosets were headfixed by a headpost for all recordings. Eye position was measured with an IScan CCD infrared camera sampling eye position at 500 Hz. Stimulus presentation and behavioral control were managed through MonkeyLogic (revision date: 4-05-2014, build 1.0.26) in MATLAB (version R2016b). Digital and analog signals were coordinated through National Instrument DAQ cards (NI PCI6621) and BNC breakout boxes (NI BNC2090A). Neural data were broken into two streams for offline processing of spikes (single- and multiunit activity) and LFPs. Spike data were high-pass filtered at 500 Hz and candidate spike waveforms were defined as exceeding 4 SDs of a sliding 1 s window of ongoing voltage fluctuations. Artifacts were rejected if appearing synchronously (within 0.5 ms) on over a quarter of all recorded channels. Segments of data (1.5 ms) around the time of candidate spikes were selected for spike sorting using principal component analysis through the open-source spike sorting software MClust (ver. 4.3.02; A. David Redish, University of Minnesota) in MATLAB. Sorted units were classified as single- or multiunit and single units were validated by the presence of a clear refractory period in the autocorrelogram. LFP data were low-pass filtered at 300 Hz and down-sampled to 1000 Hz for further analysis.

Receptive field mapping. Receptive fields were mapped using a reverse correlation technique. The marmoset was trained to hold fixation on an image (marmoset face, 1 degree of visual angle (DVA) square) presented at the center of the LCD monitor. A drifting Gabor (2° diameter, spatial frequency: 0.5 cycles/degree, temporal frequency 10 cycles/s) appeared at a random position on the monitor between 0° and 18° in azimuth and −15° to 15° in elevation, drifting in one of eight possible directions for 200 ms, after which it disappeared. A new probe then appeared after a random delay drawn from an exponential distribution (mean delay = 40 ms). The sequence repeated until the marmoset broke fixation (defined as an excursion of 1.5° from fixation) or viewed 16 probes. The marmoset was given a juice reward proportional to the number of probes presented. The receptive field for each unit recorded on the array was estimated by calculating the spike-triggered average (STA) stimulus that evoked the maximal response:

$$\mathrm{STA} = \frac{1}{N}\sum_{i=1}^{N} x_i y_i \tag{1}$$

The STA is the sum of probe location x_i weighted by the spike count y_i within the time bin 40–200 ms after probe onset, normalized by the number of all recorded spikes N. We estimated the relative position of each recording array in cortex from the location of estimated receptive fields on each spiking channel, and the known topography of area MT in the marmoset[101] (Fig. 1a). We excluded from the analysis the upper half of monkey W's array as the recordings did not appear to be in area MT.

Behavioral task. The marmosets were trained to saccade to a marmoset face to initiate a trial of a visual detection task. Upon their gaze landing on the face, the face turned into a fixation point (0.15 DVA). The marmosets held fixation on the fixation point (1.5° tolerance) for a minimum duration (400 ms monkey W, 300 ms monkey T) awaiting the appearance of a drifting Gabor. The Gabor target was 4 DVA in diameter, which reliably produced evoked responses in the multiunit spiking activity on 1–2 adjacent electrodes. The Gabor had a spatial frequency of 0.5 cycles/degree, a temporal frequency of 10 cycles/s, and could drift in one of up to 8 possible directions. Spontaneous data were analyzed for the period of fixation preceding the appearance of a target and excluded a period of at least 100 ms following the initial saccade to initiate the trial. Early fixation breaks (defined by the excursion of the eye position from the fixation window) were excluded from the analysis. The target only appeared if fixation was held for an additional random duration beyond the minimum duration. The random duration was drawn from an exponential distribution (mean duration = 200 ms) to generate a flat hazard function.

Relative power between spontaneous and evoked LFP. We calculated the relative power between spontaneous and evoked LFP (forward-reverse filtered with a fourth-order Butterworth at 5–50 Hz) by computing the sum-squared LFP magnitude in a window just after stimulus onset (0–200 ms) divided by sum-squared LFP magnitude just before stimulus onset (−200 to 0 ms) on the electrode retinotopically aligned to the stimulus location in cortex. For LFP values λ_t at this electrode, where $t \in \{\Delta t, 2\Delta t, \ldots, n\Delta t\}$, the relative power P is then

$$P = \frac{\sum_{t_2}^{t_3} \lambda_t^2}{\sum_{t_1}^{t_2} \lambda_t^2} \tag{2}$$

where $t_1 = -200$ ms, $t_2 = 0$, and $t_3 = 200$ ms.

Computational simulations. The model consists of N LIF neurons, with $N_e = 0.8N$ excitatory units and $N_i = 0.2N$ inhibitory. The membrane potential $V^{(i)}$ of the ith neuron evolves according to the equations

$$C_\mathrm{m}\dot{V}^{(i)} = G_\mathrm{L}\left(E_\mathrm{L} - V^{(i)}\right) + g_e^{(i)}\left(E_e - V^{(i)}\right) + g_i^{(i)}\left(E_i - V^{(i)}\right) \tag{3}$$

$$\tau_{\{e,i\}}\dot{g}_{\{e,i\}}^{(i)} = -g_{\{e,i\}}^{(i)} \tag{4}$$

where C_m is the membrane capacitance, G_L is the leak conductance, E_L is the resting membrane potential, $\tau_{\{e,i\}}$ are the excitatory and inhibitory synaptic time constants, $g_{\{e,i\}}{}^{((i))}$ are the time-dependent synaptic conductances of the ith neuron, and $E_{\{e,i\}}$ are the reversal potentials for excitatory and inhibitory synaptic transmission, respectively.

When $V^{(i)}$ exceeds threshold V_T at time t_s, the following spike and reset conditions occur:

$$V^{(i)} \mapsto V_\mathrm{r} \tag{5}$$

$$t_\mathrm{n} = t_\mathrm{s} + \tau^{(i,j)},\ g_{\{e,i\}}^{(j)} \mapsto g_{\{e,i\}}^{(j)} + G_{\{e,i\}}\ \forall j \in [1, K] \tag{6}$$

where V_r is the reset potential, t_n is the time at which the postsynaptic neuron receives its input following axonal and synaptic delays, $G_{\{e,i\}}$ are the excitatory and inhibitory synaptic weights, $g_{\{e,i\}}{}^{((j))}$ are the excitatory and inhibitory conductances of postsynaptic neuron $j \neq i$, respectively, and K is the number of postsynaptic targets of neuron i. Immediately after neuron i spikes, it undergoes a refractory period of τ_r where the membrane potential is not updated.

Network connectivity and axonal conduction delays. We studied spiking network models with unstructured, random connectivity (random networks, Fig. 2a) or topographic, locally random connectivity (topographic networks, Fig. 2d) or a dense version of the topographic network (dense network, Figs. 7 and 8). The $N_e = 0.8N$ excitatory neurons, of indices $1, 2, \ldots, N_e$, where N_e is a square number, are arranged uniformly on a 2D grid. Similarly, the $N_i = 0.2N$ inhibitory neurons, of indices $N_{e+1}, N_{e+2}, \ldots, N$, where N_i is also a square number, are arranged uniformly on a 2D grid. Both grids have side length L and they are concentric, together forming a 2D sheet of the N neurons.

In the random network, connections were randomly and uniformly drawn, and the only delay modeled was that relating to synaptic vesicle release, τ_s, which was short and homogeneous across the network. In the topographic and dense networks, connections were randomly drawn from an isotropic 2D Gaussian probability distribution of zero mean and SD σ in either dimension. σ is 400 µm except in Fig. 6a, where the effect of this parameter was studied systematically. In all networks, there were no self- or double-connections. Axonal conduction delays increased linearly with distance between pre- and postsynaptic cells:

$$\tau^{(i,j)} = \tau_\mathrm{s} + \frac{d^{(i,j)}}{v_\mathrm{c}^{(i,j)}} \tag{7}$$

where $\tau^{(i,j)}$ is the delay from neuron i to neuron j, τ_s is the same delay representing synaptic vesicle release as in the random network, $d^{(i,j)}$ is the Euclidean distance between neurons i and j, and $v_\mathrm{c}{}^{((i,j))}$ is the axonal conduction speed for the connection from neuron i to neuron j. All distances were calculated taking 2D periodic boundary conditions into account, effectively wrapping the network onto a toroidal topology[58,81]. 1D versions of the random and topographic networks were also simulated. The models were the same as in the 2D cases, except the neurons were positioned on a ring of length L with periodic boundary conditions.

Self-sustained activity. Instead of initializing self-sustained activity through a "kick" of external Poisson input spikes[34,35,38], which may induce trace activity correlations, we recorded the state variables of a self-sustained network, including membrane potential ($V^{(i)}$) and conductance ($g_{\{e,i\}}{}^{((i))}$), after a long period (10 s) of simulated self-sustained activity. Taking these distributions as a steady state, we then used the Gaussian approximation (mean and variance) to initialize the membrane potentials and conductances with randomly drawn values in the simulations thereafter. After starting the simulation with these initial conditions, networks with approximately balanced excitation and inhibition exhibit self-sustained, irregular spiking activity. Each simulation ran for 1.2 s, from which we eliminated the first 200 ms from our analysis in case of residual initialization artifacts.

Spike train statistics and the asynchronous-irregular regime. To characterize basic spike train statistics, we randomly selected 5000 neurons in the simulation and measured the mean firing rate, CV (defined as the ratio of the standard variation of the interspike interval to the mean for each neuron that has a minimum of three spikes over the simulation window), and the average pairwise correlation (average Pearson's correlation between spike trains smoothed with a 100 ms window for 1000 randomly selected pairs). To prevent longer simulations with high firing rates during our parallel runs, networks that produced mean firing rates over 25 sp/s had an early exit condition. Simulations were classified as asynchronous irregular if the mean firing rate across all simulated units was >1 and <25 sp/s; the mean CV across all units was >0.7 and <1.4[38,102].

Pairwise spike coherence. Pairwise spike coherence was calculated using multitaper methods[85]. We took the spike trains from the 10 × 10 excitatory neurons comprising the pool for estimating the LFP and an adjacent LFP pool. The 1000 ms of simulation time was broken into 500 ms epochs, stepping 125 ms to cover the full period. The DC component of each unit's spike train was removed, and tapered with a single Slepian taper, giving an effective smoothing of 2.5 Hz for the 500 ms data windows.

To estimate the coherence between two spike trains $x = [x_1\ x_2 \ldots x_i \ldots x_n]$ and $y = [y_1\ y_2 \ldots y_i \ldots y_n]$, we first calculated their FFT spectra $X = [X_1\ X_2 \ldots X_j \ldots X_m]$ and $Y = [Y_1\ Y_2 \ldots Y_j \ldots Y_m]$, respectively, where j denotes the index of spectral frequency. The auto- and cross-spectral densities are calculated as

$$S_j^{xx} = \frac{2\Delta t^2}{T} X_j X_j^* \tag{8}$$

and

$$S_j^{xy} = \frac{2\Delta t^2}{T} X_j Y_j^* \tag{9}$$

respectively, where Δt is the sampling interval, T is the spike train duration, and superscript $*$ denotes complex conjugation. In practice, x and y each represent pools of 100 concurrent spike trains across space. The coherence at a given spectral frequency is calculated as

$$C_j^{xy} = \frac{\left|S_j^{xy}\right|}{\sqrt{S_j^{xx} S_j^{yy}}} \tag{10}$$

This coherence calculation is averaged across ten trials to generate an estimate of the average coherence at each frequency as well as an estimate of the variance. For estimating differences in pairwise coherence across networks, we take the frequency with the maximum coherence in the two networks.

NETSIM software. Simulations were generated using a specialized program called NETSIM (v0.1), which is ~1500 lines of C code (available at http://mullerlab.github.io). Equations in the model were integrated using the forward Euler method with a time step of 0.1 ms. Simulation results were additionally point-checked with shorter timesteps throughout. Random numbers were generated using a C implementation of the ISAAC algorithm[103] (Tom Bartol, personal communication, 2016). To verify the numerical integration in this program, we confirmed the network displayed the correct firing rate for unconnected LIF neurons with varying DC-current injections. We also verified simulations under a simple feed-forward network topology to confirm the accuracy of the simulations. In addition, to ensure reproducibility of our computational simulations[104], we compared results from NETSIM and Brian2 at specific points in the (G_e,G_i) parameter space for the balanced random network model, verifying that the mean firing rate, CV, and cross-correlation were in agreement between the two simulators.

Network parameter scans. In order to identify the excitatory and inhibitory synaptic conductance weights that produced self-sustained and asynchronous-irregular activity, we simulated networks with 50 values of G_e ranging from 0.1 to 5 nS and G_i ranging from 1 to 50 nS for a total of 2500 simulations (Table S2). In order to determine the effect of network scale on the range of these 2500 simulations that produced self-sustained and asynchronous-irregular activity, we repeated these simulations five times with varying parameters of network size, neuron number, and connections per neuron (Table S2). The number of neurons per network size was chosen to maintain a density of 28,125 neurons/mm^2. The number of connections was chosen to maintain the density of connections within the Gaussian used to assign connections across network sizes. For larger networks (> 2 mm), the connection number did not grow with the size of the network, as 99% of the connections occur within 3 SDs of the Gaussian ($\sigma = 400$ µm). In order to run these simulations across all combinations of network size and conductance parameters, we utilized the Extreme Science Engineering Discovery Environment Comet cluster at the San Diego SuperComputer center at UC San Diego. Data analysis for these simulations was also performed on the Comet cluster running MATLAB. Circular variables were analyzed using the Circular Statistics Toolbox.

Calculation of LFP estimate. We utilized a previously developed proxy for the LFP generated by a network of point LIF neurons, which was systematically developed from a spatially extended model[39]. The LFP estimate $\lambda(t)$ is computed as a weighted sum of the excitatory and inhibitory synaptic currents I_e and I_i across m excitatory cells in each 10×10 neuron pool:

$$\lambda(t) = \sum_{j=1}^{m} I_e^{(j)}(t-\tau) - \alpha \sum_{j=1}^{m} I_i^{(j)}(t) \tag{11}$$

where $\tau = 6$ ms, $\alpha = 1.65$, and $m = 100$ excitatory cells. These values of τ and α were found by the authors to have an optimal agreement with the LFP generated from a three-dimensional model of spatially extended multi-compartment model neurons[39] and are the values used here. Here, we computed the LFP using the pooled excitatory and inhibitory synaptic conductances and the driving force between the mean pooled membrane potential and the synaptic reversal potential to calculate the average current in the pool. We verified that this approach was nearly precisely equivalent to the proxy calculated using synaptic inputs to each individual neuron in the pool. This LFP proxy is then computed for each 10×10 neuron pool across the 2D network. The LFP proxy was thus independent across each spatial pool, unlike cortical recordings where LFP signals show varying frequency-dependent scales of spatial integration[105]. We note that excluding these effects is a conservative step, as the addition of spatial integration would only increase traveling waves in the LFP. Further, we note that our results do not depend critically on the choice of LFP proxy and our conclusions are unchanged when analyzing the mean membrane potentials or excitatory synaptic conductances.

In order to compare the properties of waves in our model, where LFP signals are independent across space, with waves recorded from the cortex, where electrodes pool signals across a volume ~250 µm in radius[29,106], we convolved the LFP with a 2D Gaussian kernel (with a spatial standard deviation of four LFP bins, corresponding to a radius of 272 µm) before further analysis.

Analysis of spatiotemporal dynamics. To analyze spatiotemporal dynamics in the population activity produced by the spiking network model, we used a technique we recently developed for the wideband analysis of nonstationary data. Briefly, for each real-valued time series $\lambda_{(x,y)}\ (t)\ \forall\, x \in [1,N_{\mathrm{c}}], y \in [1,N_{\mathrm{r}}]$, where N_{c} and N_{r} are the numbers of columns and rows, respectively, we compute the GP $\phi_{(x,y)}$ of the wideband filtered LFP (fourth-order Butterworth from 5 to 100 Hz) at each point using the corrected analytic signal representation introduced in recent work[17]. We next calculated the gradient of GP $\mathrm{g}_{(x,y)}(t)$ at each moment in time:

$$\mathrm{g}_{x,y}(t) = -\nabla\phi_{x,y}(t) \tag{12}$$

For the spatial gradient, derivatives are taken across the two dimensions of space and are approximated by the appropriate forward and centered finite differences (formulas and code available in the wave MATLAB toolbox: https://github.com/mullerlab/wave-MATLAB/blob/master/analysis/phase_gradient_complex_multiplication.m). As in previous work, phase differences were implemented as multiplications in the complex plane[44,107],

$$\Delta\phi_n = \arg\left[\Lambda_{n+1}\Lambda_n^*\right] \tag{13}$$

so that the unwrapping phase across the two dimensions of the network was not necessary. Here, Λ is the analytic signal representation of $\lambda(t)$. Wavelength is the reciprocal of the phase gradient magnitude at each point in space and time:

$$\nu_{x,y} = \frac{1}{\left|\mathrm{g}_{x,y}\right|} \tag{14}$$

As specified in the main text, significance was determined at each point in space and time by comparing observed wavelengths to a spatial shuffle of electrode positions, with the 99th percentile of the shuffle distribution serving as a threshold. The fraction of wave state (Fig. 4a) is the ratio between points with detected waves over all points $\alpha_{w/\alpha}$, where α_w is the number of points with detected waves and α is the total number of points tested.

Wave speed $s(t)$ was computed as the ratio of instantaneous frequency to phase gradient magnitude[96],

$$s(t) = \frac{\frac{\partial\phi}{\partial t}}{\left|\mathrm{g}_{x,y}\right|} \tag{15}$$

We further analyzed the spatiotemporal activity patterns using a 2D spectral decomposition in space and time (Figs. 3b and 5b). To do this, we calculated the 2D FFT of $\lambda_{(x,y)}\ (t)$ for each 1D slice through the network by transforming first in space, and then in time. To account for the spatial and temporal autocorrelation in the data, each slice's spectrum was normalized by dividing the spectrum produced from a spatial and temporal shuffle respectively. This normalization allows visualization of the spectral line representing traveling waves in the network LFP; it is important to note, however, that the spectral peak representing traveling waves is nevertheless clear in the raw spectrum. The normalized spectrum for each slice through the network was then averaged together.

Calculation of response gain. To quantify the sensitivity of the sparse- and dense-wave network regimes to incoming stimulation, we first identified depolarized and hyperpolarized states from the LFP of a 0.2×0.2 mm^2 neuron pool defined by the spike-phase bins that generated the maximum or minimum spiking probability, respectively, for each network regime. We then applied feed-forward stimulation of 20-Hz Poisson spiking inputs to 100 synapses for each neuron within the pool for 10 ms, aligned to the depolarized or hyperpolarized phase in the network. This process was repeated across 40 trials, yielding a distribution of evoked responses. The same random seed was used to construct the networks across each trial, so that the simulations were identical up to the point of stimulation. We calculated the sum of firing rate during stimulus for the evoked response divided by that of the no-stimulus case.

Calculation of the spike-phase index. The degree of spike-phase coupling was measured as the mean resultant vector length for the LFP (filtered with a forward-reverse fourth-order Butterworth filter from 5 to 100 Hz) phase distribution from observed spike times. This measure was calculated using the circ_r function in the Circular Statistics Toolbox for MATLAB (P. Berens, CircStat: A MATLAB Toolbox for Circular Statistics, Journal of Statistical Software, Volume 31, Issue 10, 2009). The mean resultant r of the spike-phase distribution is the normalized sum over complex exponentials of the phase angles ϕ_j,

$$r = \frac{1}{M}\sum_{j=1}^{M} e^{\mathrm{i}\phi_j} \tag{16}$$

where M is the number of spikes, the modulus of r ($|r| \in [0,1]$) represents the degree of spike-phase modulation, and $i^2 = -1$. The closer r is to 0, the more uniform the phase distribution. The closer it is to 1, the more concentrated the phases.

Statistics and reproducibility. Experimental results from in vivo electrophysiology were generated in an initial monkey and replicated in a second monkey with a similar result. All analyses that stemmed from previous experimental work were reproduced from newly written analysis code. Network simulations and subsequent data analysis including statistical tests were initially generated and then repeated on separate machines across different institutes to ensure the reproducibility of the results.

Reporting summary. Further information on research design is available in the Nature Research Reporting Summary linked to this article.

Data availability

Access to the raw simulation data and the processed electrophysiology data used in this study are available at https://github.com/mullerlab/davis2021ncomms. Source data are provided with this paper.

Code availability

An open-source code repository for all analysis methods is available on https://github.com/mullerlab/davis2021ncomms. The open-source code for the custom simulation framework NETSIM is available at https://github.com/mullerlab/NETSIM.

Received: 22 November 2020; Accepted: 17 September 2021;
Published online: 18 October 2021

Reference

1. Croner, L. J., Purpura, K. & Kaplan, E. Response variability in retinal ganglion cells of primates. *Proc. Natl. Acad. Sci. USA* **90**, 8128–8130 (1993).
2. Mainen, Z. F. & Sejnowski, T. J. Reliability of spike timing in neocortical neurons. *Science* **268**, 1503–1506 (1995).
3. Destexhe, A., Rudolph, M. & Paré, D. The high-conductance state of neocortical neurons in vivo. *Nat. Rev. Neurosci.* **4**, 739–751 (2003).
4. Destexhe, A. & Rudolph-Lilith, M. *Neuronal Noise* (Springer US, 2012).
5. Shadlen, M. N. & Newsome, W. T. Noise, neural codes and cortical organization. *Curr. Opin. Neurobiol.* **4**, 569–579 (1994).
6. Arieli, A., Sterkin, A., Grinvald, A. & Aertsen, A. Dynamics of ongoing activity: explanation of the large variability in evoked cortical responses. *Science* **273**, 1868–1871 (1996).

7. Tsodyks, M., Kenet, T., Grinvald, A. & Arieli, A. Linking spontaneous activity of single cortical neurons and the underlying functional architecture. *Science* **286**, 1943–1946 (1999).
8. Kenet, T., Bibitchkov, D., Tsodyks, M., Grinvald, A. & Arieli, A. Spontaneously emerging cortical representations of visual attributes. *Nature* **425**, 954–956 (2003).
9. Han, F., Caporale, N. & Dan, Y. Reverberation of recent visual experience in spontaneous cortical waves. *Neuron* **60**, 321–327 (2008).
10. Ermentrout, G. B. & Kleinfeld, D. Traveling Electrical Waves in Cortex. *Neuron* **29**, 33–44 (2001).
11. Santos, E. et al. Radial, spiral and reverberating waves of spreading depolarization occur in the gyrencephalic brain. *Neuroimage* **99**, 244–255 (2014).
12. Benucci, A., Frazor, R. A. & Carandini, M. Standing waves and traveling waves distinguish two circuits in visual cortex. *Neuron* **55**, 103–117 (2007).
13. Petersen, C. C. H., Hahn, T. T. G., Mehta, M., Grinvald, A. & Sakmann, B. Interaction of sensory responses with spontaneous depolarization in layer 2/3 barrel cortex. *Proc. Natl Acad. Sci. USA* **100**, 13638–13643 (2003).
14. Destexhe, A., Contreras, D. & Steriade, M. Spatiotemporal analysis of local field potentials and unit discharges in cat cerebral cortex during natural wake and sleep states. *J. Neurosci.* **19**, 4595–4608 (1999).
15. Churchland, M. M. et al. Stimulus onset quenches neural variability: a widespread cortical phenomenon. *Nat. Neurosci.* **13**, 369–378 (2010).
16. Sato, T. K., Nauhaus, I. & Carandini, M. Traveling waves in visual cortex. *Neuron* **75**, 218–229 (2012).
17. Davis, Z. W., Muller, L., Martinez-Trujillo, J., Sejnowski, T. & Reynolds, J. H. Spontaneous travelling cortical waves gate perception in behaving primates. *Nature* https://doi.org/10.1038/s41586-020-2802-y (2020).
18. El Boustani, S., Pospischil, M., Rudolph-Lilith, M. & Destexhe, A. Activated cortical states: experiments, analyses and models. *J. Physiol. Paris* **101**, 99–109 (2007).
19. Nandy, A., Nassi, J. J., Jadi, M. P. & Reynolds, J. Optogenetically induced low-frequency correlations impair perception. *Elife* **8**, e35123 (2019).
20. Destexhe, A. & Contreras, D. Neuronal computations with stochastic network states. *Science* **314**, 85–90 (2006).
21. Renart, A. et al. The asynchronous state in cortical circuits. *Science* **327**, 587–590 (2010).
22. Fiser, J., Chiu, C. & Weliky, M. Small modulation of ongoing cortical dynamics by sensory input during natural vision. *Nature* **431**, 573–578 (2004).
23. Luczak, A., Bartho, P. & Harris, K. D. Gating of sensory input by spontaneous cortical activity. *J. Neurosci.* **33**, 1684–1695 (2013).
24. Gutnisky, D. A., Beaman, C. B., Lew, S. E. & Dragoi, V. Spontaneous Fluctuations in Visual Cortical Responses Influence Population Coding Accuracy. *Cereb. Cortex* https://doi.org/10.1093/cercor/bhv312 (2016).
25. Destexhe, A., Rudolph, M., Fellous, J. M. & Sejnowski, T. J. Fluctuating synaptic conductances recreate in vivo-like activity in neocortical neurons. *Neuroscience* **107**, 13–24 (2001).
26. Chance, F. S., Abbott, L. F. & Reyes, A. D. Gain modulation from background synaptic input. *Neuron* **35**, 773–782 (2002).
27. Tomko, G. J. & Crapper, D. R. Neuronal variability: non-stationary responses to identical visual stimuli. *Brain Res.* **79**, 405–418 (1974).
28. Shadlen, M. N. & Newsome, W. T. The variable discharge of cortical neurons: implications for connectivity, computation, and information coding. *J. Neurosci.* **18**, 3870–3896 (1998).
29. Katzner, S. et al. Local origin of field potentials in visual cortex. *Neuron* **61**, 35–41 (2009).
30. Lindén, H. et al. Modeling the spatial reach of the LFP. *Neuron* **72**, 859–872 (2011).
31. Abbott, L. F. & van Vreeswijk, C. Asynchronous states in networks of pulse-coupled oscillators. *Phys. Rev. E Stat. Phys. Plasmas Fluids Relat. Interdiscip. Topics* **48**, 1483–1490 (1993).
32. Brunel, N. Dynamics of sparsely connected networks of excitatory and inhibitory spiking neurons. *J. Comput. Neurosci.* **8**, 183–208 (2000).
33. Softky, W. R. & Koch, C. The highly irregular firing of cortical cells is inconsistent with temporal integration of random EPSPs. *J. Neurosci.* **13**, 334–350 (1993).
34. Vogels, T. P. & Abbott, L. F. Signal propagation and logic gating in networks of integrate-and-fire neurons. *J. Neurosci.* **25**, 10786–10795 (2005).
35. Kumar, A., Schrader, S., Aertsen, A. & Rotter, S. The high-conductance state of cortical networks. *Neural Comput.* **20**, 1–43 (2008).
36. Binzegger, T., Douglas, R. J. & Martin, K. A. C. A quantitative map of the circuit of cat primary visual cortex. *J. Neurosci.* **24**, 8441–8453 (2004).
37. Atapour, N. et al. Neuronal Distribution Across the Cerebral Cortex of the Marmoset Monkey (Callithrix jacchus). *Cereb. Cortex* **29**, 3836–3863 (2019).
38. Destexhe, A. Self-sustained asynchronous irregular states and Up-Down states in thalamic, cortical and thalamocortical networks of nonlinear integrate-and-fire neurons. *J. Comput. Neurosci.* **27**, 493–506 (2009).
39. Mazzoni, A. et al. Computing the Local Field Potential (LFP) from Integrate-and-Fire Network Models. *PLoS Comput. Biol.* **11**, e1004584 (2015).
40. Hellwig, B. A quantitative analysis of the local connectivity between pyramidal neurons in layers 2/3 of the rat visual cortex. *Biol. Cybern.* **82**, 111–121 (2000).
41. Levy, R. B. & Reyes, A. D. Spatial profile of excitatory and inhibitory synaptic connectivity in mouse primary auditory cortex. *J. Neurosci.* **32**, 5609–5619 (2012).
42. Girard, P., Hupé, J. M. & Bullier, J. Feedforward and feedback connections between areas V1 and V2 of the monkey have similar rapid conduction velocities. *J. Neurophysiol.* **85**, 1328–1331 (2001).
43. Cagigal, M. P., Vega, L. & Prieto, P. Movement characterization with the spatiotemporal Fourier transform of low-light-level images. *Appl. Opt.* **34**, 1769–1774 (1995).
44. Muller, L., Reynaud, A., Chavane, F. & Destexhe, A. The stimulus-evoked population response in visual cortex of awake monkey is a propagating wave. *Nat. Commun.* **5**, 3675 (2014).
45. Muller, L. et al. Rotating waves during human sleep spindles organize global patterns of activity that repeat precisely through the night. *Elife* **5**, e17267 (2016).
46. Stettler, D. D., Das, A., Bennett, J. & Gilbert, C. D. Lateral connectivity and contextual interactions in macaque primary visual cortex. *Neuron* **36**, 739–750 (2002).
47. Angelucci, A. et al. Circuits for local and global signal integration in primary visual cortex. *J. Neurosci.* **22**, 8633–8646 (2002).
48. Bringuier, V., Chavane, F., Glaeser, L. & Frégnac, Y. Horizontal propagation of visual activity in the synaptic integration field of area 17 neurons. *Science* **283**, 695–699 (1999).
49. Gonzalez-Burgos, G., Barrionuevo, G. & Lewis, D. A. Horizontal Synaptic Connections in Monkey Prefrontal Cortex. *Cerebral Cortex* **10**, 82–92 (2000).
50. Kuhn, A., Aertsen, A. & Rotter, S. Neuronal integration of synaptic input in the fluctuation-driven regime. *J. Neurosci.* **24**, 2345–2356 (2004).
51. DeWeese, M. R. & Zador, A. M. Non-Gaussian membrane potential dynamics imply sparse, synchronous activity in auditory cortex. *J. Neurosci.* **26**, 12206–12218 (2006).
52. Hirsch, J. A. & Gilbert, C. D. Synaptic physiology of horizontal connections in the cat's visual cortex. *J. Neurosci.* **11**, 1800–1809 (1991).
53. Frégnac, Y., Bringuier, V. & Chavane, F. Synaptic integration fields and associative plasticity of visual cortical cells in vivo. *J. Physiol. Paris* **90**, 367–372 (1996).
54. Frégnac, Y. Reading Out the Synaptic Echoes of Low-Level Perception inV1. in *Computer Vision – ECCV2012.* Workshops and Demonstrations 486–495 (Springer Berlin Heidelberg, 2012).
55. Gerard-Mercier, F., Carelli, P. V., Pananceau, M., Troncoso, X. G. & Frégnac, Y. Synaptic Correlates of Low-Level Perception in V1. *J. Neurosci.* **36**, 3925–3942 (2016).
56. Destexhe, A. Oscillations, complex spatiotemporal behavior, and information transport in networks of excitatory and inhibitory neurons. *Phys. Rev. E Stat. Phys. Plasmas Fluids Relat. Interdiscip. Topics* **50**, 1594–1606 (1994).
57. Zerlaut, Y. & Destexhe, A. Enhanced Responsiveness and Low-Level Awareness in Stochastic Network States. *Neuron* **94**, 1002–1009 (2017).
58. Mehring, C., Hehl, U., Kubo, M., Diesmann, M. & Aertsen, A. Activity dynamics and propagation of synchronous spiking in locally connected random networks. *Biol. Cybern.* **88**, 395–408 (2003).
59. Crook, S. M., Ermentrout, G. B., Vanier, M. C. & Bower, J. M. The role of axonal delay in the synchronization of networks of coupled cortical oscillators. *J. Comput. Neurosci.* **4**, 161–172 (1997).
60. Golomb, D. & Ermentrout, G. B. Continuous and lurching traveling pulses in neuronal networks with delay and spatially decaying connectivity. *Proc. Natl Acad. Sci. USA* **96**, 13480–13485 (1999).
61. Golomb, D. & Ermentrout, G. B. Effects of delay on the type and velocity of travelling pulses in neuronal networks with spatially decaying connectivity. *Network* **11**, 221–246 (2000).
62. Osan, R. & Ermentrout, B. Two dimensional synaptically generated traveling waves in a theta-neuron neural network. *Neurocomputing* **38**, 789–795 (2001).
63. Roxin, A., Brunel, N. & Hansel, D. Role of delays in shaping spatiotemporal dynamics of neuronal activity in large networks. *Phys. Rev. Lett.* **94**, 238103 (2005).
64. Roxin, A., Brunel, N. & Hansel, D. Rate Models with Delays and the Dynamics of Large Networks of Spiking Neurons. *Progr. Theoret. Phys. Suppl.* **161**, 68–85 (2006).
65. Kriener, B., Helias, M., Aertsen, A. & Rotter, S. Correlations in spiking neuronal networks with distance dependent connections. *J. Comput. Neurosci.* **27**, 177–200 (2009).
66. Kriener, B., Helias, M., Rotter, S., Diesmann, M. & Einevoll, G. T. How pattern formation in ring networks of excitatory and inhibitory spiking neurons depends on the input current regime. *Front. Comput. Neurosci.* **7**, 187 (2013).
67. Senk, J. et al. Conditions for wave trains in spiking neural networks. *Phys. Rev. Research* **2**, 023174 (2020).
68. Ermentrout, B. Neural networks as spatio-temporal pattern-forming systems. *Rep. Prog. Phys.* **61**, 353–430 (1998).

69. Bressloff, P. C. Traveling waves and pulses in a one-dimensional network of excitable integrate-and-fire neurons. *J. Math. Biol.* **40**, 169–198 (2000).
70. Pinto, D. & Ermentrout, G. Spatially Structured Activity in Synaptically Coupled Neuronal Networks: I. Traveling Fronts and Pulses. *SIAM J. Appl. Math.* **62**, 206–225 (2001).
71. Liley, D. T. J., Cadusch, P. J. & Dafilis, M. P. A spatially continuous mean field theory of electrocortical activity. *Network* **13**, 67–113 (2002).
72. Coombes, S., Lord, G. J. & Owen, M. R. Waves and bumps in neuronal networks with axo-dendritic synaptic interactions. *Physica D* **178**, 219–241 (2003).
73. Atay, F. M. & Hutt, A. Stability and Bifurcations in Neural Fields with Finite Propagation Speed and General Connectivity. *SIAM J. Appl. Math.* **65**, 644–666 (2004).
74. Venkov, N. A., Coombes, S. & Matthews, P. C. Dynamic instabilities in scalar neural field equations with space-dependent delays. *Physica D* **232**, 1–15 (2007).
75. Veltz, R. Interplay Between Synaptic Delays and Propagation Delays in Neural Field Equations. *SIAM J. Appl. Dyn. Syst.* **12**, 1566–1612 (2013).
76. Meijer, H. G. E. & Coombes, S. Travelling waves in models of neural tissue: from localised structures to periodic waves. *EPJ Nonlinear Biomedical Physics* **2**, 3 (2014).
77. Visser, S., Nicks, R., Faugeras, O. & Coombes, S. Standing and travelling waves in a spherical brain model: The Nunez model revisited. *Physica D* **349**, 27–45 (2017).
78. Gong, P. & van Leeuwen, C. Distributed dynamical computation in neural circuits with propagating coherent activity patterns. *PLoS Comput. Biol.* **5**, e1000611 (2009).
79. Keane, A. & Gong, P. Propagating waves can explain irregular neural dynamics. *J. Neurosci.* **35**, 1591–1605 (2015).
80. Huang, C. et al. Circuit Models of Low-Dimensional Shared Variability in Cortical Networks. *Neuron* **101**, 337–348.e4 (2019).
81. Kumar, A., Rotter, S. & Aertsen, A. Conditions for propagating synchronous spiking and asynchronous firing rates in a cortical network model. *J. Neurosci.* **28**, 5268–5280 (2008).
82. Brunel, N. & Hakim, V. Fast global oscillations in networks of integrate-and-fire neurons with low firing rates. *Neural Comput.* **11**, 1621–1671 (1999).
83. Brunel, N. & Wang, X.-J. What Determines the Frequency of Fast Network Oscillations With Irregular Neural Discharges? I. Synaptic Dynamics and Excitation-Inhibition Balance. *Journal of Neurophysiology* **90**, 415–430 (2003).
84. Palmigiano, A., Geisel, T., Wolf, F. & Battaglia, D. Flexible information routing by transient synchrony. *Nat. Neurosci.* https://doi.org/10.1038/nn.4569 (2017).
85. Mitchell, J. F., Sundberg, K. A. & Reynolds, J. H. Spatial attention decorrelates intrinsic activity fluctuations in macaque area V4. *Neuron* **63**, 879–888 (2009).
86. Zohary, E., Shadlen, M. N. & Newsome, W. T. Correlated neuronal discharge rate and its implications for psychophysical performance. *Nature* **370**, 140–143 (1994).
87. Abbott, L. F. & Dayan, P. The Effect of Correlated Variability on the Accuracy of a Population Code. *Neural Computation* **11**, 91–101 (1999).
88. Averbeck, B. B., Latham, P. E. & Pouget, A. Neural correlations, population coding and computation. *Nat. Rev. Neurosci.* **7**, 358–366 (2006).
89. Cohen, M. R. & Maunsell, J. H. R. Attention improves performance primarily by reducing interneuronal correlations. *Nat. Neurosci.* **12**, 1594–1600 (2009).
90. Rudolph, M., Pospischil, M., Timofeev, I. & Destexhe, A. Inhibition determines membrane potential dynamics and controls action potential generation in awake and sleeping cat cortex. *J. Neurosci.* **27**, 5280–5290 (2007).
91. Morrison, A., Aertsen, A. & Diesmann, M. Spike-Timing-Dependent Plasticity in Balanced Random Networks. *Neural Computation* **19**, 1437–1467 (2007).
92. Reinhold, K., Lien, A. D. & Scanziani, M. Distinct recurrent versus afferent dynamics in cortical visual processing. *Nat. Neurosci.* **18**, 1789–1797 (2015).
93. Guo, Z. V. et al. Maintenance of persistent activity in a frontal thalamocortical loop. *Nature* **545**, 181–186 (2017).
94. Yang, Z., Heeger, D. J., Blake, R. & Seidemann, E. Long-range traveling waves of activity triggered by local dichoptic stimulation in V1 of behaving monkeys. *J. Neurophysiol.* **113**, 277–294 (2015).
95. Chemla, S. et al. Suppressive Traveling Waves Shape Representations of Illusory Motion in Primary Visual Cortex of Awake Primate. *J. Neurosci.* **39**, 4282–4298 (2019).
96. Rubino, D., Robbins, K. A. & Hatsopoulos, N. G. Propagating waves mediate information transfer in the motor cortex. *Nat. Neurosci.* **9**, 1549–1557 (2006).
97. Zanos, T. P., Mineault, P. J., Nasiotis, K. T., Guitton, D. & Pack, C. C. A sensorimotor role for traveling waves in primate visual cortex. *Neuron* **85**, 615–627 (2015).
98. Balasubramanian, K. et al. Propagating Motor Cortical Dynamics Facilitate Movement Initiation. *Neuron* **106**, 526–536.e4 (2020).
99. Braitenberg, V. & Schüz, A. *Cortex: Statistics and Geometry of Neuronal Connectivity*. (Springer, 1998).
100. Markov, N. T. et al. Weight consistency specifies regularities of macaque cortical networks. *Cereb. Cortex* **21**, 1254–1272 (2011).
101. Rosa, M. G. P. & Elston, G. N. Visuotopic organisation and neuronal response selectivity for direction of motion in visual areas of the caudal temporal lobe of the marmoset monkey (Callithrix jacchus): middle temporal area, middle temporal crescent, and surrounding cortex. *J. Comp. Neurol.* **393**, 505–527 (1998).
102. Voges, N. & Perrinet, L. Complex dynamics in recurrent cortical networks based on spatially realistic connectivities. *Front. Comput. Neurosci.* **6**, 41 (2012).
103. Jenkins, R. J. ISAAC. in *Fast Software Encryption* 41–49 (Springer Berlin Heidelberg, 1996).
104. Davison, A. P. et al. PyNN: A Common Interface for Neuronal Network Simulators. *Front. Neuroinform.* **2**, 11 (2008).
105. Łęski, S., Lindén, H., Tetzlaff, T., Pettersen, K. H. & Einevoll, G. T. Frequency dependence of signal power and spatial reach of the local field potential. *PLoS Comput. Biol.* **9**, e1003137 (2013).
106. Buzsáki, G., Anastassiou, C. A. & Koch, C. The origin of extracellular fields and currents—EEG, ECoG, LFP and spikes. *Nat. Rev. Neurosci.* **13**, 407–420 (2012).
107. Feldman, M. Hilbert transform in vibration analysis. *Mech. Syst. Signal Process.* **25**, 735–802 (2011/4).

Acknowledgements

We thank Katie Williams, Sean Adams, and Mat LeBlanc for their contributions to this project, in addition to the San Diego Supercomputer Center for their support for this project. We would also like to thank Tom Bartol for the discussions on the software implementation. This work was funded by Gatsby Charitable Foundation, the Fiona and Sanjay Jha Chair in Neuroscience, the Canadian Institute for Health Research and NSF (NeuroNex Grant No. 2015276), the Swartz Foundation, NIH Grants R01-EY028723, T32 EY020503-06, T32 MH020002-16A, P30 EY019005, and BrainsCAN at Western University through the Canada First Research Excellence Fund (CFREF).

Author contributions

Conceptualization: Z.W.D., G.B.B., C.F., T.D., T.J.S., J.H.R., L.M.; data curation: Z.W.D., G.B.B. C.F., T.D., C.S., L.M.; formal analysis: Z.W.D., G.B.B., C.F., T.D., L.M.; funding acquisition: Z.W.D., T.J.S., J.H.R., L.M.; investigation: Z.W.D., G.B.B., L.M.; methodology: Z.W.D., G.B.B., C.F., T.S., C.S., J.H.R., L.M.; supervision: T.J.S., J.H.R., L.M.; visualization: Z.W.D., G.B.B., L.M.; writing—original draft, Z.W.D., G.B.B., C.F., T.D., J.H.R., L.M.; writing—review and editing, Z.W.D., G.B.B., T.J.S., J.H.R., L.M.

Competing interests

The authors declare no competing interests.

Additional information

Supplementary information The online version contains supplementary material available at https://doi.org/10.1038/s41467-021-26175-1.

Correspondence and requests for materials should be addressed to Zachary W. Davis, John H. Reynolds or Lyle Muller.

Peer review information *Nature Communications* thanks Bastian Pietras and the other, anonymous, reviewer(s) for their contribution to the peer review of this work. Peer reviewer reports are available.

Reprints and permission information is available at http://www.nature.com/reprints

Publisher's note Springer Nature remains neutral with regard to jurisdictional claims in published maps and institutional affiliations.

Open Access This article is licensed under a Creative Commons Attribution 4.0 International License, which permits use, sharing, adaptation, distribution and reproduction in any medium or format, as long as you give appropriate credit to the original author(s) and the source, provide a link to the Creative Commons license, and indicate if changes were made. The images or other third party material in this article are included in the article's Creative Commons license, unless indicated otherwise in a credit line to the material. If material is not included in the article's Creative Commons license and your intended use is not permitted by statutory regulation or exceeds the permitted use, you will need to obtain permission directly from the copyright holder. To view a copy of this license, visit http://creativecommons.org/licenses/by/4.0/.

© The Author(s) 2021

Supplementary Information

Supplementary Figure 1

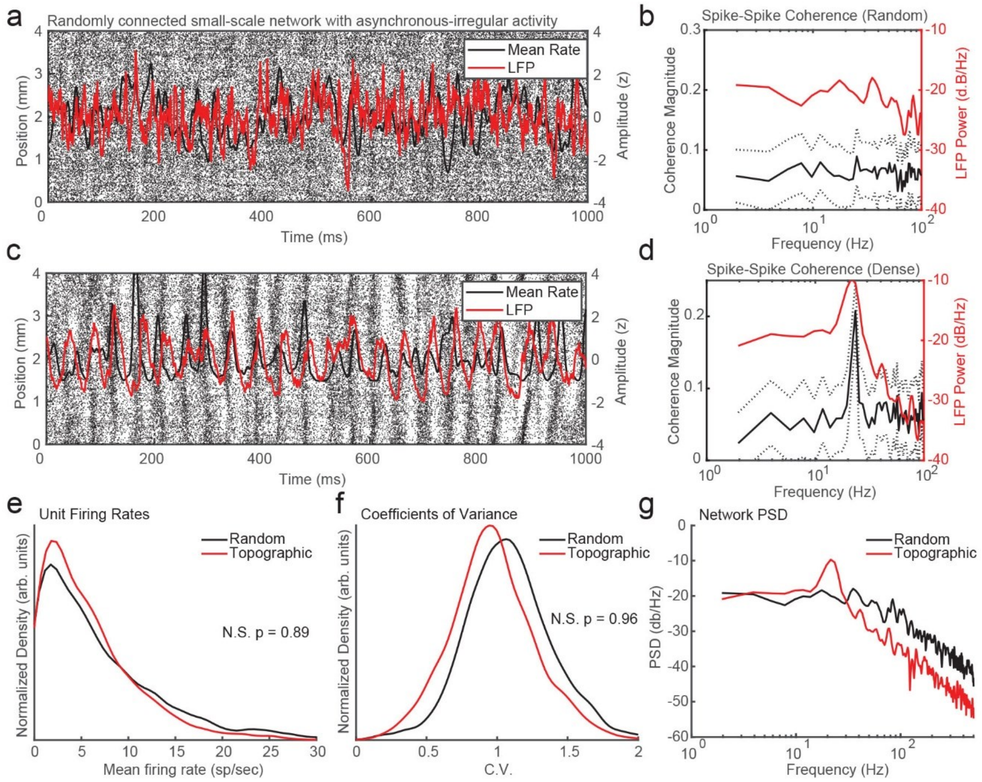

Figure S1. Dense spiking waves induce pairwise correlation in a small-scale spiking network. (a) Spike rasters from 10,000 neurons in a small-scale network simulation with random connections and no delays producing asynchronous-irregular spiking dynamics. The mean firing rate and LFP for a single 100 neuron LFP pool is plotted in black and red respectively. (b) Pairwise spike coherence (black line) and power spectral density (red line) for LFP pools in (a). Dotted lines denote the 95% confidence interval of the mean. (c) Spike rasters as in (a), but with topographic connections and transmission delays (0.2 m/s). (d) Coherence and PSD as in (b) but for the network shown in (c). Dense spike participation in waves generates strong coherence at the dominant frequency of fluctuations in the network. (e) There was no difference in the distribution of unit mean firing rates between the random (black) and topographic (red) small-scale networks (N = 5000 units; p = 0.89; two-sided Kolmogorov–Smirnov test). (f) There was no significant difference in the distribution of unit C.Vs between the random and topographic small-scale

networks (N = 3319 units; p = 0.96; two-sided Kolmogorov–Smirnov test). (g) Comparison of the PSD between the random and topographic small-scale networks.

Supplementary Figure 2

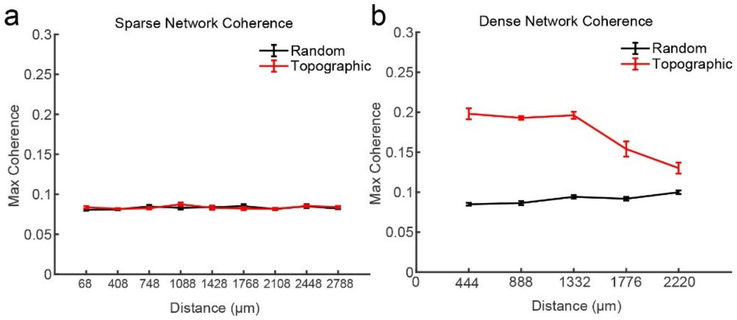

Figure S2. Distance dependence of pairwise spike coherence. (a) The maximum pairwise spike coherence calculated between neuron pools at various distances in the random (black) and topographic (red) large-scale networks in Figure 2. There was no change in spike coherence in either network at any distance. (b) Same as (a), but for the small-scale networks in Figure S1. There was a negative correlation with maximum spike coherence and distance in the small-scale topographic model (N = 10 resamples, error bars indicate S. E. M.; Pearson’s r = -0.72).

Supplementary Figure 3

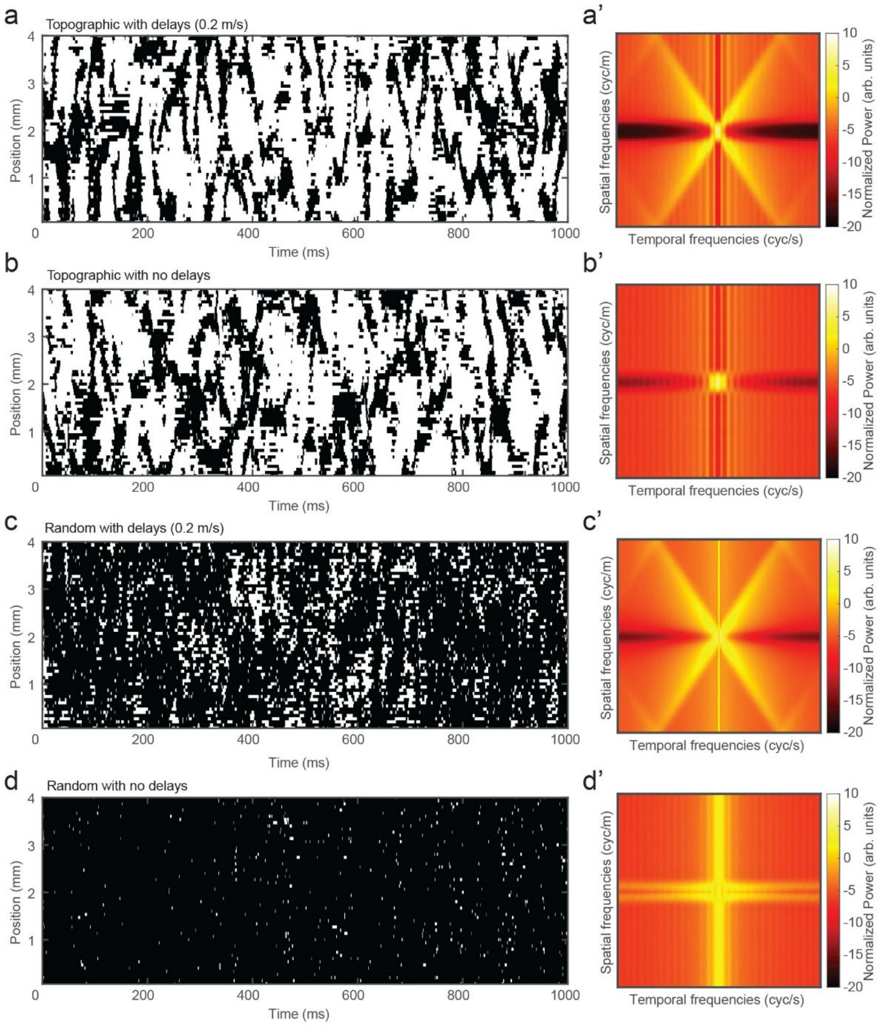

Figure S3. Topographic connections and distance-dependent delays combined are necessary to generate traveling waves. (a) Significant (white) and non-significant (black) wavelength values for each position in a linear slice through a large-scale 2D network simulation with topographic connections and no delays. (a') 2-D (space-time) FFT shows a concentration of spectral power corresponding to waves traveling at the velocity corresponding to propagation speeds (0.2 m/s). (b, b') Same as in (a), but for a network with topographic connectivity and no delays. Topographic connectivity is sufficient to generate significant spatially organized wavelengths. However, without delays, the spectral power does not concentrate along a joint spatial and temporal frequency band consistent with traveling waves. (c, c') Wavelengths and spatiotemporal FFT for

a randomly connected network with delays. With random connectivity the network lacks strong spatial organization while delays are sufficient for the spatiotemporal flow of activity. (d, d’). Wavelengths and spatiotemporal FFT for a randomly connected network without delays. There is no spatial or temporal structure in this network suggestive of any wave activity.

Supplementary Figure 4

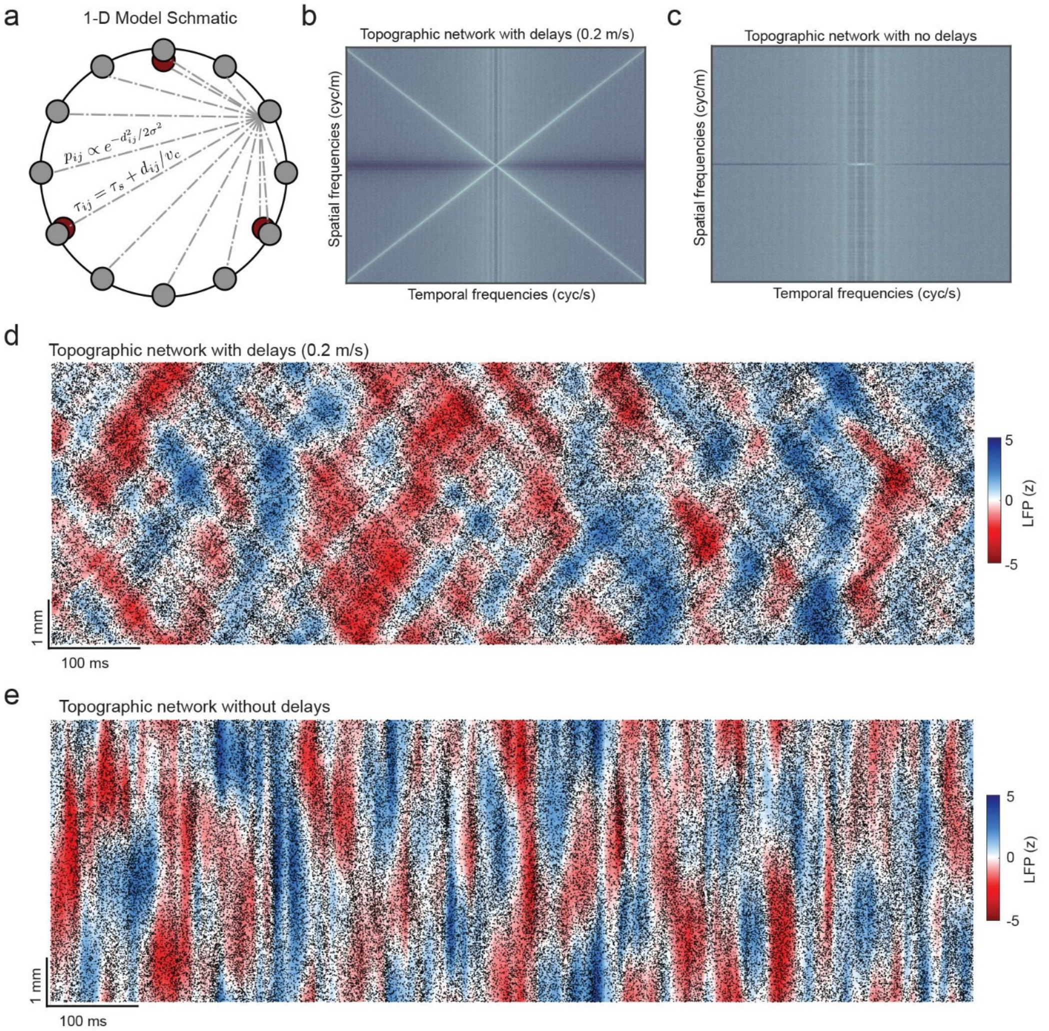

Figure S4. Delays are necessary for robust traveling waves in 1-D spiking network model. (a) Schematic of 1-D network model. 450,000 neurons were arranged on a ring with topographic connection probabilities and distance dependent delays. (b) 2-D FFT of the spatial (y-axis) and temporal (x-axis) frequencies of activity in the topographic network. The clear spectral line is consistent with waves traveling at 0.2 m/s. (c) No spectral line appears in a similar topographic 1D network without delays. (d) Spike rasters and LFP amplitude (pseudocolor) for the topographic network displays waves moving across space over time in the 1-D topographically connected network with delays. (e) Same as (d), but for the 1-D topographic network without

delays. LFP fluctuations do not travel as waves but rather occur synchronously across regions of the network.

Supplementary Figure 5

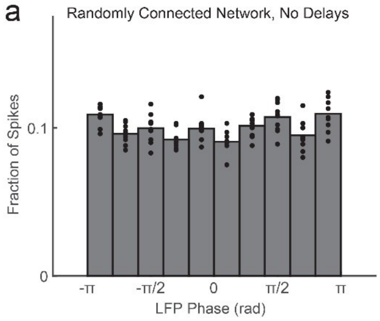

Figure S5. Randomly-connected spiking network model has weak spike-LFP phase coupling. (a) Histogram showing the fraction of spikes that occurred during each phase of the LFP in the randomly connected network shown in Figure 2a (N = 10 resamples; circular-resultant = 0.03).

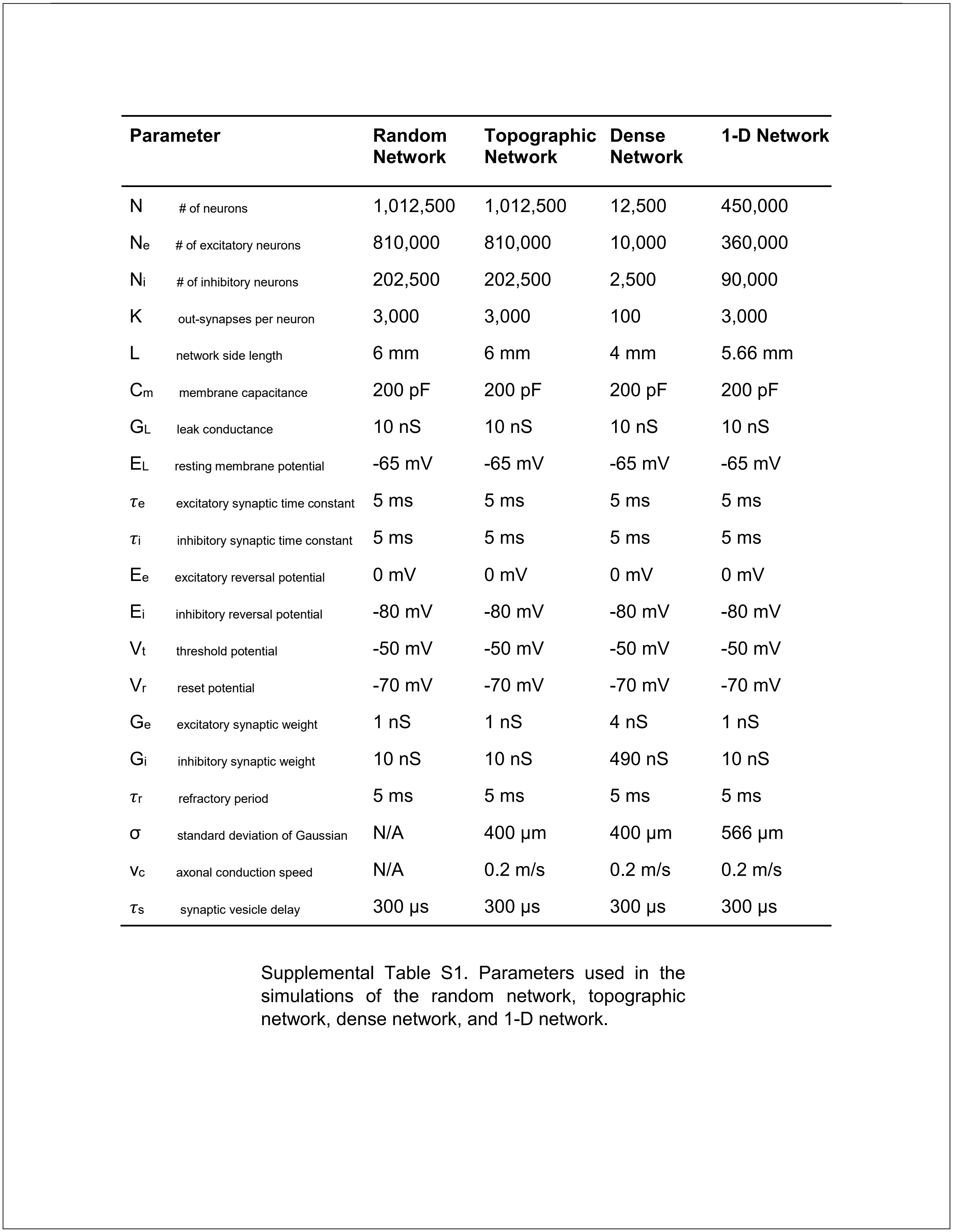

Parameter		**Random Network**	**Topographic Network**	**Dense Network**	**1-D Network**
N	# of neurons	1,012,500	1,012,500	12,500	450,000
N_e	# of excitatory neurons	810,000	810,000	10,000	360,000
N_i	# of inhibitory neurons	202,500	202,500	2,500	90,000
K	out-synapses per neuron	3,000	3,000	100	3,000
L	network side length	6 mm	6 mm	4 mm	5.66 mm
C_m	membrane capacitance	200 pF	200 pF	200 pF	200 pF
G_L	leak conductance	10 nS	10 nS	10 nS	10 nS
E_L	resting membrane potential	-65 mV	-65 mV	-65 mV	-65 mV
τ_e	excitatory synaptic time constant	5 ms	5 ms	5 ms	5 ms
τ_i	inhibitory synaptic time constant	5 ms	5 ms	5 ms	5 ms
E_e	excitatory reversal potential	0 mV	0 mV	0 mV	0 mV
E_i	inhibitory reversal potential	-80 mV	-80 mV	-80 mV	-80 mV
V_t	threshold potential	-50 mV	-50 mV	-50 mV	-50 mV
V_r	reset potential	-70 mV	-70 mV	-70 mV	-70 mV
G_e	excitatory synaptic weight	1 nS	1 nS	4 nS	1 nS
G_i	inhibitory synaptic weight	10 nS	10 nS	490 nS	10 nS
τ_r	refractory period	5 ms	5 ms	5 ms	5 ms
σ	standard deviation of Gaussian	N/A	400 μm	400 μm	566 μm
v_c	axonal conduction speed	N/A	0.2 m/s	0.2 m/s	0.2 m/s
τ_s	synaptic vesicle delay	300 μs	300 μs	300 μs	300 μs

Supplemental Table S1. Parameters used in the simulations of the random network, topographic network, dense network, and 1-D network.

Parameter	**0.5 mm network**	**1 mm network**	**2 mm network**	**3 mm network**	**4 mm network**
N # of neurons	8,000	28,125	112,500	253,125	450,000
K out-synapses per neuron	100	375	1500	3,000	3,000
G_e excitatory synaptic weight	0.1-5 nS	0.1-5 nS	0.1-5 nS	0.1-5 nS	0.1-5 nS
G_i inhibitory synaptic weight	1-50 nS	1-50 nS	1-50 nS	1-50 nS	1-50 nS
L network side length	0.533 mm	1 mm	2 mm	3 mm	4 mm

Supplemental Table S2. Parameters used in scans across 2-D network sizes. N scales with L to maintain a constant neuronal density. K scales with N until the point L exceeds the area of the Gaussian that determines the probability of neuronal connections. The corresponding values of all parameters not listed here are found in Table S1 under the topographic network.

3 | Analytical prediction of spatiotemporal patterns in oscillator networks with distance-dependent time delays

In the previous chapter, a comprehensive numerical study showed that distance-dependent time delays are important in generating biologically realistic spontaneous traveling waves in spiking neural networks. Following that result, we asked what analytical traction could be gained in a more abstract network, nonetheless possessing distance-dependent time delays. It is notoriously difficult to gain analytical insight in such systems, but in this work, we utilized a recent complex-valued approach to the Kuramoto model (Muller et al., 2021; Budzinski et al., 2022) that enabled us to do so. We used a time-delay operator that gave rise to traveling waves in the network. This delay operator and the adjacency matrix, representing network connectivity, collectively influence the eigenmodes of the system. These eigenmodes characterize the dynamics and therefore give analytical insight into how distance-dependent delays can shape spatiotemporal dynamics into traveling waves.

PHYSICAL REVIEW RESEARCH **5**, 013159 (2023)

Analytical prediction of specific spatiotemporal patterns in nonlinear oscillator networks with distance-dependent time delays

Roberto C. Budzinski,[1,2,3,*] Tung T. Nguyen,[1,2,3,*] Gabriel B. Benigno,[1,2,3,*] Jacqueline Đoàn,[1,2,3] Ján Mináč,[1,3]
Terrence J. Sejnowski,[4,5] and Lyle E. Muller[1,2,3,†]
[1]*Department of Mathematics, Western University, London, Ontario N6A 3K7, Canada*
[2]*Brain and Mind Institute, Western University, London, Ontario N6A 3K7, Canada*
[3]*Western Academy for Advanced Research, Western University, Ontario N6A 3K7, Canada*
[4]*The Salk Institute for Biological Studies, La Jolla, California 92037, USA*
[5]*Division of Biological Sciences, University of California, San Diego, La Jolla, California 92161, USA*

(Received 11 March 2022; revised 22 July 2022; accepted 3 January 2023; published 2 March 2023)

We introduce an analytical approach that allows predictions and mechanistic insights into the dynamics of nonlinear oscillator networks with heterogeneous time delays. We demonstrate that time delays shape the spectrum of a matrix associated with the system, leading to the emergence of waves with a preferred direction. We then create analytical predictions for the specific spatiotemporal patterns observed in individual simulations of time-delayed Kuramoto networks. This approach generalizes to systems with heterogeneous time delays at finite scales, which permits the study of spatiotemporal dynamics in a broad range of applications.

DOI: 10.1103/PhysRevResearch.5.013159

I. INTRODUCTION

What is the effect of heterogeneous time delays in networked systems? This question is difficult to treat analytically in the context of multiple distributed time delays. In recent work [1], we studied intracranial electrophysiological recordings from human clinical patients during sleep. We found that the 11–15-Hz sleep "spindle" oscillation, a brain rhythm important for learning and memory [2], was not perfectly synchronized with zero phase difference across the cortex; rather, sleep spindles are organized into rotating waves that travel in a preferred direction (see Movie 1 in Ref. [1]). Importantly, the propagation speed of the observed waves is consistent with the axonal conduction speed of the long-range fiber network in the cortex (3–5 m/s [3]). This set of observations raises an important question: How do these fibers, with no major anisotropy, create a specific spatiotemporal structure with a preferred chirality?

In this paper, we analyze a time-delay Kuramoto model to address this question. Utilizing a recently reported analytical approach to the Kuramoto dynamics [4], we introduce a complex-valued delay operator. This operator shapes the dynamics of the Kuramoto system into waves traveling across the network. The combination of this delay operator and the adjacency matrix determines these dynamics through their effect on eigenvalues in the complex plane, thus providing mechanistic insights into the effect of heterogeneous time delays. The approach introduced here offers a mathematical description for the dynamics of time-delayed networks, an important open problem in physics [5] with many applications in neuroscience [6], engineering [7], and technology [8]. In general, approaches to systems with heterogeneous time delays center on numerical simulations, and no coherent analytical approach currently exists [9,10]. Importantly, while this question first arose from observations of neural dynamics in the human cortex during sleep, the delay operator we introduce here is general to studying the effect of distributed time delays in networks at finite scales, potentially allowing insight into these dynamics in a broad range of systems [11–13].

II. DELAY OPERATOR

We start with the standard Kuramoto model (KM) [14–16] and then consider the model with distance-dependent time delays [17–19]. The original KM on a general network of N nodes is defined by

$$\dot{\theta}_i(t) = \omega_i + \epsilon \sum_{j=1}^{N} A_{ij} \sin(\theta_j(t) - \theta_i(t)), \qquad (1)$$

where $\theta_i \in [-\pi, \pi)$ represents the state variable (phase) of oscillator i at time t, ω_i is the intrinsic angular frequency, ϵ scales the coupling strength, and $A_{ij} \in \{0, 1\}$ represents the elements of the adjacency matrix. The coupling of two connected oscillators i and j causes their phases to attract [15,16,20,21].

Time delays have been observed to be an important mechanism underlying the generation of traveling waves in the brain [13,22–24]. With this in mind, we consider a time-delay

---

[*] These authors contributed equally to this work.
[†] lmuller2@uwo.ca

Published by the American Physical Society under the terms of the Creative Commons Attribution 4.0 International license. Further distribution of this work must maintain attribution to the author(s) and the published article's title, journal citation, and DOI.

Kuramoto model (dKM) with delays τ_{ij} that depend on the distance between two oscillators i and j:

$$\dot{\theta}_i(t) = \omega_i + \epsilon \sum_{j=1}^{N} A_{ij} \sin(\theta_j(t - \tau_{ij}) - \theta_i(t)). \tag{2}$$

The delay operator approach we introduce here generalizes to arbitrary adjacency matrices. In order to demonstrate this approach, we start by considering an undirected ring graph $\mathfrak{G}_{\mathrm{RG}}$, where $N = 100$ nodes are arranged on a one-dimensional ring with periodic boundary conditions. Each node in $\mathfrak{G}_{\mathrm{RG}}$ is connected to the $k = 25$ nearest neighbors in each direction, and $A_{ij} \in \{0, 1\}$ is 1 if oscillators i and j are connected, and 0 otherwise. The time delay $\tau_{ij} = d_{ij}/\nu$ between two nodes i and j grows linearly with distance (d_{ij}) with respect to the periodic boundary conditions on the ring [$d_{ij} = \min(|i - j|, N - |i - j|)$]. For the parameters chosen in this paper, the time delays range from approximately 2 to 62 ms, a timescale relevant to neural dynamics [10,25,26]. We consider the case where all oscillators have the same frequency of 10 Hz ($\omega = 20\pi$); however, our approach can be applied to the case of nonidentical natural frequencies [27].

The time-delay term $\theta_j(t - \tau_{ij})$ can be approximated by $\theta_j(t) - \omega\tau_{ij}$ [17,18,24]. Using this approximation, in combination with the algebraic approach to the Kuramoto dynamics [4,28], we introduce a delay operator, which provides analytical insight into how heterogeneous time delays can create specific, sophisticated spatiotemporal structures in the resulting nonlinear dynamics. Applying this approximation to Eq. (2), we arrive at an equation that captures the time-delay dynamics in the dKM in heterogeneous phase lags [17,18,24]. We can then use our algebraic approach to the Kuramoto dynamics and arrive at (see Appendix A for details)

$$\boldsymbol{x}(t) = e^{i\omega t} e^{t\boldsymbol{W}} \boldsymbol{x}(0), \tag{3}$$

where $\boldsymbol{x} \in \mathbb{C}^N$ and the matrix $\boldsymbol{W}$ is given by

$$\boldsymbol{W} = \epsilon e^{-i\boldsymbol{\eta}} \circ \boldsymbol{A}, \tag{4}$$

where $\circ$ represents the Hadamard (elementwise) product. This matrix has information about the coupling strength ϵ, the time delays $\boldsymbol{\eta} = \omega\boldsymbol{\tau}$ present in the original dKM, and the connection scheme of the system on $\boldsymbol{A}$. In previous work, we have shown that this complex-valued equation, when evaluated through the procedure described below, precisely captures the trajectories of the original, nonlinear Kuramoto model [28]. We now show that this approach generalizes to the case of heterogeneous time delays.

With this approach, we have two dynamical systems: the original, nonlinear KM and a complex-valued system with the explicit solution in Eq. (3) (details on the derivation can be found in Ref. [28] and in Appendix A). In the complex-valued system, $\boldsymbol{x} \in \mathbb{C}^N$ has elements $x_i(t) \in \mathbb{C}$ whose argument we compare with the numerical solution of the original Kuramoto model with heterogeneous time delays (dKM) $\theta_i(t) \in \mathbb{R}$ [obtained by Euler integration of Eq. (2) with high temporal precision]. That is, $\mathrm{Arg}[x_i(t)]$ is compared with $\theta_i(t)$. When initialized with unit-modulus initial conditions $|x_i(0)| = 1$ for all i, with arguments $\mathrm{Arg}[x_i(0)]$ that match the initial phases $\theta_i(0)$ in the original dKM, the trajectories in the original and complex-valued KM correspond for a nontrivial window of time [4]. As mentioned above, in Ref. [28] we found that iterating the explicit expression (3) in a specific manner produces trajectories in the complex-valued system that *precisely* match those in the original, nonlinear Kuramoto model. Specifically, we can evaluate

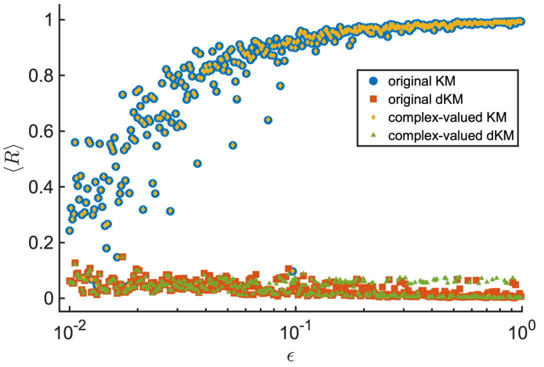

FIG. 1. Synchronization level for nondelayed and delayed networks. The time-average Kuramoto order parameter $\langle R \rangle$ is plotted as a function of the coupling strength ϵ for the nondelayed case (blue circles, original KM; orange diamonds, complex-valued KM) and for the delayed case (red squares, original dKM; green triangles, complex-valued dKM). Each point represents one 10-s simulation with random initial conditions [$\mathcal{U}(-\pi, \pi)$], which are the same for the complex-valued case and for the numerical simulation at each point.

$$\boldsymbol{x}(t + \varsigma) = \Lambda[e^{i\omega\varsigma} e^{\varsigma\boldsymbol{W}} \boldsymbol{x}(t)], \tag{5}$$

where ς is small but finite, $t \in [0, \varsigma, 2\varsigma, \ldots, n\varsigma]$, and Λ represents an elementwise operator mapping the modulus of each state vector element $x_i(t)$ to unity. This approach represents an iterative analytical procedure, defined by the application of the linear matrix exponential and Λ. Note that Eq. (5) propagates the solution at discrete time intervals defined by ς, Eq. (3) can be applied within intervals defined by ς, and $\varsigma > dt$. Critically, while this iterative procedure does not represent a closed-form, all-time solution for the dynamics of the original nonlinear Kuramoto system, all evolution of the arguments $\mathrm{Arg}[x_i]$ [which, again, correspond with $\theta_i(t)\ \forall\ i$ in the original KM] is governed under the linear matrix exponential operator, and it is clear that the elementwise Λ operator only changes the moduli. In this paper, we show that this approach applies also in the case of heterogeneous time delays and provides analytical insight into how distance-dependent time delays create specific spatiotemporal patterns.

III. RESULTS

We first study phase synchronization in networks with (dKM) and without (KM) time delays on $\mathfrak{G}_{\mathrm{RG}}$, as a function of the coupling strength ϵ (Fig. 1). We use the Kuramoto order parameter,

$$R(t) = \frac{1}{N} \left| \sum_{j=1}^{N} e^{i\theta_j(t)} \right|, \tag{6}$$

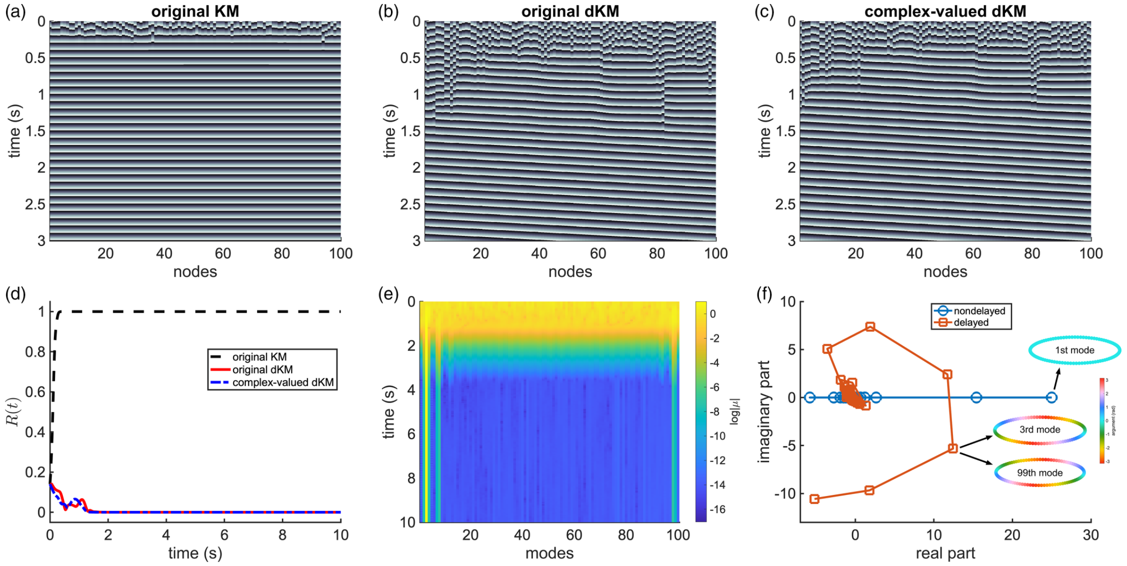

FIG. 2. Analytical and geometric view of the effect of time delays. The spatiotemporal dynamics of the system is represented using color coding, where the phase of each oscillator is plotted as a function of time for (a) the original KM, (b) the original dKM, (c) and the complex-valued dKM. Dark colors represent phases close to $-\pi$, and light colors represent phases close to π. (a) Without delay, the network transitions to phase synchronization, which is represented by the horizontal lines. The effect of the delay, however, induces wave patterns in the system, whose dynamics are represented (b) in the original dKM and also captured (c) by the complex-valued model. (d) These dynamical characteristics are corroborated by the Kuramoto order parameter $R(t)$. (e) The eigenmodes offer a geometric perspective to such dynamics, where the waves are represented by a single eigenmode contribution (third mode in this case). (f) The eigenvalues of $\boldsymbol{W}$ (delayed) and $\epsilon\boldsymbol{A}$ (nondelayed) provide further analytical insights into the effect of the delay in the system: It rotates the eigenvalues in the complex plane, which allows the system to access different modes. In the nondelayed case, the leading eigenvalue (in the real part) is associated with an eigenvector with a zero-phase-difference configuration (first mode). In the delayed case, otherwise, there are two leading eigenvalues that are associated with the eigenvectors $\boldsymbol{v}_3$ and $\boldsymbol{v}_{99}$, which have phase configurations representing traveling waves.

and its time average $\langle R\rangle$ for 10-s simulations to measure the level of phase synchronization. As the coupling strength ϵ increases in the nondelayed case (original KM and complex-valued KM), $\langle R\rangle$ begins at a low value and increases until approaching unity (representing phase synchronization).

In the case with heterogeneous time delay (original dKM and complex-valued dKM), the order parameter remains low (Fig. 1, red squares and green triangles), reflecting the fact that time delays induce a range of spatiotemporal patterns, as observed previously [17,18,29–33]. Here, we observe that the complex-valued model is able to capture the average dynamics that the original Kuramoto model depicts, for both the nondelayed and delayed cases, for different coupling strengths across different initial conditions (Fig. 1).

We next study dynamics in the KM and dKM considering an individual realization, for a fixed coupling strength ($\epsilon = 0.5$), and compare the dynamics of the original dKM with the evaluation of the complex-valued approach. Without time delays, the original KM exhibits a quick transition from random initial conditions to a phase-synchronized state [horizontal lines, Fig. 2(a)]. With time delays, however, phase synchronization is not reached, and the original dKM exhibits a transition from random initial conditions to a traveling wave state [diagonal structures, Fig. 2(b)]. The evaluation of the complex-valued dKM captures both the transient dynamics and the traveling wave state exhibited in the original dKM [Fig. 2(c)], as well as the dynamics of the Kuramoto order parameter $R(t)$ [Fig. 2(d)].

Our approach to systems with heterogeneous time delay provides insight into the mechanism for these dynamics in terms of the spectrum of $\boldsymbol{W}$—Eq. (4). If $\boldsymbol{A}$ and $\boldsymbol{\tau}$ are circulant, $\boldsymbol{W}$ is also circulant (see Appendix B); hence $\boldsymbol{W}$ and $\boldsymbol{A}$ share the same eigenvectors (which form an orthonormal basis). We can then write Eq. (3) using the eigenspectrum of $\boldsymbol{W}$, which results in $\boldsymbol{x}(t) = e^{i\omega t}(\alpha_1 e^{\lambda_1 t}\boldsymbol{v}_1 + \cdots + \alpha_N e^{\lambda_N t}\boldsymbol{v}_N)$, where α_i can be written in terms of initial conditions. Importantly, we can also write Eq. (5) in a similar fashion, which results in $\boldsymbol{x}(t+\varsigma) = \Lambda[e^{i\omega\varsigma}(\alpha_1 e^{\lambda_1\varsigma}\boldsymbol{v}_1 + \cdots + \alpha_N e^{\lambda_N\varsigma}\boldsymbol{v}_N)]$, where α_i can again be written in terms of the state of the system at time $t \in [0, \varsigma, 2\varsigma, \ldots, n\varsigma]$. Thus, while it is in general a very difficult problem to understand the dynamics of nonlinear networks in terms of eigenspectra, this approach provides a unique insight into the connection between the spectrum of $\boldsymbol{W}$—Eq. (4)—and the spatiotemporal dynamics of the nonlinear oscillator network—Eq. (2). Critically, our approach uses familiar mathematical techniques from linear algebra matrix theory in a distinct way: While previous approaches in nonlinear dynamics have sought to describe the dynamics using the spectrum of the Laplacian matrix [34–36], the focus on the complex-valued system in our approach enables the insight that the *argument* of the eigenvectors of the matrix $\boldsymbol{W}$

provides analytical predictions about the resulting nonlinear dynamics.

Following this idea, Fig. 2(e) shows the eigenmode contributions, here represented by $\log|\mu_i|$, as a function of time, for the dynamics in Fig. 2(c). Here, the eigenmode contributions are given by the projection of the complex-valued approach solution $\boldsymbol{x}(t)$ onto the eigenvectors of $\boldsymbol{W}$. The eigenmode contributions are obtained as $\mu_k(t) = \langle \boldsymbol{x}(t), \boldsymbol{v}_k \rangle$, where $\langle \cdot \rangle$ denotes the standard complex inner product. Figure 2(e) shows that, when the network exhibits incoherent dynamics, the eigenmode contributions remain uniform across μ_i. When the traveling wave pattern is reached, on the other hand, the third eigenmode becomes dominant (note the log scale). These results demonstrate that the change from incoherent dynamics to a traveling wave can be understood quite directly through the geometry of the eigenmodes. Furthermore, in the case of circulant networks, we can evaluate eigenvalues and eigenvectors analytically using the circulant diagonalization theorem (CDT) [37]; in this case, the first eigenvector represents the solution where all oscillators have the same phase (phase synchronization), and higher modes represent wave patterns, given by Fourier modes (see Appendix C).

The effect of heterogeneous time delays on the dynamics of the dKM can be understood through the geometry of eigenvalues in the complex plane. Figure 2(f) illustrates the eigenvalues of $\epsilon\boldsymbol{A}$ (nondelayed) and $\boldsymbol{W}$ (delayed). While the nondelayed case (blue line and circles) has purely real eigenvalues, the effect of the heterogeneous time delays (red line and squares) can be understood in our framework in terms of the Hadamard (elementwise) product of the delay operator $\boldsymbol{\tau}$ and $\boldsymbol{A}$ [see Eq. (4) and Appendix B]. The effect of this operation is to provide a specific rotation of the eigenvalues in the complex plane. This rotation allows the system to access higher modes and, therefore, to exhibit different traveling wave patterns. Furthermore, the rotation is not the same for all eigenvalues because the delays are heterogeneous. In this particular case, the rotation leads to eigenvalues associated with the 3rd and 99th modes to have the largest real part, allowing the system to reach traveling wave states associated with the 3rd and 99th modes. In the particular example of Fig. 2, the network evolves to a wave given by the third mode, but different (random) initial conditions can evolve to the dynamics described by either the 3rd or 99th mode [27]. Moreover, when different time delays are considered, different modes can be dominant, and therefore the system evolves to a different wave pattern [27].

We can now uncover how the combination of network structure, time delays, and node state can create specific spatiotemporal patterns. By using our delay operator approach, we can analytically predict the specific pattern to which the original dKM evolves. Figure 3(a) shows the wave pattern given by θ obtained from the original dKM (blue line) and the argument (elementwise) of the third eigenvector (red line), which predicts the observed dynamics [27]. In this case, phases increase in the clockwise direction around the ring, which we define to be the positive direction (+1). It is important to note that, in our approach, the argument of each eigenvector element ($\mathrm{Arg}[(\boldsymbol{v}_k)_i]\,\forall i \in [1, N]$) directly relates with the phase offset in the resulting network dynamics. Because of the correspondence between trajectories in the complex-valued model and the original dKM, this approach creates a direct link between eigenvectors of the adjacency matrix and the specific spatiotemporal dynamics that result. For the dynamics in Fig. 3(a), the eigenmode contribution is given by μ_3 [see Fig. 2(e)], and the phase configuration matches the argument of $\boldsymbol{v}_3$. In the example considered here, two eigenvalues are dominant (i.e., having the largest real part): λ_3 and λ_{99} [Fig. 2(f)]. Different initial conditions can thus evolve to the phase pattern given by the 99th mode, which is predicted by $\boldsymbol{v}_{99}$ [Fig. 3(b)]. In this case, the spatial frequency is the same as observed in the previous case, but the direction of the wave pattern is the opposite [27]. These results show a clear connection between the spectrum of the network (described by $\boldsymbol{W}$) and the dynamics on the original dKM, where the wave pattern (solution) can be described by the phase configuration of the eigenvector associated with the dominant mode.

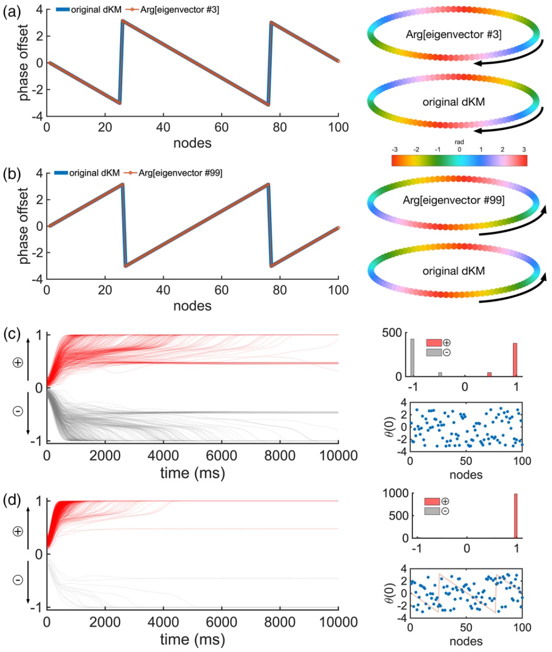

FIG. 3. Analytical predictions of specific wave patterns. (a) The phase configuration for the original dKM (blue line) matches the argument (elementwise) of the third eigenvector $\mathrm{Arg}[\boldsymbol{v}_3]$—the analytical prediction (red dotted line). A representation on the circle using color coding reveals the wave pattern (right). (b) Different initial conditions lead to the wave pattern that matches the argument of the 99th eigenvector $\mathrm{Arg}[\boldsymbol{v}_{99}]$. These waves can propagate either counterclockwise (negative) or clockwise (positive). (c) With random initial conditions, due to the dominance of two eigenvalues (3rd and 99th), the system exhibits waves propagating in both directions—with approximately half of the initial conditions evolving to each direction (top right). (d) With biased initial conditions, starting from $\mathrm{Arg}[\boldsymbol{v}_3]$ (red line, bottom right) and adding uniform random phases $0.8(\mathcal{U}(-\pi, \pi))$, we obtain a preferred direction of propagation.

We take counterclockwise increases in phase to be in the negative direction, and clockwise increases to be positive.

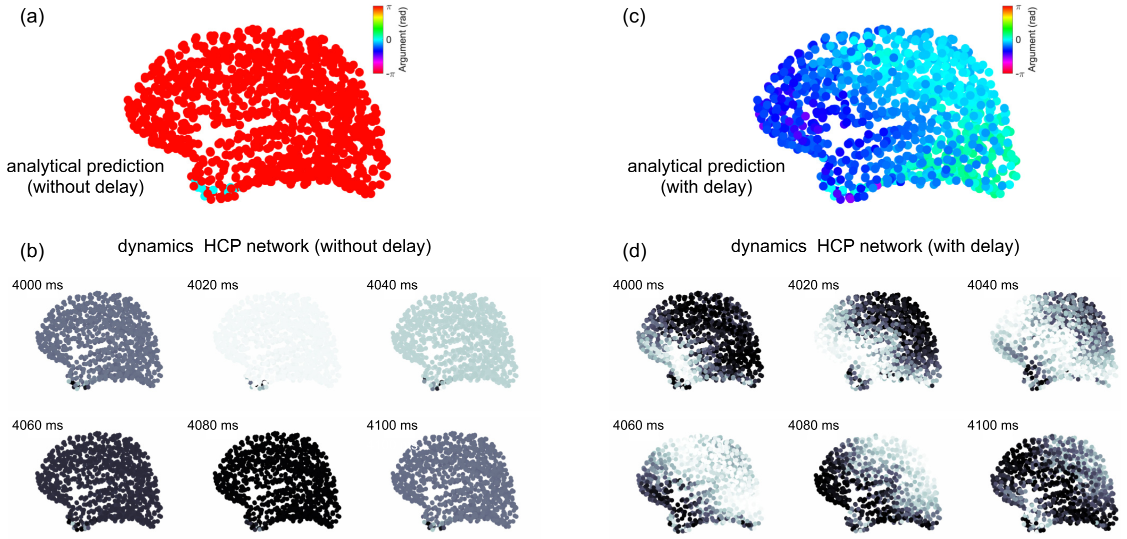

FIG. 4. Analytical predictions of spatiotemporal patterns in brain networks. We use our approach to investigate networks based on the Human Connectome Project (HCP) [38]. We consider the case without delay in the coupling between nodes and also the case with distance-dependent delays (heterogeneous delay). We use our delay operator to create the matrix $\boldsymbol{W}$, which allows analytical predictions of the dynamics. We show the phase of each node, given by the Kuramoto model, using color coding (dark colors are values close to $-\pi$, and light colors are values close to π). (a) In the case without delay, the argument of the leading eigenvector depicts zero phase difference, which predicts phase synchronization. (b) We then study the numerical simulation for the network without delay, given by Eq. (1), which shows a phase-synchronized state. (c) In the case with heterogeneous time delays, the argument of the leading eigenvector shows a phase offset from the bottom left to the top right (in the projection), which predicts a wave pattern. (d) We perform the numerical simulation with the delayed Kuramoto model, given by Eq. (2), and the network depicts the wave pattern that is predicted by our approach. This shows that we are able to predict the dynamics observed in the simulations using our delay operator.

Because the network considered here has two dominant eigenvalues equal in their real parts, random initial conditions evolve equally either to the phase pattern of $\boldsymbol{v}_3$ or to the phase pattern of $\boldsymbol{v}_{99}$ in individual simulations [Fig. 3(c)]. To quantify the spatiotemporal dynamics, the spatial frequency, and the direction of propagation, we compare the phases obtained from the original dKM and the argument of the eigenvectors of $\boldsymbol{W}$. Specifically, we evaluate

$$\rho^{(k)}(t) = \left|\frac{1}{N}\sum_{j=1}^{N} e^{i\theta_j(t)} e^{-i\mathrm{Arg}[(\boldsymbol{v}_k)_j]}\right|, \tag{7}$$

where $\theta_j(t)$ is the phase of the oscillator j at time t obtained from the original dKM, N is the number of oscillators in the network, i is the imaginary unit, and $\boldsymbol{v}_k$ is the kth eigenvector of $\boldsymbol{W}$. Here, we use $\boldsymbol{v}_3$, and $\rho^{(k)} = 1$ means that the phase configuration of the network given by the $\boldsymbol{\theta}(t)$ is the same as the one given by the argument of the eigenvector $\boldsymbol{v}_k$. In the case shown in Fig. 3(c), approximately half of the simulations evolve to the positive direction, indicating that the dynamics matches the argument of $\boldsymbol{v}_3$, and approximately half evolve to the negative, indicating that the dynamics is given by the argument of $\boldsymbol{v}_{99}$. A small fraction of initial conditions exhibit inner products of approximately ±0.5, corresponding to a wave with a different spatial frequency.

Using the insights from this approach, we can now design initial conditions that generate waves in a preferred direction. To do this, we started from the phase pattern specified by $\boldsymbol{v}_3$ and randomized the phases by nearly a full cycle ($0.8\,\mathcal{U}[-\pi,\pi]$, then wrapped in $[-\pi,\pi]$). While this initial condition is nearly random (Fig. 3(d), bottom right, where the red line represents $\mathrm{Arg}[\boldsymbol{v}_3]$; compare with Fig. 3(c), bottom right), nearly all simulations evolve to the positive direction. These results demonstrate that the combination of connectivity, time delays, and network state can generate specific spatiotemporal patterns in oscillator networks—here, traveling waves with a chirality in a preferred direction.

The framework for systems with heterogeneous time delays introduced in this paper generalizes to many types of networks. This approach can be applied to very sophisticated networks obtained from experimental data. In particular, this approach can successfully predict traveling wave patterns arising in an oscillator network based on connectivity in the human brain. Figure 4 illustrates simulations and the analytical prediction resulting from our approach for networks where the connectivity data are based on the Human Connectome Project (HCP) [38]. In this case, $N = 998$ cortical regions are given at a point in 3-space, with connections between areas derived from neuroimaging data. Connection weights between regions are determined by the number of fibers [38,39], which we use to build the adjacency matrix $\boldsymbol{A}$. Here, the coupling strength is scaled with $\epsilon = 200$, and the initial conditions for each analysis are given by random phases $[-\pi,\pi]$. Furthermore, time delays are obtained by

$\tau_{ij} = d_{ij}/\nu$, where the distances d_{ij} are determined by the average length of these fibers and the known axonal conduction speed is given by $\nu = 5$ m/s [40]. The dynamics of each node is represented by the Kuramoto model, given either by Eq. (1) in the nondelayed case or by Eq. (2) in the delayed case. The natural frequency of each oscillator is given by 10 Hz (simulating, for example, a specific drive from the thalamus). Using the delay operator, we construct the matrix $\boldsymbol{W}$ for these systems—Eq. (4)—which allows us to obtain analytical predictions of the spatiotemporal patterns that emerge. First, we consider the case without time delays, where $\tau_{ij} = 0$. We then obtain the eigenspectrum of the matrix $\boldsymbol{W}$ and plot the argument (elementwise) of the eigenvector associated with the leading eigenvalue [Fig. 4(a)]. In this case, this eigenvector shows a zero phase difference across nodes, predicting phase synchronization. We then perform the numerical simulation of the Kuramoto model (without delay), given by Eq. (1), and plot the phase of each node using color coding [Fig. 4(b)], where we observe a phase-synchronized behavior [27]. On the other hand, when we consider time delays in the interaction between cortical areas, the scenario is different. In this case, the argument (elementwise) of the eigenvector associated with the leading eigenvalue depicts a phase offset increasing from the bottom left to the top right (in this projection), predicting a wave propagating along that direction [Fig. 4(c)]. We then perform numerical simulations of the Kuramoto model with heterogeneous time delays—Eq. (2)—and we observe the wave pattern that is predicted by our approach, as shown in Fig. 4(d) [27]. This example now clearly demonstrates the advantage of this analytical approach: When we numerically evaluate the eigenspectrum of $\boldsymbol{W}$ in this case, the leading eigenvector for the case without delays predicts phase synchrony, while the leading eigenvector for the case with delays predicts the *precise* wave pattern observed in the simulation. This result shows that our approach is able to predict the spatiotemporal pattern that results from connectivity and time delays in a highly relevant, real-world case.

IV. CONCLUSION

In this paper, we have introduced an analytical approach to the dynamics of nonlinear oscillator networks with heterogeneous time delays, an important open problem in physics with many potential applications. The advance in this paper is based on an algebraic approach to the Kuramoto model introduced in Ref. [28]. Importantly, the flexibility of this framework allowed us to introduce a delay operator, which provides rigorous analytical predictions for the specific traveling wave patterns induced by distance-dependent time delays. Using this approach, we can explain the effect of time delays in terms of a rotation of the eigenvalues of the matrix describing the system, which provides a clear and precise way to understand heterogeneous time delays in terms of the geometry of eigenmodes. Our approach therefore allows analytical predictions for the specific spatiotemporal patterns exhibited by the original dKM.

This framework allows us to understand how the combination of isotropic connectivity and time delays can produce traveling waves propagating in a preferred direction, as observed in experimental data [1]. Importantly, while this question first arose in our study of neural dynamics in human cortex during sleep, the approach we have introduced here is general to networks of oscillators at finite scales. The results shown in this paper, together with the results in Refs. [4,28], represent a coherent and general framework for nonlinear oscillator networks.

al advance of this framework is to consider the dynamics in an individual simulation, taking into account both the initial conditions and the specific connectivity pattern in the network. This framework thus provides an opportunity to connect an individual adjacency matrix, for example, a single network taken from experimental data or a single realization of a random graph model, to the specific spatiotemporal pattern that results in a simulation. This approach has important potential applications, for example, in linking an experimentally reconstructed brain network to dynamics and computation in a neural system [41] or in linking the connections in a large-scale power grid to potential large and transient disruptions [42,43]. In this paper, we have generalized this framework to systems with heterogeneous time delays, which demonstrates the utility of this algebraic, operator-based approach to nonlinear dynamical systems at finite scales.

An open-source code repository for this work is available on GitHub [44].

ACKNOWLEDGMENTS

This work was supported by BrainsCAN at Western University through the Canada First Research Excellence Fund (CFREF), the NSF through a NeuroNex award (Award No. 2015276), Natural Sciences and Engineering Research Council of Canada (NSERC) Grant No. R0370A01, ONR Grant No. N00014-16-1-2829, NIH Grants No. EB009282 and No. EB026899, the Swartz Foundation, SPIRITS 2020 of Kyoto University, Compute Ontario [45], Digital Research Alliance of Canada [46], and the Western Academy for Advanced Research. J.M. gratefully acknowledges support from a Western University Faculty of Science Distinguished Professorship in 2020–2021. R.C.B. gratefully acknowledges support from a Western Institute for Neuroscience Clinical Research Postdoctoral Fellowship. G.B.B. gratefully acknowledges support from the Canadian Open Neuroscience Platform (in the form of a Graduate Scholarship), the Vector Institute (as a Postgraduate Affiliate), and NSERC (in the form of a Canada Graduate Scholarship - Doctoral).

APPENDIX A: THE COMPLEX-VALUED APPROACH

We consider the Kuramoto model with heterogeneous time delays described by Eq. (2) and then use the approximation given by $\theta_j(t-\tau_{ij}) \approx \theta_j(t) - \omega\tau_{ij}$ [17,18,24], which leads to

$$\dot{\theta}_i(t) = \omega + \epsilon \sum_{j=1}^{N} A_{ij} \sin(\theta_j(t) - \theta_i(t) - \eta_{ij}), \tag{A1}$$

where $\eta_{ij} = \omega\tau_{ij}$.

Based on Refs. [4,28], we introduce the complex-valued approach to the Kuramoto model described by Eq. (A1). To do that, we introduce a new dynamical system, described by the variable $\psi \in \mathbb{C}$:

$$\dot{\psi}_i(t) = \omega + \epsilon \sum_{j=1}^{N} A_{ij}[\sin(\psi_j(t) - \psi_i(t) - \eta_{ij}) - i\cos(\psi_j(t) - \psi_i(t) - \eta_{ij})]. \tag{A2}$$

Next, multiplying both sides by i and applying Euler's formula yields

$$i\dot{\psi}_i(t) = i\omega + \epsilon e^{-i\psi_i(t)} \sum_{j=1}^{N} A_{ij} e^{i\psi_j(t)} e^{-i\eta_{ij}}. \tag{A3}$$

We define $\boldsymbol{W}$ as

$$\boldsymbol{W} = \epsilon e^{-i\boldsymbol{\eta}} \circ \boldsymbol{A}, \tag{A4}$$

where $\circ$ represents the Hadamard product (or elementwise product) and $\eta_{ij} = \omega\tau_{ij}$. This results in the following matrix form of Eq. (A3):

$$\dot{\boldsymbol{\psi}}(t) = \boldsymbol{\omega} + \frac{1}{i}\,\mathrm{diag}[e^{-i\boldsymbol{\psi}(t)}]\,\boldsymbol{W} e^{i\boldsymbol{\psi}(t)}, \tag{A5}$$

where we note explicitly that $\boldsymbol{\psi} = [\psi_1, \ldots, \psi_N]^T$, $\dot{\boldsymbol{\psi}} = [\dot{\psi}_1, \ldots, \dot{\psi}_N]^T$, and $\boldsymbol{\omega} = [\omega, \ldots, \omega]^T$. Furthermore, we can write the previous equation as

$$\frac{d}{dt} e^{i\boldsymbol{\psi}(t)} = (\mathrm{diag}[i\boldsymbol{\omega}] + \boldsymbol{W}) e^{i\boldsymbol{\psi}(t)}. \tag{A6}$$

Lastly, letting $\boldsymbol{x}(t) = e^{i\boldsymbol{\psi}(t)}$, we have

$$\dot{\boldsymbol{x}}(t) = (\mathrm{diag}[i\boldsymbol{\omega}] + \boldsymbol{W})\boldsymbol{x}(t), \tag{A7}$$

whose general solution is

$$\boldsymbol{x}(t) = e^{i\omega t} e^{t\boldsymbol{W}} \boldsymbol{x}(0). \tag{A8}$$

In this paper, the dynamics of the complex-valued approach is studied by considering the elementwise argument of $\boldsymbol{x}(t)$, i.e., $\mathrm{Arg}[x_i(t)]\ \forall\ i \in [1, N]$. As shown in Ref. [28], when $\frac{|x_j|}{|x_i|} \approx 1$, the dynamics of $\mathrm{Arg}[\boldsymbol{x}(t)]$ precisely matches the trajectories of the Kuramoto model given by Eq. (A1). This allows us to use the eigenspectrum of $\boldsymbol{W}$ to understand and predict the dynamics of the Kuramoto model with heterogeneous time delays.

APPENDIX B: CIRCULANT NETWORKS AND HADAMARD PRODUCT

The definition of the Hadamard product can be described as follows.

Definition 1. Let $\boldsymbol{A}, \boldsymbol{B}$ be two $n \times n$ matrices. The Hadamard product $\boldsymbol{A} \circ \boldsymbol{B}$ is a matrix of dimension $n \times n$ with elements given by

$$(\boldsymbol{A} \circ \boldsymbol{B})_{ij} = (\boldsymbol{A})_{ij}(\boldsymbol{B})_{ij}.$$

For a complex number λ, we also define $e^{\circ(\lambda \boldsymbol{A})}$ to be the matrix of dimension $n \times n$ with elements given by

$$(e^{\circ\lambda\boldsymbol{A}})_{ij} = e^{\lambda \boldsymbol{A}_{ij}}.$$

We have the following observation.

Proposition 1. Let $\boldsymbol{A}, \boldsymbol{B}$ be two circulant matrices. Then (1) $\boldsymbol{A} \circ \boldsymbol{B}$ is a circulant matrix and (2) $e^{\lambda\circ\boldsymbol{A}}$ is a circulant matrix.

Proof. Assume that $\boldsymbol{A} = \mathrm{circ}(\boldsymbol{a})$, $\boldsymbol{B} = \mathrm{circ}(\boldsymbol{b})$ with $\boldsymbol{a} = (a_1, a_2, \ldots, a_n)$ and $\boldsymbol{b} = (b_1, b_2, \ldots, b_n)$. Then we can see that

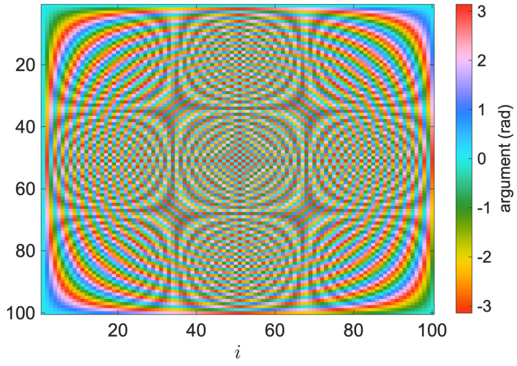

FIG. 5. A graphical representation of the matrix with the phase configuration of the eigenvectors of $\boldsymbol{W}$. The kth column is the color-coded argument (elementwise) of the kth eigenvector.

$$\boldsymbol{A} \circ \boldsymbol{B} = \mathrm{circ}((a_1b_1, a_2b_2, \ldots, a_nb_n))$$

and

$$e^{\circ\lambda\boldsymbol{A}} = \mathrm{circ}((e^{\lambda a_1}, e^{\lambda a_2}, \ldots, e^{\lambda a_n})).$$

Therefore we conclude that both $\boldsymbol{A} \circ \boldsymbol{B}$ and $e^{\lambda\circ\boldsymbol{A}}$ are circulant. ■

APPENDIX C: THE CIRCULANT DIAGONALIZATION THEOREM

In the case of circulant networks, we can use the circulant diagonalization theorem (CDT) to obtain the eigenspectrum of the adjacency matrix analytically [37]. In this paper, both the nondelayed network $\epsilon\boldsymbol{A}$ and the delayed one $\boldsymbol{W}$ are circulant (see Proposition 1). The CDT states that all circulant matrices, say, $\boldsymbol{H} = \mathrm{circ}(\boldsymbol{h})$, where $\mathrm{circ}(\boldsymbol{h})$ is the circulant matrix constructed from the generating vector $\boldsymbol{h} = (h_1, \ldots, h_N)$, are diagonalized by the same unitary matrix $\boldsymbol{U}$ with components

$$U_{ks} = \frac{1}{\sqrt{N}} \exp\left[-\frac{2\pi i}{N}(k-1)(s-1)\right], \tag{C1}$$

where $k, s \in [1, N]$, and that the N eigenvalues are given by

$$E_k(\boldsymbol{H}) = \sum_{j=1}^{N} h_j \exp\left[-\frac{2\pi i}{N}(k-1)(j-1)\right]. \tag{C2}$$

We let Eq. (C2) determine the ordering of the eigenvalues throughout this paper. The argument of the eigenvectors associated with these eigenvalues corresponds to the columns of the discrete Fourier transform (DFT) matrix, which range from low to high spatial frequencies.

Figure 5 shows the argument of the eigenvectors using color coding. Here, $\mathrm{Arg}[(\boldsymbol{v}_1)_i] = 0\ \forall\ i \in [1, N]$ (as shown in Fig. 2), which represents zero phase difference across oscillators, or phase synchronization. The other eigenvectors represent Fourier modes (waves) with different spatial frequencies. Figure 2 shows the cases of the eigenvectors $\boldsymbol{v}_3$ and $\boldsymbol{v}_{99}$.

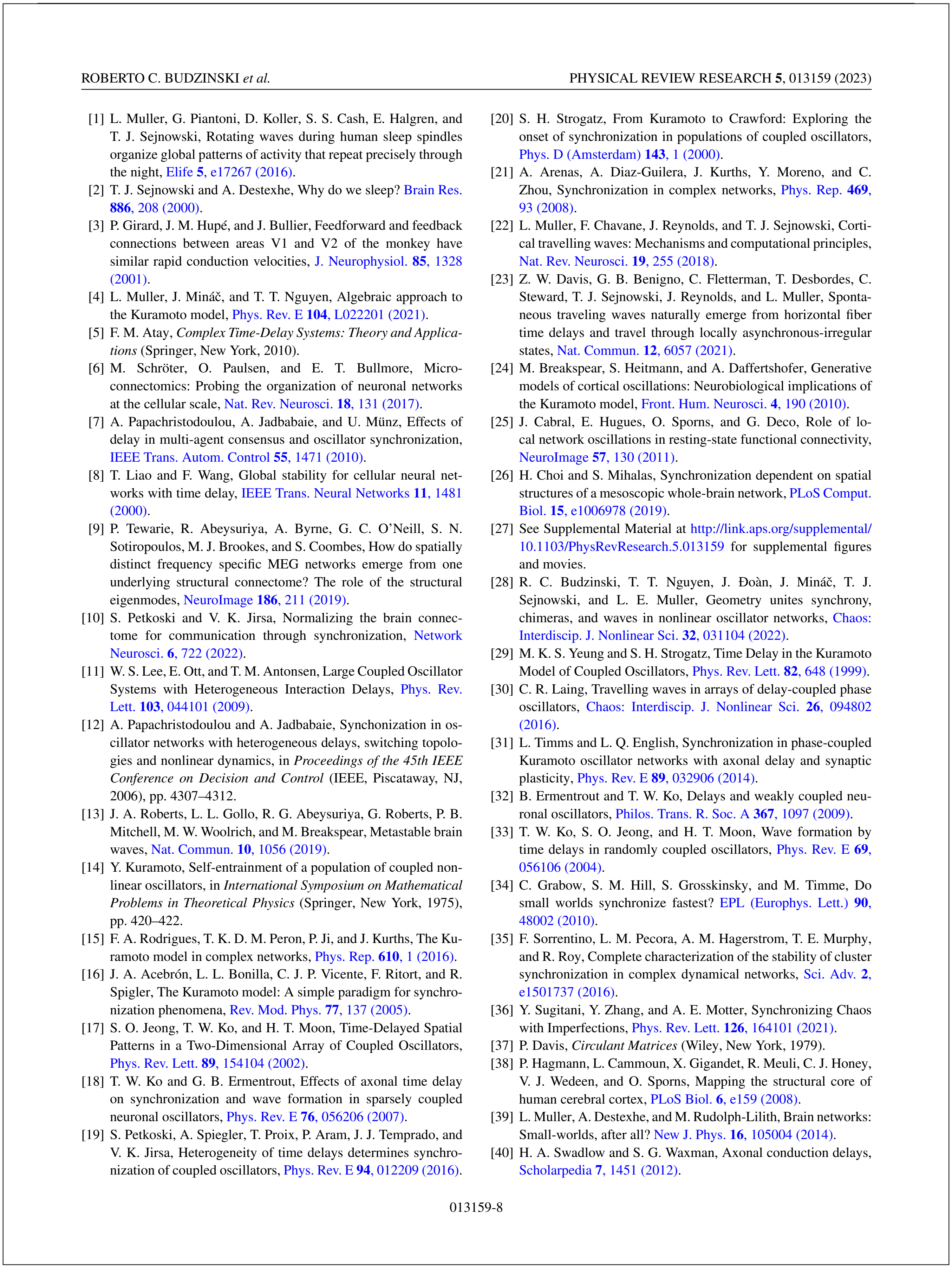

[1] L. Muller, G. Piantoni, D. Koller, S. S. Cash, E. Halgren, and T. J. Sejnowski, Rotating waves during human sleep spindles organize global patterns of activity that repeat precisely through the night, Elife **5**, e17267 (2016).

[2] T. J. Sejnowski and A. Destexhe, Why do we sleep? Brain Res. **886**, 208 (2000).

[3] P. Girard, J. M. Hupé, and J. Bullier, Feedforward and feedback connections between areas V1 and V2 of the monkey have similar rapid conduction velocities, J. Neurophysiol. **85**, 1328 (2001).

[4] L. Muller, J. Mináč, and T. T. Nguyen, Algebraic approach to the Kuramoto model, Phys. Rev. E **104**, L022201 (2021).

[5] F. M. Atay, *Complex Time-Delay Systems: Theory and Applications* (Springer, New York, 2010).

[6] M. Schröter, O. Paulsen, and E. T. Bullmore, Microconnectomics: Probing the organization of neuronal networks at the cellular scale, Nat. Rev. Neurosci. **18**, 131 (2017).

[7] A. Papachristodoulou, A. Jadbabaie, and U. Münz, Effects of delay in multi-agent consensus and oscillator synchronization, IEEE Trans. Autom. Control **55**, 1471 (2010).

[8] T. Liao and F. Wang, Global stability for cellular neural networks with time delay, IEEE Trans. Neural Networks **11**, 1481 (2000).

[9] P. Tewarie, R. Abeysuriya, A. Byrne, G. C. O'Neill, S. N. Sotiropoulos, M. J. Brookes, and S. Coombes, How do spatially distinct frequency specific MEG networks emerge from one underlying structural connectome? The role of the structural eigenmodes, NeuroImage **186**, 211 (2019).

[10] S. Petkoski and V. K. Jirsa, Normalizing the brain connectome for communication through synchronization, Network Neurosci. **6**, 722 (2022).

[11] W. S. Lee, E. Ott, and T. M. Antonsen, Large Coupled Oscillator Systems with Heterogeneous Interaction Delays, Phys. Rev. Lett. **103**, 044101 (2009).

[12] A. Papachristodoulou and A. Jadbabaie, Synchronization in oscillator networks with heterogeneous delays, switching topologies and nonlinear dynamics, in *Proceedings of the 45th IEEE Conference on Decision and Control* (IEEE, Piscataway, NJ, 2006), pp. 4307–4312.

[13] J. A. Roberts, L. L. Gollo, R. G. Abeysuriya, G. Roberts, P. B. Mitchell, M. W. Woolrich, and M. Breakspear, Metastable brain waves, Nat. Commun. **10**, 1056 (2019).

[14] Y. Kuramoto, Self-entrainment of a population of coupled nonlinear oscillators, in *International Symposium on Mathematical Problems in Theoretical Physics* (Springer, New York, 1975), pp. 420–422.

[15] F. A. Rodrigues, T. K. D. M. Peron, P. Ji, and J. Kurths, The Kuramoto model in complex networks, Phys. Rep. **610**, 1 (2016).

[16] J. A. Acebrón, L. L. Bonilla, C. J. P. Vicente, F. Ritort, and R. Spigler, The Kuramoto model: A simple paradigm for synchronization phenomena, Rev. Mod. Phys. **77**, 137 (2005).

[17] S. O. Jeong, T. W. Ko, and H. T. Moon, Time-Delayed Spatial Patterns in a Two-Dimensional Array of Coupled Oscillators, Phys. Rev. Lett. **89**, 154104 (2002).

[18] T. W. Ko and G. B. Ermentrout, Effects of axonal time delay on synchronization and wave formation in sparsely coupled neuronal oscillators, Phys. Rev. E **76**, 056206 (2007).

[19] S. Petkoski, A. Spiegler, T. Proix, P. Aram, J. J. Temprado, and V. K. Jirsa, Heterogeneity of time delays determines synchronization of coupled oscillators, Phys. Rev. E **94**, 012209 (2016).

[20] S. H. Strogatz, From Kuramoto to Crawford: Exploring the onset of synchronization in populations of coupled oscillators, Phys. D (Amsterdam) **143**, 1 (2000).

[21] A. Arenas, A. Diaz-Guilera, J. Kurths, Y. Moreno, and C. Zhou, Synchronization in complex networks, Phys. Rep. **469**, 93 (2008).

[22] L. Muller, F. Chavane, J. Reynolds, and T. J. Sejnowski, Cortical travelling waves: Mechanisms and computational principles, Nat. Rev. Neurosci. **19**, 255 (2018).

[23] Z. W. Davis, G. B. Benigno, C. Fletterman, T. Desbordes, C. Steward, T. J. Sejnowski, J. Reynolds, and L. Muller, Spontaneous traveling waves naturally emerge from horizontal fiber time delays and travel through locally asynchronous-irregular states, Nat. Commun. **12**, 6057 (2021).

[24] M. Breakspear, S. Heitmann, and A. Daffertshofer, Generative models of cortical oscillations: Neurobiological implications of the Kuramoto model, Front. Hum. Neurosci. **4**, 190 (2010).

[25] J. Cabral, E. Hugues, O. Sporns, and G. Deco, Role of local network oscillations in resting-state functional connectivity, NeuroImage **57**, 130 (2011).

[26] H. Choi and S. Mihalas, Synchronization dependent on spatial structures of a mesoscopic whole-brain network, PLoS Comput. Biol. **15**, e1006978 (2019).

[27] See Supplemental Material at http://link.aps.org/supplemental/10.1103/PhysRevResearch.5.013159 for supplemental figures and movies.

[28] R. C. Budzinski, T. T. Nguyen, J. Đoàn, J. Mináč, T. J. Sejnowski, and L. E. Muller, Geometry unites synchrony, chimeras, and waves in nonlinear oscillator networks, Chaos: Interdiscip. J. Nonlinear Sci. **32**, 031104 (2022).

[29] M. K. S. Yeung and S. H. Strogatz, Time Delay in the Kuramoto Model of Coupled Oscillators, Phys. Rev. Lett. **82**, 648 (1999).

[30] C. R. Laing, Travelling waves in arrays of delay-coupled phase oscillators, Chaos: Interdiscip. J. Nonlinear Sci. **26**, 094802 (2016).

[31] L. Timms and L. Q. English, Synchronization in phase-coupled Kuramoto oscillator networks with axonal delay and synaptic plasticity, Phys. Rev. E **89**, 032906 (2014).

[32] B. Ermentrout and T. W. Ko, Delays and weakly coupled neuronal oscillators, Philos. Trans. R. Soc. A **367**, 1097 (2009).

[33] T. W. Ko, S. O. Jeong, and H. T. Moon, Wave formation by time delays in randomly coupled oscillators, Phys. Rev. E **69**, 056106 (2004).

[34] C. Grabow, S. M. Hill, S. Grosskinsky, and M. Timme, Do small worlds synchronize fastest? EPL (Europhys. Lett.) **90**, 48002 (2010).

[35] F. Sorrentino, L. M. Pecora, A. M. Hagerstrom, T. E. Murphy, and R. Roy, Complete characterization of the stability of cluster synchronization in complex dynamical networks, Sci. Adv. **2**, e1501737 (2016).

[36] Y. Sugitani, Y. Zhang, and A. E. Motter, Synchronizing Chaos with Imperfections, Phys. Rev. Lett. **126**, 164101 (2021).

[37] P. Davis, *Circulant Matrices* (Wiley, New York, 1979).

[38] P. Hagmann, L. Cammoun, X. Gigandet, R. Meuli, C. J. Honey, V. J. Wedeen, and O. Sporns, Mapping the structural core of human cerebral cortex, PLoS Biol. **6**, e159 (2008).

[39] L. Muller, A. Destexhe, and M. Rudolph-Lilith, Brain networks: Small-worlds, after all? New J. Phys. **16**, 105004 (2014).

[40] H. A. Swadlow and S. G. Waxman, Axonal conduction delays, Scholarpedia **7**, 1451 (2012).

[41] E. Litvina, A. Adams, A. Barth, M. Bruchez, J. Carson, J. E. Chung, K. B. Dupre, L. M. Frank, K. M. Gates, K. M. Harris, H. Joo, J. W. Lichtman, K. M. Ramos, T. Sejnowski, J. S. Trimmer, S. White, and W. Koroshetz, BRAIN initiative: Cutting-edge tools and resources for the community, J. Neurosci. **39**, 8275 (2019).

[42] D. Witthaut, F. Hellmann, J. Kurths, S. Kettemann, H. Meyer-Ortmanns, and M. Timme, Collective nonlinear dynamics and self-organization in decentralized power grids, Rev. Mod. Phys. **94**, 015005 (2022).

[43] A. E. Motter, S. A. Myers, M. Anghel, and T. Nishikawa, Spontaneous synchrony in power-grid networks, Nat. Phys. **9**, 191 (2013).

[44] https://mullerlab.github.io.

[45] https://www.computeontario.ca.

[46] https://alliancecan.ca.

Supplementary material - Analytical prediction of specific spatiotemporal patterns in nonlinear oscillator networks with distance-dependent time delays

Roberto C. Budzinski,[1, 2, 3, *] Tung T. Nguyen,[1, 2, 3, *] Gabriel B. Benigno,[1, 2, 3, *]
Jacqueline Đoàn,[1, 2, 3] Ján Mináč,[1, 3] Terrence J. Sejnowski,[4, 5] and Lyle E. Muller[1, 2, 3, †]
[1] *Department of Mathematics, Western University, London, ON, Canada*
[2] *Brain and Mind Institute, Western University, London, ON, Canada*
[3] *Western Academy for Advanced Research, Western University, London, ON, Canada*
[4] *The Salk Institute for Biological Studies, La Jolla, CA, USA*
[5] *Division of Biological Sciences, University of California at San Diego, La Jolla, CA, USA*

I. OSCILLATORS WITH NON-IDENTICAL NATURAL FREQUENCY

Our approach can be applied to networks of oscillators with non-identical natural frequency. In this example, the natural frequency is given by $\omega_i \in [50, 63]$, which is obtained from a random, uniform distribution. Figure S1 shows the analysis of our approach applied to the same network studied in the main text, but with non-identical natural frequencies. Without delay, the network depicts a high level of phase synchronization, which is represented by the horizontal structures in the plot (Fig. S1a). When we add heterogeneous time delays to the coupling, the network transitions to a wave pattern (Fig. S1b), which is captured by our complex-valued approach using the delay operator (Fig. S1c). The Kuramoto order parameter corroborates this scenario (Fig. S1d), where the network without delay has $R(t) \approx 1$ and the network with heterogeneous time delays has $R(t) \approx 0$.

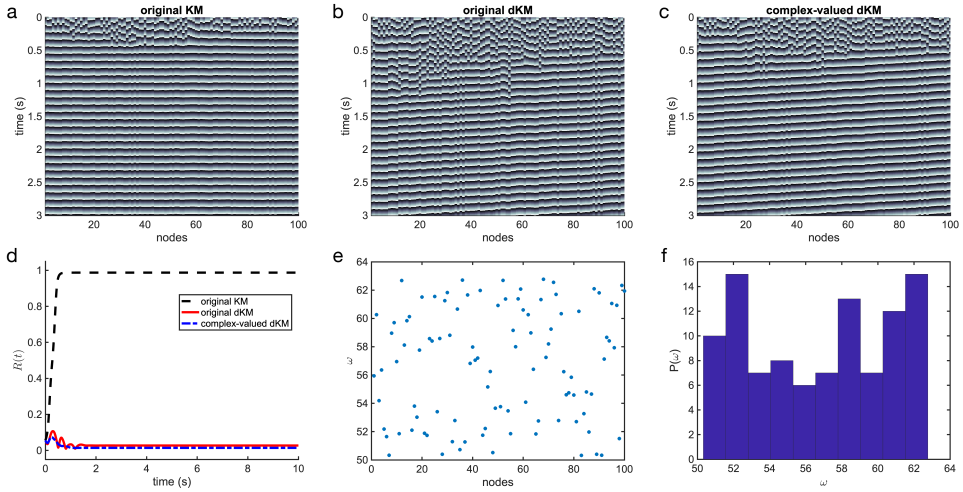

Figure S1. Analyses of an oscillator network with nonidentical natural frequency. **(a)** Without delays, the network transitions to phase synchronization. **(b)** With heterogeneous time delays in the coupling, the network transitions to a wave pattern, **(c)** which is captured by our complex-valued approach. **(d)** The Kuramoto order parameter for these three cases. **(e), (f)** Here, the oscillators have non-identical natural frequencies.

---

[*] These authors contributed equally
[†] lmuller2@uwo.ca

II. EXAMPLES OF THE DYNAMICS OF TIME DELAYED NETWORKS

Figure S2a shows the eigenvalues λ of the matrix $\boldsymbol{W}$ in the delayed, and non-delayed case ($\epsilon\boldsymbol{A}$). Here, we consider the same time delays than studied in the main text (Figs. 2 and 3), where $\tau_{ij} \in [2, 62]$ ms. In the non-delayed case, the eigenvalue with the largest real part is related to the eigenvector $\boldsymbol{v}_1 = (1, 1, \cdots, 1)^{\mathrm{T}}$ thus we have $\mathrm{Arg}[(\boldsymbol{v}_1)_i] = 0 \; \forall i \in [1, N]$. Therefore the first eigenmode captures the synchronized state (μ_1), determining the behavior of the system in the non-delayed case. In this case, random initial conditions evolve to phase synchronization due to the coupling. On the other hand, the addition of the heterogeneous delay leads to a rotation of the eigenvalues in the complex plane (see Fig. 2f in the main text), where each mode has a different rotation due to term η_{ij} in the matrix $\boldsymbol{W}$. This leads to the dominance of the 3rd and 99th modes, in terms of the real part of the eigenvalues (here, $\lambda_3 = \lambda_{99}$). We then observe that these modes determine the dynamics of the system. In this case, the system exhibits wave patterns as time evolves.

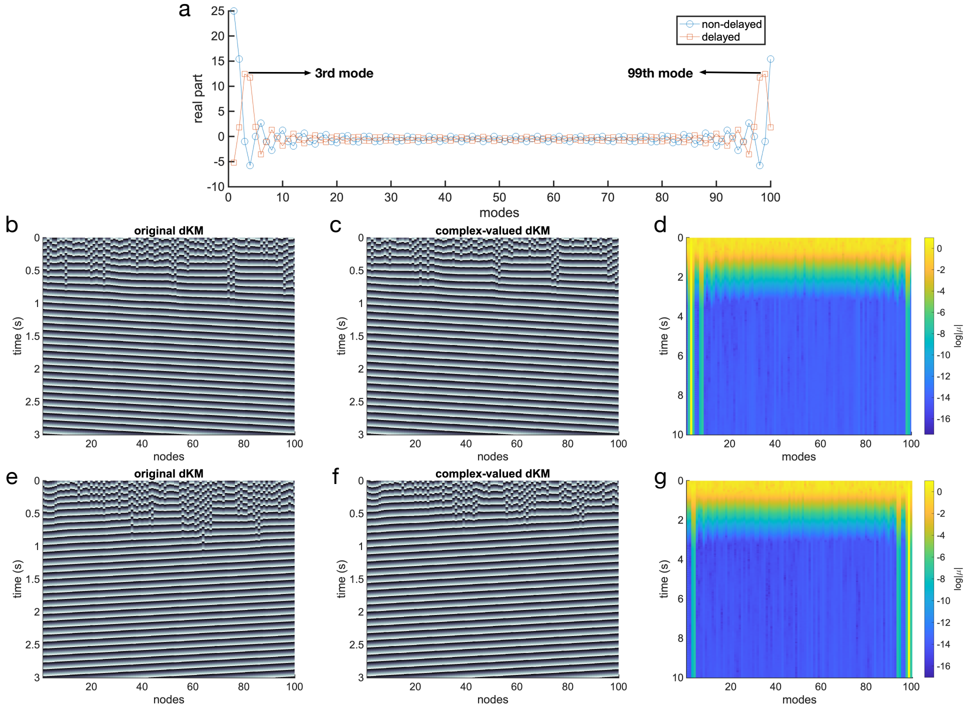

Figure S2. **(a)** Eigenvalues for the matrices $\epsilon\boldsymbol{A}$ (non-delayed) and $\boldsymbol{W}$ (delayed) used in the main text. Here, the non-delayed case shows that the first mode has the eigenvalue with the largest real part, therefore defining the dynamics of the system and leading the network to reach phase synchronization. On the other hand, the addition of the heterogeneous delay leads the eigenvalues to rotate in the complex plane (see Fig. 2f in the main text), which results in the eigenvalues associated with 3rd and 99th modes having the largest real parts. In this case, the addition of delay leads the system to transition from phase-synchronization to exhibiting wave patterns. Examples of wave patterns induced in this case are depicted for different initial conditions. **(b), (c), (d)** In the first case, the system transitions to a wave pattern defined by the 3rd mode. **(e), (f), (g)** In the second case, the system depicts a wave pattern defined by the 99th mode.

Further, Fig. S2 also depicts realizations with different initial conditions for the original dKM and complex-valued dKM. Figures S2b and S2c show examples of wave patterns where the dynamics is determined by the 3rd mode for the original dKM and the complex-valued dKM, respectively. Moreover, Fig. S2d shows the eigenmodes contribution in this case, where one can observe the dominance of the 3rd mode. Otherwise, if different initial conditions are considered, the system can depict waves patterns where the dynamics is determined by the 99th mode (Figs. S2e and S2f). The dominant contribution, in this case, is given by the 99th mode (Fig. S2g).

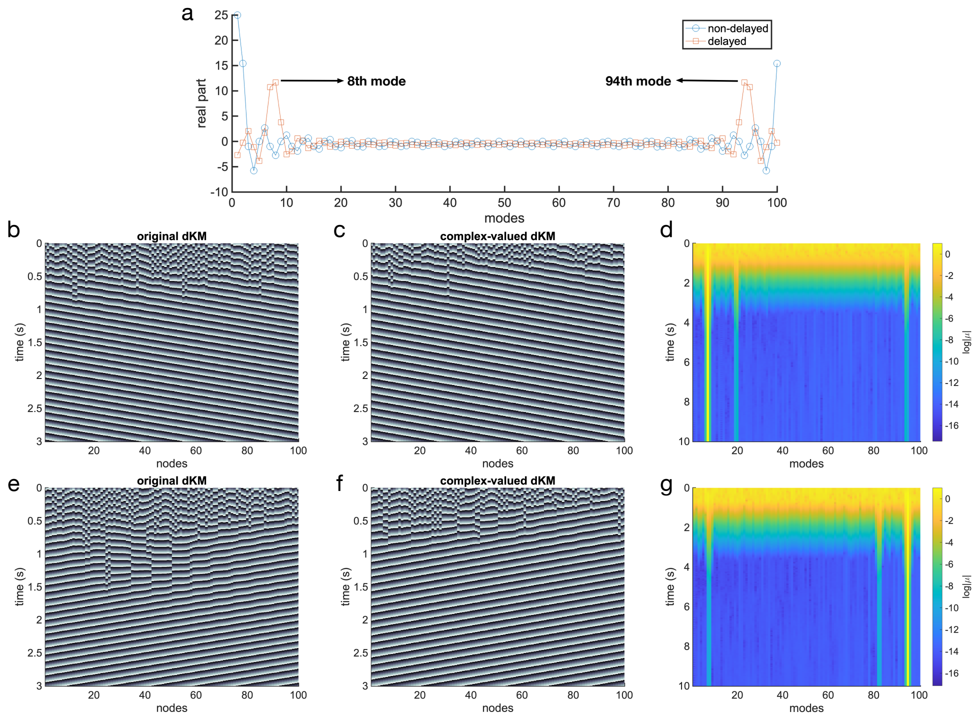

Figure S3. **(a)** Eigenvalues for the matrices $\epsilon\boldsymbol{A}$ (non-delayed) and $\boldsymbol{W}$ (delayed) for the case where $\tau_{ij} \in [6, 160]$ ms. The non-delay case has the same structure as shown before. On the other hand, the addition of the heterogeneous delay in combination with the natural frequency of oscillators leads the eigenvalues to rotate in the complex plane, which results in the eigenvalues associated with 8th and 94th modes having the largest real parts. Thus, the system transitions to wave patterns defined by these modes. **(b)**, **(c)**, and **(d)** In the first case, the system transitions to a wave pattern defined by the 8th mode. **(e)**, **(f)**, and **(g)** For different initial conditions, the system depicts a wave pattern defined by the 94th mode.

Furthermore, in order to exemplify how our approach allows us to control and predict the dynamics of the network, we show a different example of a heterogeneous delayed Kuramoto network. Here, we use the same procedure as described in the main text, but we change the speed of propagation (ν) in a such way that $\tau_{ij} \in [6, 160]$ ms. The combination of the natural frequency of oscillators ω with the delay matrix $\boldsymbol{\tau}$ (which depends on ν) leads to a different rotation of the eigenvalues in the complex plane, therefore allowing the system to reach different wave patterns. Figure S3a shows the eigenvalues of the non-delayed matrix ($\epsilon\boldsymbol{A}$), where the 1st eigenvalue has the largest real part, and also the eigenvalues of the delayed matrix ($\boldsymbol{W}$, where the 8th and 94th eigenvalues have the largest real parts. Therefore, the addition of this specific delay matrix in the system allows the network to depict wave patterns related to those modes. This behavior is shown in the other panels of Fig. S3. First, panels (b) and (c) show the spatiotemporal dynamics for the original dKM and the complex-valued dKM, respectively, where the wave pattern is defined by the 8th mode – the eigenmodes contribution is depicted in Fig. S3d. On the other hand, when different initial conditions are considered, the system can reach a wave state defined by the 94th mode, which is depicted in panels (e), (f), and (g). Moreover, different modes can be accessed when different combinations of the delay matrix (which depends on ν) and the oscillators' natural frequency are considered.

III. MOVIE CAPTIONS

Movie S1: (left) Argument (element-wise evaluated) of the 3rd eigenvector of the matrix $\boldsymbol{W}$ studied in Fig. 2 of the main text. In this case, this eigenvector is associated with the largest eigenvalue (real part) when we considered the delayed system. In this case, this represents a wave traveling in the clockwise direction. (right) Numerical simulation of the Kuramoto network with heterogeneous time delays studied in the main text. Here, each oscillator is represented on the circle and its phase is plotted as a function of time in color-code varying from black tones ($-\pi$) to white tones (π). In this case, we can observe that the argument of the eigenvector predicts the spatiotemporal pattern observed in the numerical simulation.

Movie S2: (left) Argument (element-wise evaluated) of the 99th eigenvector of the matrix $\boldsymbol{W}$ studied in Fig. 2 of the main text. In this case, this eigenvector is associated with the largest eigenvalue (real part) when we considered the delayed system. In this case, this represents a wave traveling in the counter-clockwise direction. (right) Numerical simulation of the Kuramoto network with heterogeneous time delays studied in the main text. Here, each oscillator is represented on the circle and its phase is plotted as a function of time in color-code varying from black tones ($-\pi$) to white tones (π). In this case, we can observe that the argument of the eigenvector predicts the spatiotemporal pattern observed in the numerical simulation.

Movie S3: (left) Argument (element-wise evaluated) of the eigenvector associated with the largest (real part) eigenvalue of the matrix $\boldsymbol{W}$ based on the Human Connectome Project (Fig. 5 of the main text) in the case that time delays are not considered. This represents a zero phase difference across oscillators. (right) Numerical simulation of the Kuramoto network based on the Human Connectome Project network in the case that time delays are not considered. Here, each oscillator is represented by a dot in a 3D space and its phase is plotted as a function of time in color-code varying from black tones ($-\pi$) to white tones (π). We can observe that the argument of the eigenvector predicts the spatiotemporal pattern observed in the numerical simulation.

Movie S4: (left) Argument (element-wise evaluated) of the eigenvector associated with the largest (real part) eigenvalue of the matrix $\boldsymbol{W}$ based on the Human Connectome Project (Fig. 5 of the main text) in the case that distance dependent time delays are considered. This represents a traveling wave. (right) Numerical simulation of the Kuramoto network based on the Human Connectome Project network with distance dependent time delays. Here, each oscillator is represented by a dot in a 3D space and its phase is plotted as a function of time in color-code varying from black tones ($-\pi$) to white tones (π). We can observe that the argument of the eigenvector predicts the spatiotemporal pattern observed in the numerical simulation.

IV. CODE AVAILABILITY

An open-source code repository for this work is available on GitHub: http://mullerlab.github.io.

4 | Waves traveling over a map of visual space can ignite short-term predictions of sensory input

In the previous chapter, a complex-valued implementation of the Kuramoto model, augmented with distance-dependent delays between connections, provided a reduced description of the traveling waves of cortex, and enabled analytical insight into their emergence. Here, we used that dynamical model of traveling waves in a machine-learning framework, treating it as a recurrent neural network, and we asked how useful the traveling wave dynamics might be in tasks of visual forecasting.

nature communications

Article

https://doi.org/10.1038/s41467-023-39076-2

Waves traveling over a map of visual space can ignite short-term predictions of sensory input

Received: 19 August 2022

Accepted: 25 May 2023

Published online: 09 June 2023

Check for updates

Gabriel B. Benigno[1,2,3], **Roberto C. Budzinski**[1,2,3], **Zachary W. Davis**[4], **John H. Reynolds**[4] & **Lyle Muller**[1,2,3]

Recent analyses have found waves of neural activity traveling across entire visual cortical areas in awake animals. These traveling waves modulate the excitability of local networks and perceptual sensitivity. The general computational role of these spatiotemporal patterns in the visual system, however, remains unclear. Here, we hypothesize that traveling waves endow the visual system with the capacity to predict complex and naturalistic inputs. We present a network model whose connections can be rapidly and efficiently trained to predict individual natural movies. After training, a few input frames from a movie trigger complex wave patterns that drive accurate predictions many frames into the future solely from the network's connections. When the recurrent connections that drive waves are randomly shuffled, both traveling waves and the ability to predict are eliminated. These results suggest traveling waves may play an essential computational role in the visual system by embedding continuous spatiotemporal structures over spatial maps.

Five percent of synapses received by a neuron in the visual cortex arrive through the feedforward (FF) pathway that conveys sensory input from the eyes[1–4]. While these FF synapses are strong[5], "horizontal" recurrent connections coming from within the cortical region make up about 80% of total synaptic inputs, with 95% of these connections arising from a very local patch (2 mm) around the cell[4]. The anatomy of the visual system thus indicates that cortical neurons interact with other neurons across the retinotopically organized maps[6] that assign nearby points in visual space to nearby points in a cortical region via these horizontal connections. Models of the visual system predominantly focus only on FF[7,8] and feedback (FB)[9] connections. One result of this focus is that, in models of the visual system, neurons in the visual cortex are often modeled as non-interacting "feature detectors" with fixed selectivity to features in visual input (driven by FF connections) that can be modulated by expectations generated in higher visual areas (driven by FB connections). Neuroscientists have long been interested in how horizontal connections shape neuronal selectivity[10,11] and "non-classical" receptive fields[12–16]. More recently, neuroscientists have also been interested in adding these connections to deep learning models to understand neuronal selectivity in the visual cortex[17,18]. It remains unclear, however, how horizontal connections shape the moment-by-moment computations in the cortex while processing visual input.

Recent analyses of large-scale recordings have revealed that horizontal connections profoundly shape spatiotemporal dynamics in the cortex. Traveling waves driven by horizontal connections have been observed in the visual cortex of anesthetized animals[19–24]. The relevance of traveling waves had previously been called into question, as they were thought to disappear in the awake state[25] or to be suppressed by high-contrast visual stimuli[22,26]. Recent analyses of neural activity at the single-trial level, however, have revealed spontaneous[27] and stimulus-evoked[28] activity patterns that travel smoothly across entire cortical regions in awake, behaving primates during normal vision. These neural traveling waves (nTWs) shift the balance of excitation and inhibition as they propagate across the cortex, sparsely modulating spiking activity as they pass[29]. Because they drive

---

[1]Department of Mathematics, Western University, London, ON, Canada. [2]Brain and Mind Institute, Western University, London, ON, Canada. [3]Western Academy for Advanced Research, Western University, London, ON, Canada. [4]The Salk Institute for Biological Studies, La Jolla, CA, USA.
e-mail: lmuller2@uwo.ca

fluctuations in neural excitability[27,30], nTWs show that neurons at one point in a visual area (representing a small section of visual space) can strongly interact with neurons across the entire cortical region. These results thus indicate that cortical neurons may share information about visual scenes broadly across the retinotopic map through nTWs generated by horizontal connections.

What computations, then, can be done with waves of neural activity traveling across a map of visual space? To address this question, we studied a complex-valued neural network (cv-NN) processing visual inputs ranging from simple stimuli to natural movies. In these networks, activity at each node is described by a complex number. Complex numbers extend the arithmetic of the real number system, and as with standard, real-valued neural networks, nodes receive inputs based on connection weights, with the activity of each node determined by an activation function. The network state is then described by a vector of complex numbers, each element of which can represent the activation of a small patch of neurons in a single region of the visual cortex[31,32]. cv-NNs exhibit similar or superior performance to standard, real-valued neural networks in many supervised learning tasks[33] and have been used effectively in explaining biological neural dynamics[34]. Here, we modified the standard FF architecture used in deep learning and computer vision to include horizontal recurrent connections, where neurons in a single processing layer form a web of interconnections similar to the horizontal connections in the visual cortex. Horizontal recurrent connections are thought to provide advantages[17] over the standard FF architecture used in computer vision tasks[8,35]; however, current methods for incorporating recurrent horizontal fibers to convolutional network models of the visual system severely limit both the time window over which recurrent activity can be considered and the ease with which the networks can be trained[17]. In recent work, we have introduced a mathematical approach to understand the recurrent dynamics in a specific complex-valued model[36]. Here, we leverage this understanding to train recurrent complex-valued networks to process visual inputs, ranging from simple stimuli to naturalistic movie scenes. The resulting networks can predict learned movies many frames into the future, entirely from their internal dynamics alone, without external input. During prediction, the recurrent network exhibits prominent nTWs, ranging from simple waves propagating out from a small local input[28] to complex traveling wave patterns[37], raising the possibility that nTWs enable continuous predictions of dynamic and naturalistic visual input.

Results

The cv-NN consists of an input layer sending movie frames to a recurrently connected neural network. An individual movie frame, serving as input to the network, is represented by a two-dimensional grid of pixels (input frame, Fig. 1a), and each pixel projects to the recurrently connected layer through FF connections (red lines, Fig. 1a).

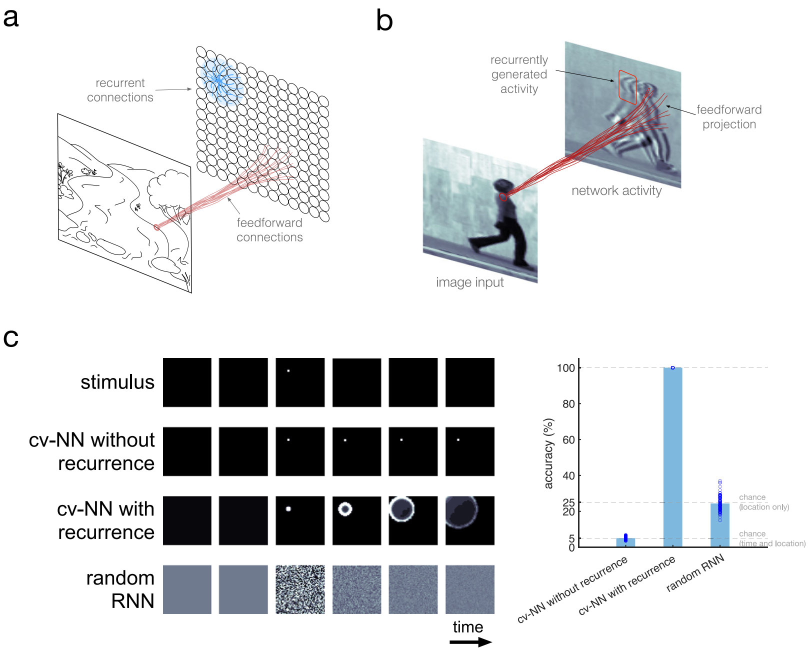

Fig. 1 | A topographic recurrent network model encodes spatiotemporal information of video frames via internal wave activity. a Schematic of the complex-valued neural network (cv-NN) model. Nodes (circles) are arranged on a two-dimensional grid and are recurrently connected (blue) locally in space like the cortical sheet. A natural image input projects locally into the network via feedforward connections (red), mimicking retinotopy. **b** Example dynamic of the network model. Due to the spatially local projection of the input image, an imprint of the image is visible in the grid of network activity. Due to the local recurrent connectivity, intrinsic wave activity is generated alongside the input projection. **c** Top row: In a sequence of six frames, exactly one of the first five contains a point stimulus, and the other frames do not. These frames are sequentially input to the network. Second row: When the cv-NN has no recurrence, the stimulus projection remains stationary. Third row: With recurrence, from the time of stimulus, cv-NN activity contains a projection of the stimulus and a wave radiating outward. Fourth row: Activity in a randomly connected recurrent neural network (RNN) following stimulus onset has a spatially disorganized structure, reflecting its lack of topography and distance-dependent time delays. Right: A linear classifier that received the final network state in the no-recurrence case could not predict the time or location beyond chance-level accuracy (5% overall), and in the random-RNN case, could predict the time but not the location beyond chance (25% overall). In contrast, using the classifier with the sixth with-recurrence network state allowed 100% accuracy since the feedforward projection of the point stimulus triggered a radiating wave that encoded the time and location of the stimulus in the subsequent network states. $N = 100$ trials for each group. Mean ± standard deviation of 5.09 ± 0.94, 100 ± 0, and 24.42 ± 4.13, respectively. Source data are provided as a Source Data file.

The recurrently connected layer is arranged on a two-dimensional grid, analogous to the retinotopic arrangement of neurons in visual regions. Horizontal interconnections within the cv-NN then drive recurrent interactions in the network (blue lines, Fig. 1a). Both FF and horizontal recurrent projections in the cv-NN are matched to the approximate scale of connectivity in visual cortex[38,39] so that a single pixel in an input movie drives a local patch of neurons, with overlapping horizontal connections, in the cv-NN. Lastly, nodes in the recurrent layer communicate with time delays approximating axonal conduction speeds along horizontal fibers[40], which have recently been shown to shape spiking neural activity into nTWs[29]. The combination of FF input and dense interconnections generates complex patterns of activity in the recurrent layer (Fig. 1b). Here, we focus on these recurrent activity patterns to understand their computational role for movie inputs ranging from simple to complex.

nTWs can simultaneously encode stimulus position and time of onset over spatial maps

To illustrate how nTWs propagating over sensory maps could facilitate visual computation, we first studied the dynamics generated in response to a single point stimulus. Without recurrent connections, a short point stimulus generates a small bump of activity that remains centered on the point of input ("cv-NN without recurrence", Fig. 1c). With recurrent connections, however, the point stimulus generates a wave that propagates out from the point of input ("cv-NN with recurrence", Fig. 1c). We then studied these stimulus-evoked waves, which are similar in form to those previously observed in the visual cortex of awake primate[28], in a simple decoding task. Specifically, we let the point stimulus appear at a random time and stimulus location in a series of input frames and then trained a linear classifier to decode the time and location of stimulus onset from the network activity at the final frame. As expected, in the cv-NN without recurrent connections, the classifier performed at chance-level accuracy in this task (Fig. 1c, right; "Methods"—"Stimulus prediction task"). With recurrence, however, the classifier selects the correct time and location of stimulus appearance from the final network state with 100% accuracy. Finally, while standard recurrent neural networks (RNNs) can encode time[41], an RNN with random connections (and hence lacking the local connectivity and distance-dependent time delays in the cv-NN) also performs at chance level in this task, which requires decoding both stimulus location and onset time (Fig. 1c). This simple illustration shows that traveling waves of neural activity when propagating on an orderly retinotopic map can simultaneously encode stimulus location and onset time, even after the stimulus is no longer present.

nTWs aid forecasting movie inputs from simple to complex

Can nTWs enable the processing of the complex, dynamic, and nonstationary visual scenes that we encounter in our natural experience? We approached this question in several steps. We first asked whether, given an input frame from a movie, the cv-NN could be trained to accurately predict the following frame. To perform this more complicated task, we introduced a learning rule that requires training only a linear readout of the recurrent layer (Fig. 2a). This procedure is analogous to a complex-valued implementation of the reservoir computing paradigm[42], which has recently found wide applications in nonlinear dynamics and physics. In the reservoir computing framework, an input signal drives activity in a recurrently connected layer. Activity in the recurrent layer is then decoded by a set of output weights, which are trained to produce a target output signal. Because of both its efficacy and relative efficiency in training, this framework has proven promising for learning predictive models of chaotic systems[43,44], and reservoir computing has recently been used to learn and predict a range of important systems in physics[45,46]. This training process, however, has never before been applied to naturalistic movie scenes. We find the cv-NN can be reliably and efficiently trained to predict the next frame in a movie input (Supplementary Table 2, Moving Bump Input). With a cv-NN trained on a movie, the predicted next frame can then be provided as input in place of the original movie (Fig. 2b). Recent work on neural networks for processing movies has focused on predicting the next frame in a video sequence based on training on a large database of inputs[47–49]. In some cases, these predictions can then be fed back as input, allowing the network to recursively generate predictions from its own internal weights[50–58]. We will call this process, where during prediction, a network receives no external movie input and generates future predictions solely from its internal structure, *closed-loop forecasting* (CLF). Previous work has developed networks that can perform accurate CLF on the order of ten frames into the future[50–58], with predicted frames becoming increasingly blurry. In this work, we asked a cv-NN to learn and perform CLF on individual movies. We find that cv-NNs trained on an individual movie can self-generate sharp forecasts of that movie many (25–100) frames into the future while receiving no external input. This system can be seen as a simple dynamical autoencoder, where a few input frames can ignite the self-generation of successive frames from its internal dynamics alone. This provides a framework that can give insight into how the visual system could create predictions by continuously changing weights based on its sensory input to make short-term extrapolations into the near future. The cv-NN is an effective model for closed-loop forecasting of entire visual scenes, generating accurate forecasts for movies of a few thousand pixels per frame using only a few thousand recurrently connected nodes.

The visual cortex readily processes and operates on dynamic visual inputs on timescales of milliseconds to seconds. We then asked whether closed-loop forecasting in this system could work on the scale of tens to hundreds of frames in an input movie. Starting with the first half of a movie containing a simple moving bump stimulus tracing out a trajectory in two-dimensional space (Fig. 2c), we find that the trained cv-NN can produce the entire second half of the movie as output from its trained synaptic weights alone (Fig. 2d and Supplementary Movie 1). As in the previous example, activity in the recurrent layer exhibits a dynamic spatiotemporal pattern extending beyond the immediate FF imprint of the stimulus and structured by the recurrent connections in the network (Fig. 2e and Supplementary Movie 1). These results demonstrate that recurrent cv-NNs can produce simple video inputs from their recurrent connections through this training process. Finally, when we remove the recurrent connections, the cv-NN produces an activity pattern that represents only the average of FF stimulus imprints without having learned the underlying spatiotemporal process[47]. In this case, the cv-NN no longer produces an accurate closed-loop forecast (Fig. 2f). These results demonstrate the importance of both the spatiotemporal patterns in the cv-NN and the horizontal recurrent dynamics generating them.

We find that closed-loop forecast performance in this system depends on two key factors: (1) the ratio of horizontal recurrent strength to feedforward input strength and (2) the spatial extent of the recurrence. To study the first factor in detail, we measured closed-loop forecast performance using an index of structural similarity (SSIM)[59], which quantifies the perceptual match between two images, ranging between 0 (perfect mismatch) and 1 (perfect match). A threshold on the SSIM, determined through test comparisons between an original and noise-corrupted version of a movie, then provides a quantitative criterion for a successful closed-loop forecast (see Supplementary Fig. 2). We studied SSIM between movie frames produced by the closed-loop forecast process and the ground truth at different ratios of recurrence to input (Fig. 3a; see also Supplementary Fig. 1 and "Methods"—"Network connectivity" and "Network dynamics"). Once the stimulus is removed and the closed-loop forecast begins (video frame 1, Fig. 3a), forecast performance in cv-NNs with low recurrent strength quickly drops close to zero (light blue line, Fig. 3a). By contrast, cv-NNs at optimal recurrent strength sustain closed-loop

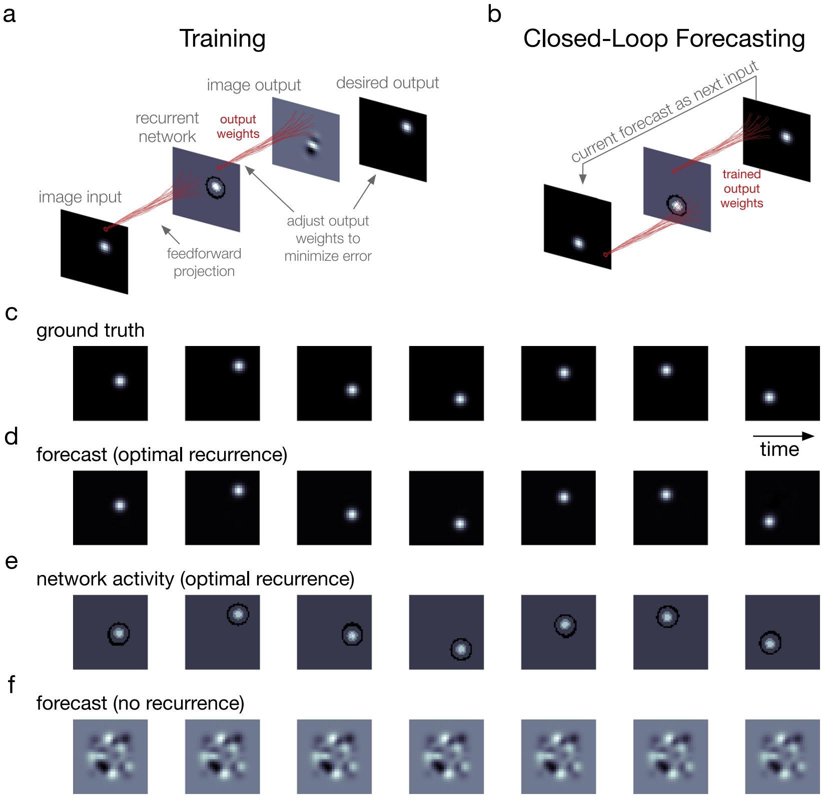

Fig. 2 | The network can forecast a simple video input many frames into the future. a As in the classification example (Fig. 1), a video frame projects into the network in a spatially local manner, and a recurrent network interaction occurs, generating internal wave activity on top of the projection. The network outputs an image from its network state via a matrix of trainable weights. Training entails one-shot linear regression between a set of network states and the corresponding desired output frames (the one-step-ahead next frames). Shown: a schematic representation of the one-shot linear regression for one time step. **b** Once training of the readout weights is complete, closed-loop forecasting begins. To properly test how well the network model learned the underlying spatiotemporal process from the training data, it is deprived of ground-truth data of any kind during this step. Instead, the forecast next frame at one time step serves as the input frame for the following time step. **c** Video frames of the data: a bump tracing an orbit. **d** Corresponding closed-loop forecasts generated by the network model with optimal recurrence. **e** Network activity for the optimal-recurrence case. Cosine of phase of activation is shown. **f** Closed-loop forecast in the case without recurrence.

forecasts for long timescales (gray line, Fig. 3a), extending beyond 100 video frames into the future. Importantly, networks where recurrence is too strong also perform poorly, with SSIM dropping near zero within a short timeframe (copper line, Fig. 3a). Systematic quantification of SSIM across ratios of recurrent strength to input strength reveals that performance is best when the recurrence and input are approximately balanced (Fig. 3b), in general agreement with the ratio of feedforward to recurrently generated synaptic drive in visual cortex[60,61]. We next studied performance as a function of the spatial extent of recurrent connectivity. The best performance occurs for recurrent lengths on approximately the same spatial scale as the moving bump stimulus (Fig. 3c), with performance dropping for recurrent lengths outside this range. This result demonstrates that recurrent connections aid closed-loop forecasting when matched to the spatial scale of the input. Horizontal recurrent connections in single visual regions span many different retinotopic scales[9,62], which could enable processing stimuli at multiple spatial scales or moving stimuli with changing scales by the visual system.

The visual system readily processes richly textured and naturalistic visual scenes. To examine this type of stimulus in the cv-NN, we considered naturalistic video inputs for next-frame prediction and closed-loop forecasting. To do this, we used videos from the Weizmann Human Action Dataset[63]. As above, we trained linear readout weights of the cv-NN on these individual naturalistic movie inputs (Fig. 4a) and then tested whether, given the first half of the input movie, the network could produce the second half in a closed-loop forecast (Fig. 4b). Even with a much more sophisticated input than the previous examples, the cv-NN can be trained rapidly and efficiently on the natural movie inputs (Supplementary Table 2, Walking Person Input). As in previous examples, at optimal values of the network parameters (“Methods”—“Parameter optimization”), the cv-NN accurately produces the natural movie using only its connection weights (Fig. 4c, d and Supplementary Movie 2). In this case, the recurrent connections in the cv-NN create complex wave patterns (Fig. 4e and Supplementary Movie 2). The recurrent connections and their resulting complex activity patterns are important for success in this task, as networks without recurrence do not produce accurate closed-loop forecasts (Fig. 4f).

We then studied what specific features of the recurrent connections enable predicting naturalistic movie inputs. As in the moving bump example, networks perform best when recurrence and input are approximately balanced, and the performance quickly decays when the recurrence is too weak or too strong (Fig. 5a, b). This result shows that, as in the simple case of the moving bump, the complex

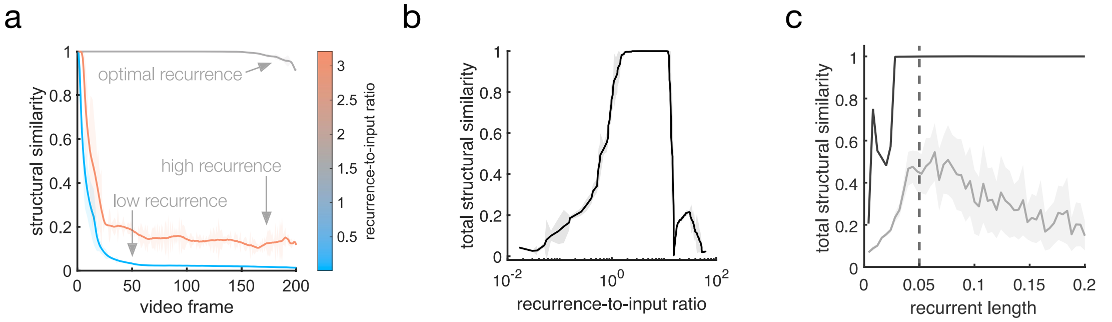

Fig. 3 | Moving bump forecast performance depends on specific properties of the recurrent connections. a Structural similarity (SSIM) between a forecast frame and the ground truth as a function of the closed-loop forecast video frame. Each curve corresponds to a different network parameter implementation. Curves have been smoothed by a moving-average filter (filter width of 30 time steps). Shaded error is the absolute difference between filtered and unfiltered. **b** Total structural similarity, in which a single SSIM is calculated for the whole movie as a function of the recurrence-to-input ratio. In the parameter space, each point differs only in recurrent strength. Smoothing and error shading is the same as in (**a**). **c** Total structural similarity as a function of recurrent length, which is the fraction of the network's side length spanned by one standard deviation of the Gaussian connectivity kernel. In the three-dimensional parameter space comprising the recurrent strength (rs), recurrent length (rl), and input strength (is), averages ($n = 89$) across rs-is planes at fixed rl were computed (gray curve). Solid gray line: average. The peak coincides with the standard-deviation width of the Gaussian bump stimulus (dashed vertical line). Shaded area: variance. Solid black curve: maximum structural similarity at each recurrent length. Source data are provided as a Source Data file.

spatiotemporal predictions generated by the network depend on a sophisticated interplay between input and recurrent connections. We next studied the role of connection topography and distance-dependent time delays. To do this, we started with networks that achieve accurate predictions and randomly shuffled both the connections and time delays, a control that removes the two key factors for generating nTWs in large-scale spiking network models[29] that match waves observed in the visual cortex (Fig. 6a). We then compared the closed-loop forecast performance and network activity in the topographic and shuffled cases. In the topographic case, the cv-NN produces accurate predictions and complex traveling wave patterns, as before (Fig. 6b, c). The shuffled versions of the cv-NN, however, produce spatiotemporally unstructured activity in the recurrent layer (Fig. 6d) and do not achieve accurate closed-loop forecasts, even after the cv-NN was retrained (Fig. 6e; see also Supplementary Table 3 and Supplementary Movie 3). This result demonstrates that with all other architectural features of the network held constant, a randomly connected cv-NN that does not produce nTWs cannot be trained to perform CLF using the same procedure that was previously successful. Shuffling only time delays in the cv-NN and then retraining also substantially drops closed-loop forecast performance (decreasing total structural similarity from 0.99 to 0.02). Further, reducing the conduction speed in half and then retraining also results in a substantial drop in performance (from 0.99 to 0.08). These two control analyses demonstrate that successful closed-loop forecasts depend on a range of time delays in the cv-NN. Finally, the specific spatiotemporal structure of the input movie is also important: a cv-NN at the optimal hyperparameters for a natural movie cannot be retrained to do closed-loop forecasting on a randomized (phase-shuffled) version of the same movie (Supplementary Table 1), demonstrating that the cv-NN utilizes the specific spatiotemporal correlations in the movie to generate its forecast. Taken together, these results demonstrate that the complex spatiotemporal patterns generated by horizontal recurrent connections in the cv-NN enable performance on next-frame prediction and closed-loop forecasting tasks for sophisticated natural movie inputs.

The nTW network model is capable of forecasting multiple movies without retraining

We lastly sought to understand whether the cv-NN could perform closed-loop forecasts on multiple movies it had previously learned and switch flexibly with changing inputs. To do this, we implemented a simple competitive process ("Methods"—"Movie switching") so that the network could adapt its output based on the similarity of its prediction to its input (Fig. 7a). Specifically, output weights for the cv-NN were trained on individual movies ($\mathbf{V_1}$ and $\mathbf{V_2}$, cf. "Training" in Fig. 7a) and stored in an aggregate matrix ($\mathcal{V}$, cf. "Switching" in Fig. 7a). When performing a closed-loop forecast, this extended network model can receive new input from this previously learned set, and then rapidly switch to closed-loop forecasting this new movie input within a few frames without any retraining of weights in the individual output matrices $\mathbf{V_i}$ (Fig. 7b and Supplementary Movie 4). This result demonstrates that the process of closed-loop forecasting, mediated by horizontal recurrent fibers in the network, can generalize to realistic visual conditions with multiple, changing input streams.

Discussion

In this work, we have introduced a model to understand whether traveling waves generated by horizontal connections in the visual cortex may play a computational role in processing natural visual inputs. By adapting a recurrent neural network model using a specific dynamical update rule and learning rule, this model learns to forecast video inputs ranging from simple visual stimuli to complex natural scenes. We report here a network model that can be trained to produce quantitatively verified closed-loop forecasts of richly textured naturalistic movies many frames into the future. The cv-NN introduced in this work incorporates the spatial topography and time delays important for shaping activity dynamics in single regions of the visual system[29] and provides a potential computational role for waves of neural activity traveling over maps of visual space. Whether similar principles of spatial topography could benefit RNNs, in general, remains open but represents an interesting potential direction for future work. Further, because the recurrent dynamics in the cv-NN are tractable to detailed mathematical analysis[36], this recurrent network model opens new possibilities for understanding the mechanisms underlying successful predictions studied here and for designing new applications in future work.

Closed-loop forecasting in the cv-NN demonstrates a form of short-term prediction by nTWs that may be relevant to the online processing of continuous sensory input by the visual system. Consider, for example, a batter in the game of baseball facing a pitcher who has just pitched a curveball, now hurtling toward the batter at over 100 miles per hour. In major league baseball, a pitch takes around 400

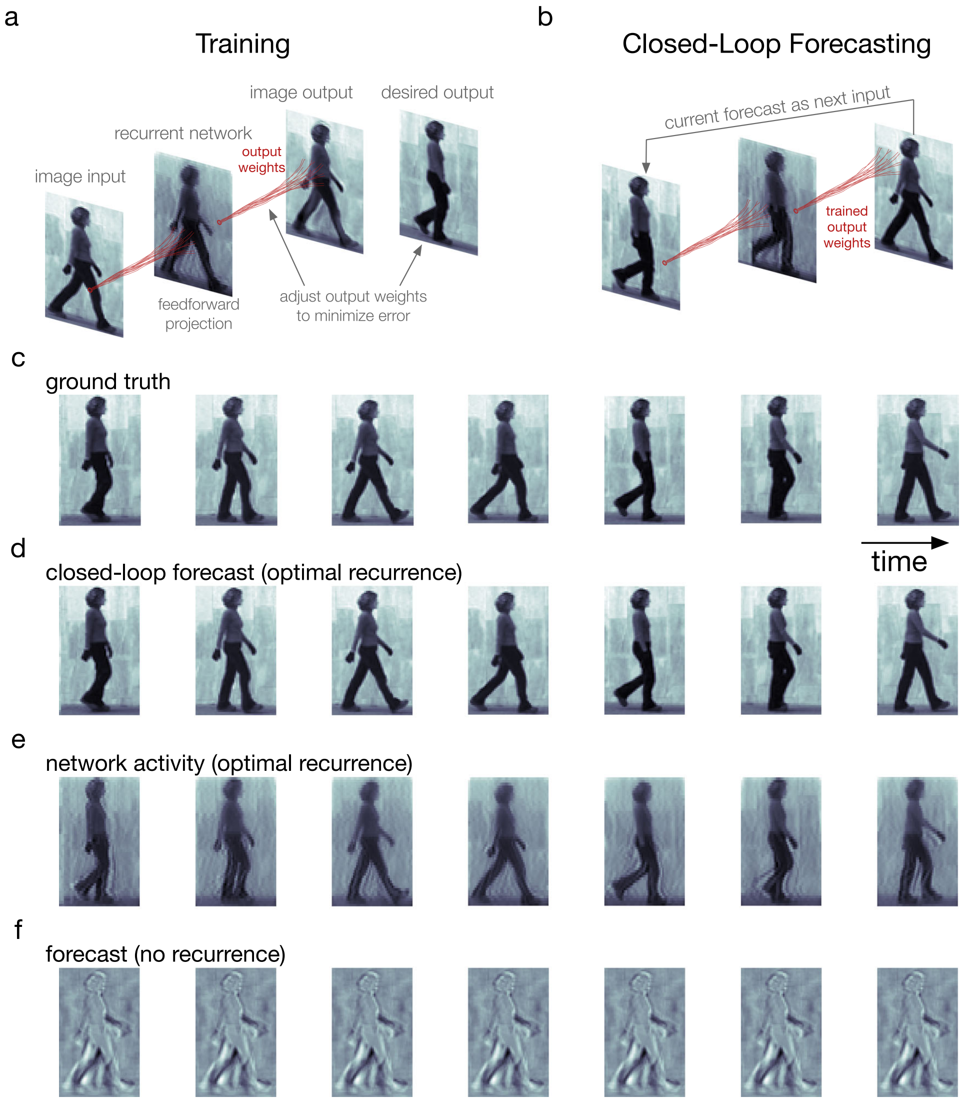
a
Training
image output
desired output
recurrent network
output weights
image input
feedforward projection
adjust output weights to minimize error
b
Closed-Loop Forecasting
current forecast as next input
trained output weights
c
ground truth
d
closed-loop forecast (optimal recurrence)
time
e
network activity (optimal recurrence)
f
forecast (no recurrence)

Fig. 4 | The recurrent network performs next-frame forecasting of a natural video input. a Training follows as in the moving bump example (Fig. 2a). **b** Next-frame closed-loop forecasting follows as in the moving bump example (Fig. 2b). **c** Video frames of the data: a person walking. **d** Corresponding closed-loop forecasts generated by the network model in the case of optimal recurrence. **e** Corresponding network states for the optimal-recurrence case (**d**). Cosine of phase is shown. **f** Same as (**d**), but in the absence of recurrence.

milliseconds to travel 60 feet from the pitcher's hand to the batter at home plate. Time is required for the neural computations that enable the batter to perceive the ball and estimate its trajectory. This includes both the time required for sensory information to travel from the retinae to relevant brain areas and the time required for computation of the ball's trajectory in space based on these signals. Assuming the entire computation can be accomplished in 150 milliseconds[64], during this time, the ball will have traveled more than 22 feet. To estimate the likely current location of the ball based on information that was available to the visual system 150 milliseconds ago, the brain may form an internal model of the ball's trajectory in space, informed by previous experience. Consistent with this idea, batters often report that, as the spinning ball travels from the pitcher's mound to home plate, the curveball suddenly changes direction, an illusory percept referred to as the curveball's "break"[65]. Short-term predictions by nTWs may represent one mechanism for rapid estimation of trajectories, as continuous spatiotemporal structures propagating over the retinotopic map. In this way, closed-loop forecasts in the cv-NN could enable the visual system to estimate the likely trajectory of the ball based on training from the previous visual experience. The curveball's "break" further recalls the process of switching predictions when the input becomes sufficiently discrepant with incoming sensory data (Fig. 7b). When the movie switches from one input to another (top row, "ground truth"), the network generates a transiently indeterminate activity pattern before jumping to the correct forecast (bottom row, "closed-loop forecast"). In this way, the cv-NN may provide a mechanistic framework for specific hypotheses in future work about the interaction of short-term predictions generated by recurrent horizontal fibers and

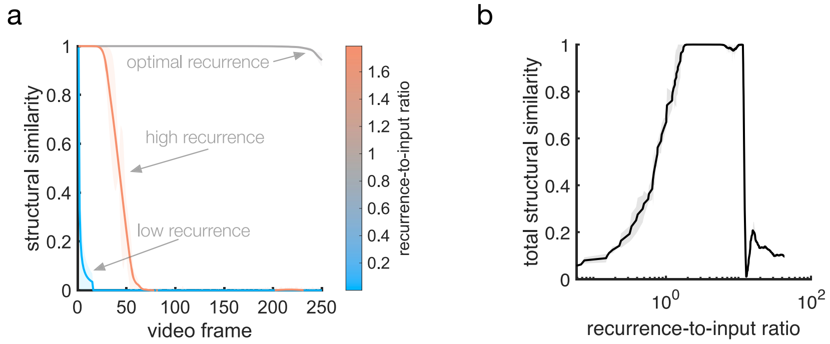

Fig. 5 | Natural movie forecast performance depends on specific properties of the recurrent connections. a Several examples of closed-loop forecast performance. Structural similarity (SSIM) between a forecast frame and the ground truth as a function of video frame during closed-loop forecasting. Each curve corresponds to a different ratio of recurrent strength to input strength. Curves have been smoothed by a moving-average filter (filter width of 30 time steps). Shaded error is the absolute difference between filtered and unfiltered. **b** Total structural similarity, in which a single SSIM is computed for the whole movie as a function of the recurrence-to-input ratio. In the parameter space, each point differs only in recurrent strength. Smoothing and error shading is the same as in (**a**). Source data are provided as a Source Data file.

continuously incoming sensory input. The cv-NN could also be useful as a model to explain how the brain encodes, stores, and recovers episodic memories of richly textured visual scenes, which studies of visual search[66] and vivid recollection[67,68] have shown are associated with activity in visual regions.

Further, while the cv-NN is not intended to be a veridical simulation of the millions of neurons contributing to nTW dynamics in the visual cortex, this network model is broadly consistent with spatiotemporal dynamics recently observed in the visual system of the alert primate. In the case of a single point stimulus (Fig. 1c), the network produces a traveling wave radiating out from the point of input. This is similar to nTWs detected in single trials during voltage-sensitive dye optical imaging in the primary visual cortex (V1) of awake macaques[28]. nTWs evoked by small visual stimuli (Gaussian spot, with a standard deviation of 0.5° of visual angle) presented during fixation consistently evoked nTWs that propagate over 7.5 mm of V1, representing a significant portion of this cortical area[69]. The spatial extent of the nTWs observed in the experiment provides a point of comparison with the model, as spatial extent determines the scale at which local populations in V1 may influence others across the retinotopic map. In the cv-NN, waves generated by small point stimuli propagate over slightly more than one-third of the network (decaying to half-amplitude after traveling over 37.5% of the network; Fig. 1c). These results demonstrate that nTWs may propagate over broadly similar spatial extents in visual cortex and in the cv-NN.

Another point of comparison with measured neural dynamics centers on the patterns evoked by moving stimuli. In the case of a moving bump stimulus (Fig. 2), the network produces a bump of activity, reflecting FF input driven by the movie but also reflecting recurrently generated activity that extends beyond the feedforward imprint of the stimulus (Fig. 2e). The radius of this recurrently generated activity is approximately twice that of the feedforward bump. This result recalls analyses of Utah array recordings in V1 of awake macaques[70]. Using a moving bar stimulus (0.5 × 4° of visual angle, moving horizontally at 6.6° per second), the authors found responses in V1 before stimuli entered neurons' classical receptive field (cf. Fig. 2C in ref. 70). The onset times of these anticipatory responses became earlier and earlier along the moving bar's trajectory. These changes in time were confirmed with computational analyses and modeling to be consistent with propagation along horizontal fibers in V1, and the spatial extent of the recurrent interactions is, again, approximately consistent with dynamics during closed-loop forecasting in the cv-NN.

The dynamics of the cv-NN are thus broadly consistent with observations of neuronal dynamics during normal processing in awake, behaving primates. Recent work has demonstrated the importance of the topographic connection patterns and axonal time delays matching those found in the visual cortex to generate nTWs in large-scale spiking network models[29]. Recent theoretical studies have developed complex-valued network models that can provide analytical insight into the time-varying dynamics of spiking neural networks[31,71], and future work could directly relate dynamics in the cv-NN during movie prediction to the fine-scale spiking dynamics of the networks in the visual cortex. Finally, in the case of naturalistic movie inputs (Fig. 4), the cv-NN produces complex spatiotemporal patterns that can be mathematically described in this model as the summation of multiple traveling waves[36,37]. Future work analyzing large-scale recordings will provide opportunities for comparison between activity patterns in the visual cortex and in the cv-NN during the processing of naturalistic movie inputs.

Another potential extension of the cv-NN is to consider multiple recurrently connected layers with specializations similar to those in different regions of the visual cortex. In this work, we focused on a cv-NN with a single recurrently connected layer to understand the potential computational role of nTWs that have recently been observed in single cortical regions during visual perception in awake animals. nTWs have been observed in many visual areas, including V1[28], V2[28], V4[72], and MT[24,27,73]. Adding multiple recurrent layers in the cv-NN may provide opportunities in future work for understanding nTW dynamics across visual areas, where spatiotemporal activity patterns have recently been shown to propagate in feedforward and feedback directions in different frequency ranges[74]. Finally, closed-loop forecasts in this cv-NN are not intended to be robust to arbitrary translations or rotations of the visual scene, and adding multiple layers in the cv-NN may provide a degree of translation invariance, which is achieved in CNNs through cascading activity through multiple processing layers[75], and scale invariance, which may also be made possible through processing in multiple recurrent layers[76]. In this way, extending the cv-NN with multiple recurrent layers represents an important opportunity for understanding the organization and computational role of nTWs occurring in many cortical areas in future work.

These results provide fundamental insight into the function of horizontal recurrent connections, whose effect on the moment-by-moment computations in the visual system has remained unexplained. While there has been much interest in the function of recurrent

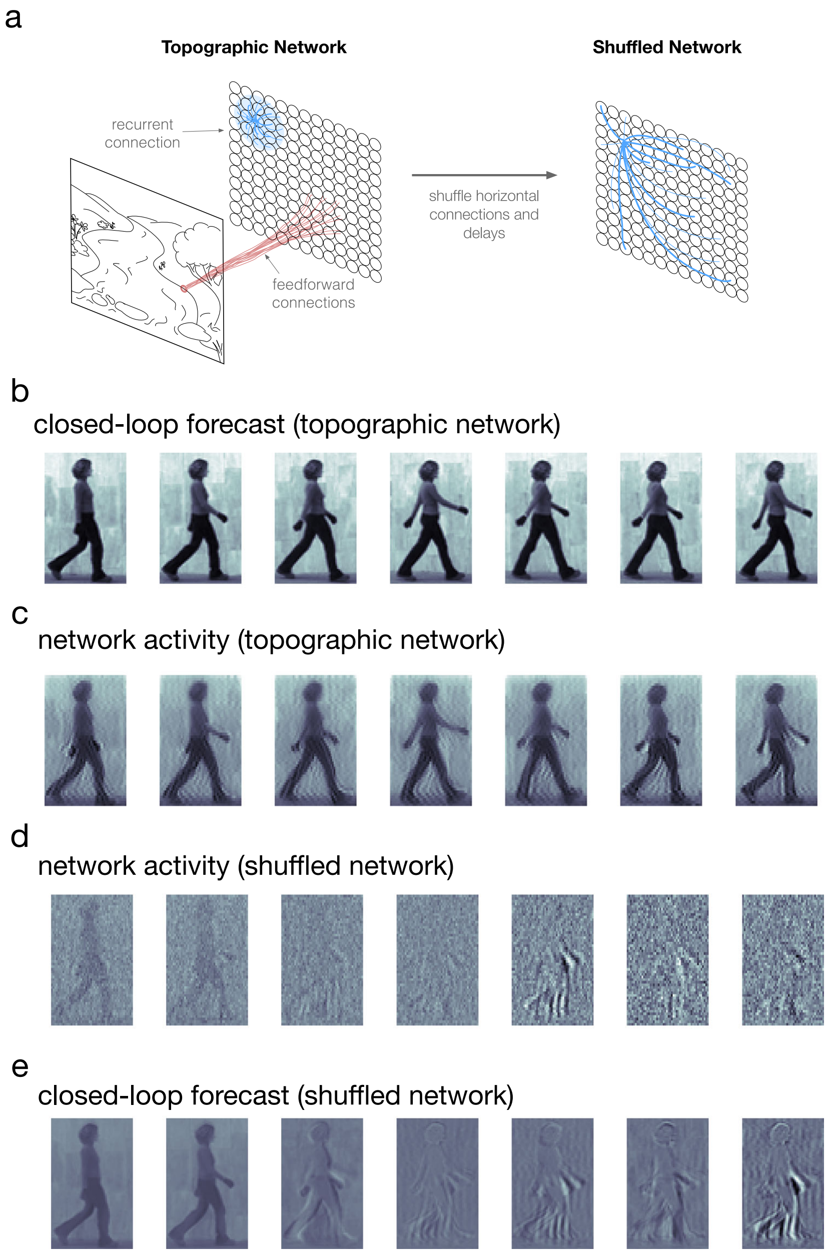
a
Topographic Network
Shuffled Network
recurrent connection
feedforward connections
shuffle horizontal connections and delays
b
closed-loop forecast (topographic network)
c
network activity (topographic network)
d
network activity (shuffled network)
e
closed-loop forecast (shuffled network)

Fig. 6 | Randomly shuffling recurrent connections eliminates nTWs and the ability to forecast. **a** Left: the topographic network model used throughout this study, featuring feedforward projections of the image input (red lines) and local distance-dependent horizontal connectivity (blue lines). There are also synaptic time delays proportional to a node pair's separation distance within the horizontal recurrent circuitry. Right: by randomizing the horizontal connection weights and time delays, the topography in the network is removed. **b** Closed-loop forecasts generated by the topographic network. **c** The network activity of the topographic network in response to frames of a natural movie input. **d** Network activity of the shuffled network. **e** Closed-loop forecasts generated by the shuffled network.

horizontal fibers in the visual cortex, for example, in explaining direction and orientation selectivity in V1[10,11] or in center-surround models of the receptive field[14,16,77], general computational roles for traveling waves generated by the massive recurrent circuitry in single cortical areas on the single-trial level remain unknown. Successful models of the visual system, including feature-based models and deep convolutional neural networks, have provided insight into how neural systems could process single image inputs but explain only a fraction of the variance in neural responses to natural sensory stimuli[18,78,79]. Importantly, it is not necessarily the case that all RNNs that can perform CLF will also exhibit nTWs; however, when networks possess the main architectural features found in the visual cortex (local connections, retinotopically ordered inputs, and communication time delays), we have demonstrated that nTWs are tightly linked to CLF. The

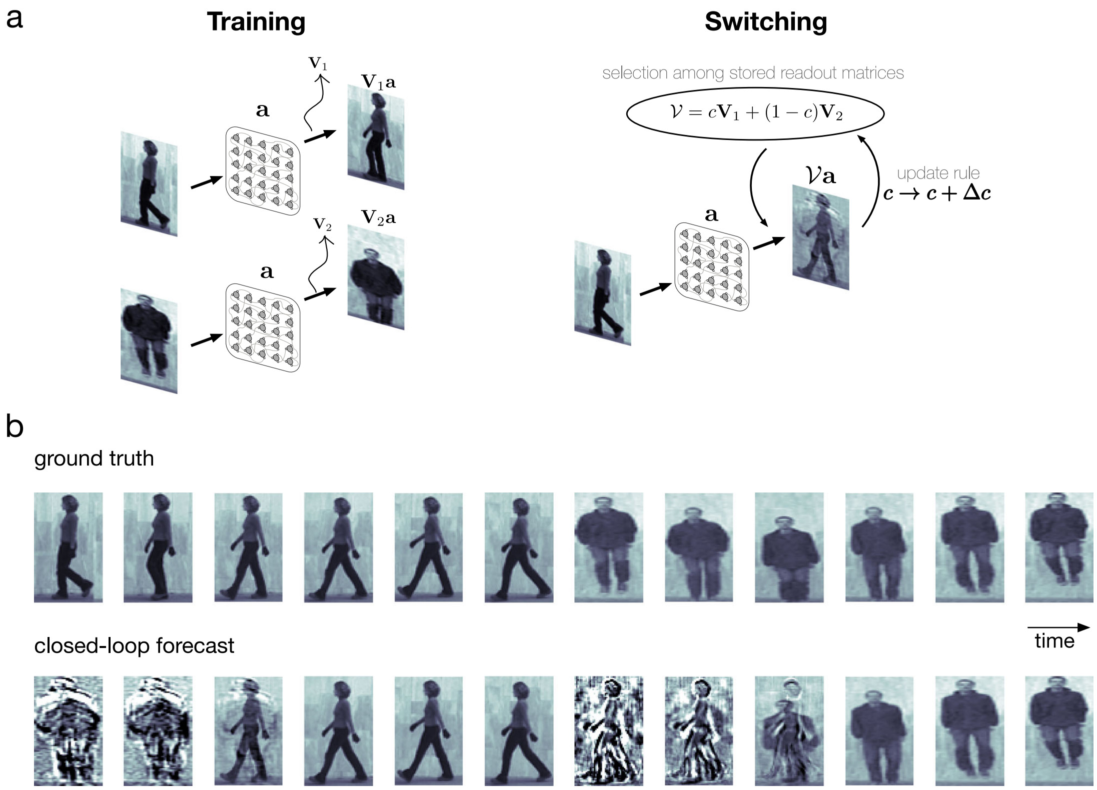

Fig. 7 | The network is capable of forecasting multiple movies without being retrained. a The recurrent network model was adapted to contain a higher-level competitive-learning process. Left: Readout matrices were learned separately for separate examples. Right: Storing the learned readout matrices in an aggregate matrix $\mathcal{V}$, the present network state drove the aggregate matrix toward either of the learned matrices via an unsupervised competitive learning rule. **b** Beginning with feeding frames from movie 1, the network takes some time to recall the learned matrix that results in an accurate closed-loop forecast. Quickly switching to a different movie, the network once again takes some time to adjust its output weights before converging to the correct ones for an accurate closed-loop forecast.

cv-NN may thus provide new opportunities for understanding how the visual system processes continuously updated, movie-like visual inputs, where information is extracted from the visual environment moment-by-moment as it comes from the eye. The sophisticated closed-loop movie forecasts produced by this network, and the fact that this closed-loop forecast process can generalize to multiple movie inputs, represent an important step in explaining the computational role of recurrent connections and traveling waves in the visual cortex.

Methods

Custom MATLAB (version R2021a) code was used for all data simulation and analysis in this study.

Network connectivity

The recurrent network is arranged on a square grid of N nodes. The network grid is treated as a discretized Euclidean plane such that the side lengths span distances of unity. Boundaries are not periodic. The recurrent weight w_{ij} from node j to node i is inversely proportional to their Euclidean distance d_{ij} so as to give local connectivity like that of the neocortical sheet. Specifically, w_{ij} is Gaussian as a function of d_{ij}:

$$w_{ij} = \alpha \exp\left[-d_{ij}^2/(2\beta^2)\right]. \tag{1}$$

The coefficient α is called the recurrent strength, and the standard deviation β is called the recurrent length. Both are free parameters. The maximum possible value of d_{ij} is $\sqrt{2}$ (corner to corner), and, for example, $\beta = 1$ means that the recurrent length equals the network side length. Further, all N^2 such weights are strictly positive, and the N-by-N matrix of such weights is symmetric ($w_{ij} = w_{ji}$). Diagonal weights (w_{ii}) are not set to zero.

Network dynamics

Network dynamics are given by a complex-valued equation. A complex number z is of the form $z = x + \mathrm{i}y$, where x is the real part, y is the imaginary part, and i is the imaginary constant defined as $\mathrm{i}^2 = -1$. Equivalently, $z = m\exp[\mathrm{i}\phi]$, where m is the modulus and ϕ is the argument. A complex number is intuitively visualized as a two-dimensional vector, where (x,y) is its Cartesian representation and (m,ϕ) is its polar representation. What distinguishes a complex number from a standard two-dimensional vector is the multiplication rule: multiplication of two complex numbers corresponds to both a scaling and a rotation in the so-called complex plane. This property makes complex-valued representations of observable quantities more concise than real-valued representations, and thus, complex numbers are a central tool in physics and engineering. From the perspective of biological vision, a complex-valued representation is useful. Since phase information is important for representing visual inputs, complex-valued models, which efficiently represent phase in the argument ϕ, are ideal. Indeed, complex-valued models of vision are widely explored[80]. Given the practical utility of artificial neural networks and deep learning (including for modeling biological neural networks), complex-valued neural networks, in which the neural activations are complex-valued, are of great interest. However, they are notoriously difficult to train, especially in a recurrent architecture[32]. We make an advance here on this front by choosing a unique dynamical equation and by exploiting the advantages of reservoir computing.

The discrete-time dynamical equation for each node i is

$$a_i[t+1] = a_i[t] + x_i[t] - \mathrm{i}\sum_{j=1}^{N} w_{ij} \exp\left\{\mathrm{i}(a_j[t-\tau_{ij}] - a_i[t])\right\}, \qquad (2)$$

$$a_i[t+1] := a_i[t+1]/|a_i[t+1]|. \qquad (3)$$

Here, $a_i[t]$ is the complex-valued activation at discrete time t, $x_i[t]$ is the feedforward input of the image stimulus to node i at discrete time t, and w_{ij} is the recurrent weight from node j to node i ("Methods"—"Network connectivity"). Further, τ_{ij} is the discrete time delay between nodes i and j, given by $\tau_{ij} = \mathrm{round}[d_{ij}/v]$ in which the Euclidean distance d_{ij} between nodes i and j ("Methods"—"Network connectivity") is scaled by the parameter v, which represents the speed of activation transmission across the network, and $\mathrm{round}[d_{ij}/v]$ rounds d_{ij}/v to the nearest integer in accord with the discrete-time dynamics. A v-value of, for example, $v = 0.1$ means the activation travels a distance of one-tenth the network side length per time step. Lastly, the modulus of $a_i[t]$ (i.e., $|a_i[t]|$) is normalized (Eq. (3)), which confines $a_i[t]$ on the complex unit circle, and thus, the phase of $a_i[t]$ contains the dynamics. We note that modulus normalization is a common operation used in complex-valued neural networks[32].

The specific form of Eq. (2) is unique compared to other complex-valued neural-network equations because it involves a pairwise node attraction $a_j[t-\tau_{ij}] - a_i[t]$. Another system with pairwise attraction is the Kuramoto model, a popular model for studying synchronization in nonlinear systems[81–83]. Our presented system has a correspondence with the Kuramoto model[84] and allows the description of the dynamics for individual realization in terms of the eigenvalues and eigenvectors of the network[36]. With the described local network connectivity and distance-dependent delays, the presented system gives rise to meaningful spatiotemporal self-organization dynamics.

The initial network state is $a_i[0] = 0 + 0i$ for all nodes, and the first several time steps contain transient activity associated with the input disrupting the initial steady state of the system. For the stimulus prediction task, this transient activity is important to the model and was used, while for the next-frame forecasting task, it is distracting to the model and was discarded.

Image read-in

At each discrete time step, a digital grayscale image is read into the network. Prior to read-in, the image is mean-subtracted and divided by its standard deviation across all its pixels (i.e., z-scored). Image read-in is accomplished with a local feedforward projection, which mimics retinotopy and preserves the spatial correlations in the image. Technically, this is a two-dimensional interpolation using the bilinear kernel common in image processing, which takes a weighted average in the nearest 2-by-2 pixel neighborhood. The projected image has $\sqrt{N}$ rows and $\sqrt{N}$ columns like the network grid, and each pixel intensity of the projected image is given by $x_i[t]$ (Eq. 2). Lastly, $x_i[t]$ is scaled according to $x_i[t] := \gamma x_i[t]$, where γ is called the input strength. In our model, γ is the fourth and final free parameter after the recurrent strength, recurrent length, and conduction speed.

Stimulus prediction task

The classification was performed using the basic perceptron. For an input vector $\mathbf{v} = \left[1\, v_1 \cdots v_N\right]^T$, where $v_1, \ldots, v_N$ are features, and a label $l \in \{0,1\}$, the goal is to find a hyperplane $\mathbf{u}^\mathrm{T}\mathbf{v} = b + u_1 v_1 + \cdots + u_N v_N = 0$, where $\mathbf{u} = \left[b\, u_1 \cdots u_N\right]^T$ is a vector containing the bias b and weights $u_1, \ldots, u_N$, that separates the data in the N-dimensional feature space according to their binary class (0 or 1). During training, with a suboptimal $\mathbf{u}$-vector and one example $\mathbf{v}$-vector, the output classification $l = \mathrm{H}(\mathbf{u}^\mathrm{T}\mathbf{v})$ is computed, where $\mathrm{H}(\cdot)$ is the Heaviside step function defined as unity for positive argument and zero otherwise. For the desired classification d (either 0 or 1), the signed distance $\Delta = d - l$ is computed, where $\Delta \in \{-1,0,1\}$. With each new example $\mathbf{v}$, the $\mathbf{u}$-vector is updated using the delta rule $\mathbf{u} := \mathbf{u} + \lambda\mathbf{v}\Delta$, where λ is the learning rate. To use the perceptron in multiclass classification, the one-versus-rest scheme is used. That is, for the set of classes $C = \left\{c_1, \ldots, c_M\right\}$, binary classification is performed separately M times. Each time i, the two classes are defined such that $c_i = 1$ and $C \backslash c_i = 0$, where "\" denotes the set difference. Then, there are M weight vectors $\mathbf{u}_1, \ldots, \mathbf{u}_\mathrm{M}$, and M inner products $f_1 = \mathbf{u}_1{}^\mathrm{T}\mathbf{v}$, ..., $f_M = \mathbf{u}_\mathrm{M}{}^\mathrm{T}\mathbf{v}$ for a given data vector $\mathbf{v}$. The multiclass classification is $\underset{c_i}{\mathrm{argmax}}\left[f_1, \ldots, f_M\right]$.

In the stimulus classification task (Fig. 1c), input frames were 50 by 50 pixels, and the network was 50 by 50 nodes. There were six frames. One of the first five frames was randomly chosen to contain the point stimulus, and the remaining frames were entirely zero intensity. The point stimulus was an isotropic two-dimensional Gaussian of standard deviation of 0.05, and the input frames are defined on the Cartesian grid $[-2,2] \times [-2,2]$. The stimulus was centered in one of four equally sized quadrants in the frame. The sequence of frames was sequentially input to the network. There are exactly twenty classes: each of the first five frames times each of the four quadrants in which the point stimulus could occur. The column vector of activations corresponding to the final (sixth) frame was used as predictor for all trials. The task was repeated 100,000 times, with the time of stimulus (1 or 2 or 3 or 4 or 5) and the location of the stimulus (quadrant 1 or 2 or 3 or 4) randomly rechosen each time.

Closed-loop forecasting

The network outputs an image of M_r rows and M_c columns of pixels—the same size as the input image—at each time step. In both examples (moving bump and natural movie), the network was 50 by 50 nodes ($N = 2500$). Recalling that $a_i[t]$ is the complex-valued activation of node i at discrete time t (Eqs. (2) and (3)), the output transformation is linear:

$$y_i[t] = \sum\nolimits_{j=1}^{N} v_{ij} a_j[t]'. \qquad (4)$$

Here, $y_i[t]$ is the ith pixel intensity of the output image, and v_{ij} is the $(i,j)^\mathrm{th}$ readout weight of the M-by-N matrix $\mathbf{V}$, where $M = M_r M_c$. The prime notation (′) indicates that the activation vector $\mathbf{a}[\mathrm{t}] = \left[a_1[t] \cdots a_N[t]\right]^T$ was mean-subtracted, which was done to avoid an intercept term during training.

The readout weights $\left\{v_{ij}\right\}$ of $\mathbf{V}$ are the only weights trained in our model, making our network a reservoir computer. Reservoir computers are recurrent neural networks that avoid the issues associated with training recurrent weights and have been shown to perform well in time series forecasting[42]. Suppose training begins at time step 1, after discarding the initial transient, and ends at time step T. Defining $\mathbf{a}[\mathrm{t}]' = \left[a_1[t]' \cdots a_N[t]'\right]^T$, the matrix of regressors is then

$$\mathbf{A} = \left[\mathbf{a}[1]' \ldots \mathbf{a}[\mathrm{T}]'\right] \qquad (5)$$

and the matrix of regressands (desired outputs) is

$$\mathbf{D} = \left[\mathbf{f}[2] \ldots \mathbf{f}[\mathrm{T}+1]\right]. \qquad (6)$$

Hence, the desired outputs are simply the set of one-step-ahead frames. Here, $\mathbf{f}[\mathrm{t}]$ is the column vectorization of the tth input image frame (before read-in) and is also mean-subtracted. Training entails ordinary least-squares linear regression between $\mathbf{A}$ and $\mathbf{D}$. Because $\mathbf{D}$ is highly underdetermined (containing far fewer frames than pixels per frame), the matrix 2-norm of **V** was simultaneously minimized during regression to reduce model bias.

Following training is *closed-loop forecasting*. At this point, the network activation has been primed by being driven with the training frames, and the readout matrix **V** has been trained. In the first time step of closed-loop forecasting, we input the corresponding video frame. Subsequently, for steps $\{t\}$, the predicted output at time step t serves as the input for time step $t+1$.

In the moving bump example (Fig. 2), the frames are 30 by 30 pixels and defined on a $[-2,2]\times[-2,2]$ Cartesian grid. A two-dimensional isotropic Gaussian of standard deviation 0.2 traced a Lissajous curve given by the parametric equations $x_c(t) = \sin(t/3)$ and $y_c(t) = \cos(t/3)$, where (x_c, y_c) is the center of the Gaussian in space and t is a continuously valued time variable[85]. The Lissajous trajectory was discretized to have 100 frames per cycle. The first cycle was discarded to omit the initial transient network activity, the network was trained on the subsequent 3 cycles, and closed-loop forecasting was performed on the 2 cycles subsequent to that.

In the natural video example (Fig. 4), a walking video from the Weizmann Human Action Dataset[86] was used, in which a person walks across the scene. We present several key examples here but note that the model successfully performs closed-loop forecasting for all movies in this dataset, where we define a successful closed-loop forecast as one in which the total structural similarity is at least 0.9 (Supplementary Fig. 2, Supplementary Table 4). Segmentation masks of the people in the videos are included with this dataset (https://www.wisdom.weizmann.ac.il/~vision/SpaceTimeActions.html). Using these masks, we cropped the frames so that the person was centered throughout the entire walk, giving frames of approximately 80 by 50 pixels. Without performing this step, our network model would fail: the training data would be independent of the closed-loop forecast data since they would occupy exclusive regions of the pixel space, and the model would not generalize to the prediction data. Such nonstationary data have been successfully taught to networks with approximate translation invariance, and translation invariance is likely used in the brain to learn such processes[87]. However, translation invariance is beyond the scope of our study. The frames were then resized to be exactly 80 by 50 pixels. Finally, each video was around 70 frames long. To get more frames without interpolation, we "bookended" each video by concatenating it with its temporal reverse sequence, where one cycle consists of the original frames followed by the bookended frames. The result is a longer video with the same spatiotemporal statistics. The first cycle was discarded to omit the initial transient network activity, the network was trained on the subsequent three cycles, and the closed-loop prediction was performed on the two cycles subsequent to that.

To measure the balance between feedforward input and recurrent interaction, we devised the *recurrence-to-input ratio*. Per Eq. (2), the input and recurrence terms are the column vectors $\mathbf{x}[t] = \left[x_1[t]\cdots x_N[t]\right]^T$ and $\mathbf{r}[t] = \left[r_1[t]\cdots r_N[t]\right]^T$, respectively, where

$$r_i[t] = -\mathrm{i}\sum_{j=1}^{N} w_{ij}\exp\left\{\mathrm{i}\left(a_j[t-\tau_{ij}] - a_i[t]\right)\right\}. \tag{7}$$

Further, let the matrices

$$\mathbf{R} = \left[\mathbf{r}[1]\ldots\mathbf{r}[T]\right] \tag{8}$$

and

$$\mathbf{X} = \left[\mathbf{x}[1]\ldots\mathbf{x}[T]\right] \tag{9}$$

be the horizontal concatenations of $\mathbf{r}[t]$ and $\mathbf{x}[t]$, respectively, over closed-loop forecast times $\{t, t+1, \ldots, t'\}$. The ratio is defined as

$$|\mathbf{R}|_F/|\mathbf{X}|_F, \tag{10}$$

where $||\mathbf{G}||_F$ denotes the Frobenius matrix norm of a matrix **G**, which is equivalent to the Euclidean vector norm of the vectorization of **G**.

Table 1 | Intervals over which model parameters were randomly searched during optimization

Parameter	Sampled interval
Recurrent strength	(0, 0.2)
Recurrent length	(0, 0.2)
Input strength	(0, 0.2)
v	(0, 0.1)

Movie switching

The network was trained on two movie inputs: one of a walking person (movie 1) and one of a jumping person (movie 1), both from the Weizmann dataset. The same recurrent matrix was used in each case–only the learned matrices ($\mathbf{V}_1$ and $\mathbf{V}_2$, respectively) differed. Let $\mathcal{V} = c\mathbf{V}_1 + (1-c)\mathbf{V}_2$, where $c \in [0,1]$. $\boldsymbol{v}$ stores both learned matrices, and the present input modulates the relative contribution of $\mathbf{V}_1$ and $\mathbf{V}_2$ using an update rule for c. The structural similarity between the input and output were computed at each time step t ($S[t]$), and the change thereof was computed at each time step as $\Delta S = S[t] - S[t-1]$. The update rule is $c := c + \Delta c$, where $\Delta c = -\eta \mathrm{sgn}[\Delta S]$ and η is the learning rate, set to 0.1. Depending on which movie (movie 1 or movie 2) drives the network, c tends toward 1 or 0, respectively. Once this happens, this driving input is removed and closed-loop forecasting commences as described. Switching entails instantaneously transitioning from closed-loop forecasting of one movie to driving the network with the frames of another movie. c then updates as described and is followed by closed-loop forecasting again.

Parameter optimization

The random-search algorithm was used to optimize parameters for closed-loop forecasting. Within specified bounds, each parameter was randomly sampled, giving a point in the parameter space. The parameter space was randomly sampled in this way many times, and each time, the structural similarity index was computed as the performance index. The bounds within which the parameters were sampled are given in Table 1.

Reporting summary

Further information on research design is available in the Nature Portfolio Reporting Summary linked to this article.

Data availability

The point stimulus and moving bump stimulus data generated in this study can be generated from the code available at this study's GitHub repository (https://github.com/mullerlab/benignoEAwavecomp). The raw data of the natural movies used in this study are provided by Lena Gorelick, Moshe Blank, and Eli Shectman of the Weizmann Institute of Science, available at https://www.wisdom.weizmann.ac.il/~vision/SpaceTimeActions.html and this study's GitHub repository. Source data are provided with this paper.

Code availability

All codes associated with this study are available at https://github.com/mullerlab/benignoEAwavecomp[88].

References

1. Peters, A. & Payne, B. R. Numerical relationships between geniculocortical afferents and pyramidal cell modules in cat primary visual cortex. *Cereb. Cortex* **3**, 69–78 (1993).
2. Latawiec, D., Martin, K. A. & Meskenaite, V. Termination of the geniculocortical projection in the striate cortex of macaque monkey: a quantitative immunoelectron microscopic study. *J. Comp. Neurol.* **419**, 306–319 (2000).
3. Da Costa, N. M. & Martin, K. A. C. The proportion of synapses formed by the axons of the lateral geniculate nucleus in layer 4 of area 17 of the cat. *J. Comp. Neurol.* **516**, 264–276 (2009).
4. Markov, N. T. et al. Weight consistency specifies regularities of macaque cortical networks. *Cereb. Cortex* **21**, 1254–1272 (2011).
5. Bruno, R. M. & Sakmann, B. Cortex is driven by weak but synchronously active thalamocortical synapses. *Science* **312**, 1622–1627 (2006).
6. Swindale, N. V. Visual map. *Scholarpedia J.* **3**, 4607 (2008).
7. Hubel, D. H. & Wiesel, T. N. Receptive fields of single neurones in the cat's striate cortex. *J. Physiol.* **148**, 574–591 (1959).
8. Riesenhuber, M. & Poggio, T. Hierarchical models of object recognition in cortex. *Nat. Neurosci.* **2**, 1019–1025 (1999).
9. Angelucci, A. et al. Circuits for local and global signal integration in primary visual cortex. *J. Neurosci.* **22**, 8633–8646 (2002).
10. Douglas, R. J., Koch, C., Mahowald, M., Martin, K. A. & Suarez, H. H. Recurrent excitation in neocortical circuits. *Science* **269**, 981–985 (1995).
11. Sompolinsky, H. & Shapley, R. New perspectives on the mechanisms for orientation selectivity. *Curr. Opin. Neurobiol.* **7**, 514–522 (1997).
12. Blakemore, C. & Tobin, E. A. Lateral inhibition between orientation detectors in the cat's visual cortex. *Exp. Brain Res.* **15**, 439–440 (1972).
13. Allman, J., Miezin, F. & McGuinness, E. Stimulus specific responses from beyond the classical receptive field: neurophysiological mechanisms for local-global comparisons in visual neurons. *Annu. Rev. Neurosci.* **8**, 407–430 (1985).
14. Field, D. J., Hayes, A. & Hess, R. F. Contour integration by the human visual system: evidence for a local 'association field'. *Vis. Res.* **33**, 173–193 (1993).
15. Gilbert, C. D. Adult cortical dynamics. *Physiol. Rev.* **78**, 467–485 (1998).
16. Albright, T. D. & Stoner, G. R. Contextual influences on visual processing. *Annu. Rev. Neurosci.* **25**, 339–379 (2002).
17. Kietzmann, T. C. et al. Recurrence is required to capture the representational dynamics of the human visual system. *Proc. Natl Acad. Sci. USA* **116**, 21854–21863 (2019).
18. Kar, K., Kubilius, J., Schmidt, K., Issa, E. B. & DiCarlo, J. J. Evidence that recurrent circuits are critical to the ventral stream's execution of core object recognition behavior. *Nat. Neurosci.* **22**, 974–983 (2019).
19. Bringuier, V., Chavane, F., Glaeser, L. & Frégnac, Y. Horizontal propagation of visual activity in the synaptic integration field of area 17 neurons. *Science* **283**, 695–699 (1999).
20. Roland, P. E. et al. Cortical feedback depolarization waves: a mechanism of top-down influence on early visual areas. *Proc. Natl Acad. Sci. USA* **103**, 12586–12591 (2006).
21. Xu, W., Huang, X., Takagaki, K. & Wu, J.-Y. Compression and reflection of visually evoked cortical waves. *Neuron* **55**, 119–129 (2007).
22. Nauhaus, I., Busse, L., Carandini, M. & Ringach, D. L. Stimulus contrast modulates functional connectivity in visual cortex. *Nat. Neurosci.* **12**, 70–76 (2009).
23. Reimer, A., Hubka, P., Engel, A. K. & Kral, A. Fast propagating waves within the rodent auditory cortex. *Cereb. Cortex* **21**, 166–177 (2011).
24. Townsend, R. G. et al. Emergence of complex wave patterns in primate cerebral cortex. *J. Neurosci.* **35**, 4657–4662 (2015).
25. Slovin, H., Arieli, A., Hildesheim, R. & Grinvald, A. Long-term voltage-sensitive dye imaging reveals cortical dynamics in behaving monkeys. *J. Neurophysiol.* **88**, 3421–3438 (2002).
26. Sato, T. K., Nauhaus, I. & Carandini, M. Traveling waves in visual cortex. *Neuron* **75**, 218–229 (2012).
27. Davis, Z. W., Muller, L., Martinez-Trujillo, J., Sejnowski, T. & Reynolds, J. H. Spontaneous travelling cortical waves gate perception in behaving primates. *Nature* **587**, 432–436 (2020).
28. Muller, L., Reynaud, A., Chavane, F. & Destexhe, A. The stimulus-evoked population response in visual cortex of awake monkey is a propagating wave. *Nat. Commun.* **5**, 3675 (2014).
29. Davis, Z. et al. Spontaneous traveling waves naturally emerge from horizontal fiber time delays and travel through locally asynchronous-irregular states. *Nat. Commun.* **12**, 6057 (2021).
30. Takahashi, K. et al. Large-scale spatiotemporal spike patterning consistent with wave propagation in motor cortex. *Nat. Commun.* **6**, 7169 (2015).
31. Schaffer, E. S., Ostojic, S. & Abbott, L. F. A complex-valued firing-rate model that approximates the dynamics of spiking networks. *PLoS Comput. Biol.* **9**, e1003301 (2013).
32. Bassey, J., Qian, L. & Li, X. A survey of complex-valued neural networks. Preprint at https://arxiv.org/abs/2101.12249 (2021).
33. Trabelsi, C. et al. Deep complex networks. *International Conference on Learning Representations* (2018).
34. Heeger, D. J. & Mackey, W. E. Oscillatory recurrent gated neural integrator circuits (ORGaNICs), a unifying theoretical framework for neural dynamics. *Proc. Natl Acad. Sci. USA* **116**, 22783–22794 (2019).
35. Krizhevsky, A., Sutskever, I. & Hinton, G. E. ImageNet classification with deep convolutional neural networks. *Commun. ACM* **60**, 84–90 (2017).
36. Budzinski, R. C. et al. Geometry unites synchrony, chimeras, and waves in nonlinear oscillator networks. *Chaos* **32**, 031104 (2022).
37. Muller, L., Chavane, F., Reynolds, J. & Sejnowski, T. J. Cortical travelling waves: mechanisms and computational principles. *Nat. Rev. Neurosci.* **19**, 255–268 (2018).
38. Hellwig, B. A quantitative analysis of the local connectivity between pyramidal neurons in layers 2/3 of the rat visual cortex. *Biol. Cybern.* **82**, 111–121 (2000).
39. Binzegger, T., Douglas, R. J. & Martin, K. A. C. A quantitative map of the circuit of cat primary visual cortex. *J. Neurosci.* **24**, 8441–8453 (2004).
40. Girard, P., Hupé, J. M. & Bullier, J. Feedforward and feedback connections between areas V1 and V2 of the monkey have similar rapid conduction velocities. *J. Neurophysiol.* **85**, 1328–1331 (2001).
41. Elman, J. L. Finding structure in time. *Cogn. Sci.* **14**, 179–211 (1990).
42. Jaeger, H. & Haas, H. Harnessing nonlinearity: predicting chaotic systems and saving energy in wireless communication. *Science* **304**, 78–80 (2004).
43. Pathak, J., Lu, Z., Hunt, B. R., Girvan, M. & Ott, E. Using machine learning to replicate chaotic attractors and calculate Lyapunov exponents from data. *Chaos* **27**, 121102 (2017).
44. Vlachas, P. R. et al. Backpropagation algorithms and Reservoir Computing in Recurrent Neural Networks for the forecasting of complex spatiotemporal dynamics. *Neural Netw.* **126**, 191–217 (2020).
45. Pathak, J., Hunt, B., Girvan, M., Lu, Z. & Ott, E. Model-free prediction of large spatiotemporally chaotic systems from data: a reservoir computing approach. *Phys. Rev. Lett.* **120**, 024102 (2018).
46. Tang, Y., Kurths, J., Lin, W., Ott, E. & Kocarev, L. Introduction to focus issue: when machine learning meets complex systems: networks, chaos, and nonlinear dynamics. *Chaos* **30**, 063151 (2020).

47. Mathieu, M., Couprie, C. & LeCun, Y. Deep multi-scale video prediction beyond mean square error. *International Conference on Learning Representations* (2016).
48. Villegas, R., Yang, J., Hong, S., Lin, X. & Lee, H. Decomposing motion and content for natural video sequence prediction. *International Conference on Learning Representations* (2017).
49. Desai, P. et al. Next frame prediction using ConvLSTM. *J. Phys. Conf. Ser.* **2161**, 012024 (2022).
50. Michalski, V., Memisevic, R. & Konda, K. Modeling deep temporal dependencies with recurrent grammar cells. *Advances in Neural Information Processing Systems* **27**, (2014)
51. Lotter, W., Kreiman, G. & Cox, D. Deep predictive coding networks for video prediction and unsupervised learning. *International Conference on Learning Representations* (2017).
52. Choi, M. & Tani, J. Predictive coding for dynamic visual processing: development of functional hierarchy in a multiple spatiotemporal scales RNN model. *Neural Comput.* **30**, 237–270 (2018).
53. Kwon, Y.-H. & Park, M.-G. Predicting future frames using retrospective cycle GAN. In *Proc. 2019 IEEE/CVF Conference on Computer Vision and Pattern Recognition (CVPR)*, 1811–1820 (IEEE, 2019).
54. Shouno, O. Photo-realistic video prediction on natural videos of largely changing frames. Preprint at https://arxiv.org/abs/2003.08635 (2020).
55. Yu, W., Lu, Y., Easterbrook, S. & Fidler, S. Efficient and information-preserving future frame prediction and beyond. In *Proc. 2020 International Conference on Learning Representations*. https://openreview.net/pdf?id=F4e26c-K1DM (ICLR, 2020).
56. Kasaraneni, S. H. Autoencoding video latents for adversarial video generation. Preprint at https://arxiv.org/abs/2201.06888 (2022).
57. Ranzato, M. et al. Video (language) modeling: a baseline for generative models of natural videos. Preprint at https://arxiv.org/abs/1412.6604 (2014).
58. Hou, R., Chang, H., Ma, B. & Chen, X. Video prediction with bidirectional constraint network. In *Proc. 2019 14th IEEE International Conference on Automatic Face & Gesture Recognition (FG 2019)*, 1–8 (2019).
59. Wang, Z., Bovik, A. C., Sheikh, H. R. & Simoncelli, E. P. Image quality assessment: from error visibility to structural similarity. *IEEE Trans. Image Process.* **13**, 600–612 (2004).
60. Ferster, D., Chung, S. & Wheat, H. Orientation selectivity of thalamic input to simple cells of cat visual cortex. *Nature* **380**, 249–252 (1996).
61. Ferster, D. & Miller, K. D. Neural mechanisms of orientation selectivity in the visual cortex. *Annu. Rev. Neurosci.* **23**, 441–471 (2000).
62. Stettler, D. D., Das, A., Bennett, J. & Gilbert, C. D. Lateral connectivity and contextual interactions in macaque primary visual cortex. *Neuron* **36**, 739–750 (2002).
63. Moshe, B., Lena, G., Eli, S., Michal, I. & Ronen, B. Actions as space-time shapes. in *Proc. Tenth IEEE International Conference on Computer Vision, Beijing, China*, 17–20 (2005).
64. Thorpe, S., Fize, D. & Marlot, C. Speed of processing in the human visual system. *Nature* **381**, 520–522 (1996).
65. McBeath, M. K. The rising fastball: baseball's impossible pitch. *Perception* **19**, 545–552 (1990).
66. Chelazzi, L., Miller, E. K., Duncan, J. & Desimone, R. A neural basis for visual search in inferior temporal cortex. *Nature* **363**, 345–347 (1993).
67. Wheeler, M. E., Petersen, S. E. & Buckner, R. L. Memory's echo: vivid remembering reactivates sensory-specific cortex. *Proc. Natl Acad. Sci. USA* **97**, 11125–11129 (2000).
68. Horner, A. J., Bisby, J. A., Bush, D., Lin, W.-J. & Burgess, N. Evidence for holistic episodic recollection via hippocampal pattern completion. *Nat. Commun.* **6**, 7462 (2015).
69. Vanni, S., Hokkanen, H., Werner, F. & Angelucci, A. Anatomy and physiology of macaque visual cortical areas V1, V2, and V5/MT: bases for biologically realistic models. *Cereb. Cortex* **30**, 3483–3517 (2020).
70. Benvenuti, G. et al. Anticipatory responses along motion trajectories in awake monkey area V1. Preprint at *bioRxiv* https://doi.org/10.1101/2020.03.26.010017 (2020).
71. Montbrió, E., Pazó, D. & Roxin, A. Macroscopic description for networks of spiking neurons. *Phys. Rev. X* **5**, 021028 (2015).
72. Zanos, T. P., Mineault, P. J., Nasiotis, K. T., Guitton, D. & Pack, C. C. A sensorimotor role for traveling waves in primate visual cortex. *Neuron* **85**, 615–627 (2015).
73. Townsend, R., Solomon, S. S., Martin, P. R., Solomon, S. G. & Gong, P. Visual motion discrimination by propagating patterns in primate cerebral cortex. *J. Neurosci*. **37**, 10074–10084 (2017).
74. Aggarwal, A. et al. Visual evoked feedforward–feedback traveling waves organize neural activity across the cortical hierarchy in mice. *Nat. Commun.* **13**, 1–16 (2022).
75. LeCun, Y., Bengio, Y. & Hinton, G. Deep learning. *Nature* **521**, 436–444 (2015).
76. Xu, Y., Xiao, T., Zhang, J., Yang, K. & Zhang, Z. Scale-invariant convolutional neural networks. Preprint at https://arxiv.org/abs/1411.6369 (2014).
77. Hess, R. F. & Dakin, S. C. Contour integration in the peripheral field. *Vis. Res.* **39**, 947–959 (1999).
78. Olshausen, B. A. How close are we to understanding V1? *Neural Comput.* **17**, 1665–1699 (2005).
79. Schrimpf, M. et al. Brain-score: which artificial neural network for object recognition is most brain-like? Preprint at *bioRxiv* https://doi.org/10.1101/407007 (2020).
80. Cadieu, C. F. & Olshausen, B. A. Learning intermediate-level representations of form and motion from natural movies. *Neural Comput.* **24**, 827–866 (2012).
81. Acebrón, J. A., Bonilla, L. L., Pérez Vicente, C. J., Ritort, F. & Spigler, R. The Kuramoto model: a simple paradigm for synchronization phenomena. *Rev. Mod. Phys.* **77**, 137–185 (2005).
82. Rodrigues, F. A., Peron, T. K. D. M., Ji, P. & Kurths, J. The Kuramoto model in complex networks. *Phys. Rep.* **610**, 1–98 (2016).
83. Breakspear, M., Heitmann, S. & Daffertshofer, A. Generative models of cortical oscillations: neurobiological implications of the Kuramoto model. *Front. Hum. Neurosci.* **4**, 190 (2010).
84. Muller, L., Mináč, J. & Nguyen, T. T. Algebraic approach to the Kuramoto model. *Phys. Rev. E* **104**, L022201 (2021).
85. Heim, N. & Avery, J. E. Adaptive anomaly detection in chaotic time series with a spatially aware echo state network. Preprint at https://arxiv.org/abs/1909.01709 (2019).
86. Gorelick, L., Blank, M., Shechtman, E., Irani, M. & Basri, R. Actions as space-time shapes. *IEEE Trans. Pattern Anal. Mach. Intell.* **29**, 2247–2253 (2007).
87. Anselmi, F. et al. Unsupervised learning of invariant representations. *Theor. Comput. Sci.* **633**, 112–121 (2016).
88. Benigno, G. B. et al. Waves traveling over a map of visual space can ignite short-term predictions of sensory input. mullerlab/benignoEAwavecomp: v1.0.0. Zenodo https://doi.org/10.5281/zenodo.7863700 (2023).

Acknowledgements

This work was supported by the Canadian Institute for Health Research (L.M.) and NSF (NeuroNex Grant No. 2015276) (L.M.), NIH Grant R01-EY028723 (J.H.R.), BrainsCAN at Western University through the Canada First Research Excellence Fund (CFREF) (L.M.), the Fiona and Sanjay Jha Chair in Neuroscience (J.H.R.), Compute Ontario (computeontario.ca) (L.M.), Digital Research Alliance of Canada (https://alliancecan.ca/en) (L.M.), SPIRITS 2020 of Kyoto University (L.M.), and the Western Academy for Advanced Research (L.M.). R.C.B. gratefully acknowledges the Western Institute for Neuroscience Clinical

Research Postdoctoral Fellowship. G.B.B. gratefully acknowledges the Canadian Open Neuroscience Platform (Graduate Scholarship), the Vector Institute (Postgraduate Affiliate), and the National Sciences and Engineering Research Council of Canada (Canada Graduate Scholarship—Doctoral). The authors thank Alex Busch for her help with illustrations.

Author contributions

Conceptualization: G.B.B., L.M.; data curation: G.B.B.; formal analysis: G.B.B., L.M.; funding acquisition: J.H.R., L.M.; investigation: G.B.B., L.M.; methodology: G.B.B., R.C.B., Z.W.D., J.H.R., L.M.; supervision: J.H.R., L.M.; visualization: G.B.B.; writing—original draft: G.B.B., L.M.; writing—review and editing: G.B.B., R.C.B., Z.W.D., J.H.R., L.M.

Competing interests

The authors declare no competing interests.

Additional information

Supplementary information The online version contains supplementary material available at https://doi.org/10.1038/s41467-023-39076-2.

Correspondence and requests for materials should be addressed to Lyle Muller.

Peer review information *Nature Communications* thanks Alex Proekt and the other anonymous reviewers for their contribution to the peer review of this work.

Reprints and permissions information is available at http://www.nature.com/reprints

Publisher's note Springer Nature remains neutral with regard to jurisdictional claims in published maps and institutional affiliations.

Open Access This article is licensed under a Creative Commons Attribution 4.0 International License, which permits use, sharing, adaptation, distribution and reproduction in any medium or format, as long as you give appropriate credit to the original author(s) and the source, provide a link to the Creative Commons license, and indicate if changes were made. The images or other third party material in this article are included in the article's Creative Commons license, unless indicated otherwise in a credit line to the material. If material is not included in the article's Creative Commons license and your intended use is not permitted by statutory regulation or exceeds the permitted use, you will need to obtain permission directly from the copyright holder. To view a copy of this license, visit http://creativecommons.org/licenses/by/4.0/.

© The Author(s) 2023

Supplementary Information for "Waves traveling over a map of visual space can ignite short-term predictions of sensory input"

Gabriel B. Benigno,[1, 2, 3] Roberto C. Budzinski,[1, 2, 3] Zachary Davis,[4] John Reynolds,[4] and Lyle Muller[1, 2, 3]

[1] *Department of Mathematics, Western University, London, ON, Canada*
[2] *Western Institute for Neuroscience, Western University, London, ON, Canada*
[3] *Western Academy for Advanced Research, Western University, London, ON, Canada*
[4] *The Salk Institute for Biological Studies, La Jolla, CA, USA*

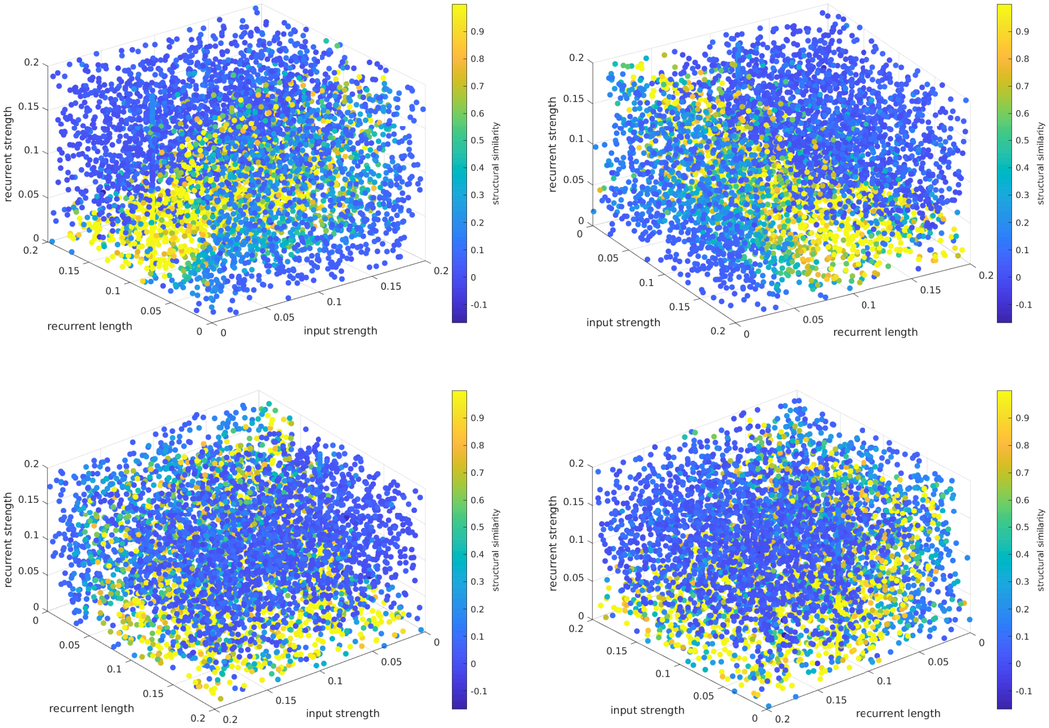

Supplementary Figure 1. Distribution of the total structural similarity (structural similarity of the entire movie) for the moving bump example (colour scale) throughout the parameter space (axes of recurrent strength, recurrent length, and input strength). Four views of the same parameter space shown. Source data are provided as a Source Data file.

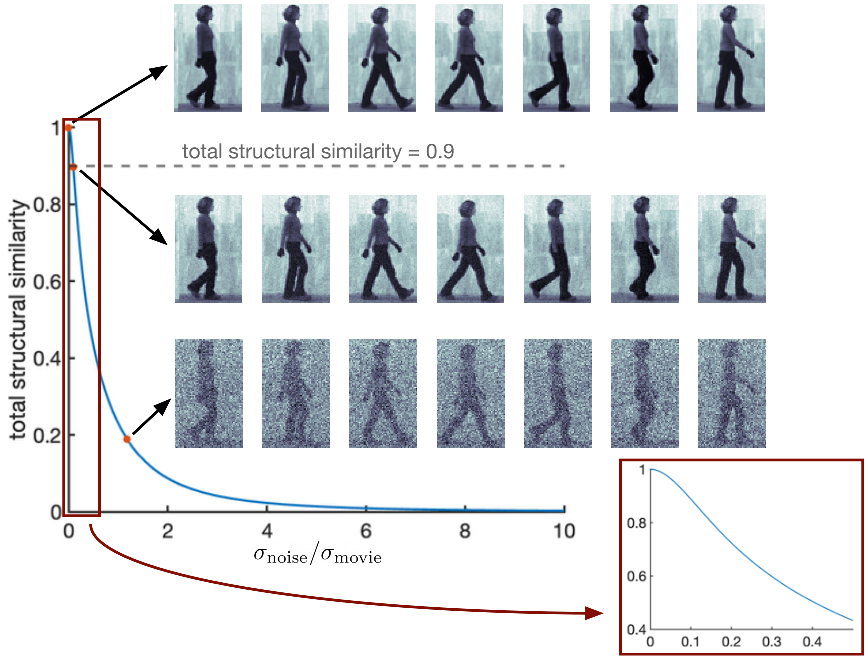

Supplementary Figure 2. Total structural similarity provides a sensitive measure of movie similarity. The total structural similarity between an example movie of a walking subject and the same movie with added Gaussian noise demonstrates how this measure captures similarity between movies. With progressively higher noise amplitude ($\sigma_{\text{noise}}/\sigma_{\text{movie}}$ in line plot), the total structural similarity rapidly decreases from 1 (no noise) to low values. Example image sequences are provided at different noise amplitudes (red dots on blue line) to illustrate the movie sequence at varying levels of added noise. Within a range of small noise amplitudes (inset), the total structural similarity drops rapidly from 1 to 0.4. Source data are provided as a Source Data file

Total SSIM	
phase-unshuffled	phase-shuffled
1.00	0.0126
	0.0143
	0.0086
	0.0125
	0.0095
	0.0109
	0.0211
	0.0018
	0.0069

Supplementary Table 1. Total structural similarity (SSIM) between ground-truth natural video and closed-loop forecast frames for regular case (left column) and case where each frame of the video is phase-shuffled using the discrete Fourier transform (right column). Shuffling was performed 10 times (mean ± standard deviation = 0.0169 ± 0.0050).

input	reservoir size	video frame size (pixels)	# of training frames	training time (s)	closed-loop forecast performance (total SSIM)
moving bump	50x50	30x30	300	26.48	1.00
walking person	50x50	80x50	432	36.07	1.00

Supplementary Table 2. Training specifications for both forecasting examples for the cases of optimal hyperparameters. Total SSIM, total structual similarity.

total SSIM	
unshuffled	shuffled
0.9996	0.0186
0.9978	0.3692
0.9998	0.4609
0.9993	0.5982
0.9999	0.0126
0.9989	0.1804
0.9982	0.0091
0.9998	0.4609
0.9992	0.0653
0.9998	0.4553

Supplementary Table 3. Left column: a random sample of ten well performing (total SSIM > 0.99) network implementations (mean ± standard deviation = 0.9988 ± 0.0014). Right column: topographically randomized versions of the network implementations, in which the recurrent weights and time delays were shuffled (mean ± standard deviation = 0.2566 ± 0.2186). Total SSIM, total structural similarity.

Movie	$\mathrm{SSIM}_{\mathrm{train}}$	$\mathrm{SSIM}_{\mathrm{test}}$
Shahar walk	1.00	0.9999999254
Moshe walk	1.00	0.9999995867
Lyova walk	1.00	0.9999999899
Lena walk1	1.00	0.9999563115
Lena walk2	1.00	0.9999995154
Ira walk	1.00	0.9999872030
Ido walk	1.00	0.9999999976
Eli walk	1.00	0.9999993216
Denis walk	1.00	0.9999968517
Daria walk	1.00	0.9999962703

Supplementary Table 4. Results of 100 trials of the random-search optimization method performed on the free parameters for each walking movie in the Weizmann dataset, in terms of the total structural similarity (SSIM)-values during training and testing ($\mathrm{SSIM}_{\mathrm{train}}$ and $\mathrm{SSIM}_{\mathrm{test}}$, respectively) of the best trial for each movie.

5 | Discussion

In this thesis, we explored the origins and roles of traveling waves of neural activity in the visual cortex. In Work 1 (Chapter 2), a large-scale simulation of a spiking neural network revealed the importance of distance-dependent time delays in shaping the spatiotemporal dynamics into waves across the entire network. Importantly these waves agreed with those observed in vivo and provide a possible mechanism of gain modulation that complements the observed effect in vivo of the waves modulating perceptual sensitivity. In Work 2 (Chapter 3), we analyzed a nonlinear oscillator model of synchronization, also containing distance-dependent delays. This approach provided analytical insight into the emergent traveling waves in the system as individual eigenmodes contributing individual waves. In Work 3 (Chapter 4), we used the model from Work 2 in a machine-learning framework, and found that the emergent traveling waves are helpful in forecasting spatiotemporally structured natural movie inputs.

5.1 Distance-dependent delays induce spontaneous and evoked traveling waves

Work 1 expanded on and sought to provide a mechanism for the recent experimental result of spontaneous activity in cortex modulating online sensory processing, which impacted perceptual sensitivity. These spatiotemporal dynamics are asynchronous throughout the cortical area and are not stochastic. Instead, they are frequently shaped as traveling waves. This spiking model, which is topographic and conductance-based, revealed the sufficiency of distance-dependent conduction delays in describing the in-vivo results from Davis et al., 2020. The waves are spontaneous and intrinsic in the sense that there is no forcing stimulus. Moreover, their presence in the parameter space of excitatory and inhibitory conductances (that generate asynchronous-irregular activity) is ubiquitous. These waves agreed with the cortical recordings of awake, behaving marmosets, with wave speeds that matched the speed of conduction of unmyelinated axonal horizontal fibres in layer 2/3.

Cortical regions possess horizontal axonal fibres reaching between hundreds of microns and several millimeters (Angelucci et al., 2002; Stettler et al., 2002), and the associated time delays range from several to tens of milliseconds (Bringuier et al., 1999; Girard et al., 2001). Previous spiking models studied networks occupying 100 µm to 1 mm—smaller scales than the ones considered in Work 1 (up to 6 mm on a side). Furthermore, some studies posited that the spatiotemporal dynamics were negligibly affected by the distance-dependent delays in the system (Mehring et al., 2003). On the other hand, many other studies have found time delays to meaningfully impact spatiotemporal dynamics (Crook et al., 1997; Golomb and Ermentrout, 1999, 2000; Kriener et al., 2009; Kriener et al., 2014; Osan and Ermentrout, 2001; Roxin et al., 2005, 2006; Senk et al., 2020). Furthermore, there are previous topographic models that lack distance-dependent delays that have been shown to produce traveling waves (Gong and van Leeuwen, 2009; Huang et al., 2019; Keane and Gong, 2015). However, the spiking activity associated with the waves from these network models are highly correlated in space. Our large-scale spiking network model in Work 1 provides evidence that distance-dependent delays in networks on the scale of entire visual cortical areas are a fundamental substrate of spatiotemporal dynamics organized as spontaneous traveling waves. Lastly, in this model, the local network dynamics remain asynchronous despite the large-scale presence of the traveling waves. Thus, these spontaneous traveling waves are compatible with the asynchronous-irregular regime. Perhaps more fundamentally, they emerge from the topographic connectivity and distance-dependent delays, which respect the physical structure of visual cortex.

Work 2 (Chapter 3) abstracted the important structural ingredients of the network model of Work 1 (i.e., local distance-dependent connectivity and distance-dependent time delays) into a ring network of coupled oscillators given by the Kuramoto model. We presented an analytical approach to the spatiotemporal dynamics of this network. Based on a complex-valued formulation of the Kuramoto model introduced by Muller et al., 2021 and Budzinski et al., 2022, this framework allowed us to use a delay operator. Considering a matrix representing both the network connectivity and the delays, the effect of time delays in the system could then be understood as a rotation of the eigenvalues in the complex plane.

In Work 3 (Chapter 4), a model based on that of Work 2 was used to ask what computations could be done by such a biologically constrained system known to exhibit traveling-wave dynamics. In this case, however, the system received inputs of natural movie frames, and was tasked with forecasting subsequent frames. The wave activity in this network is then evoked (rather than spontaneous as in Works 1 and 2), reminiscent of a result observed in macaque V1 by Muller et al., 2014.

Taken together, these results demonstrate the importance of distance-dependent time delays in neural systems, in which traveling waves emerge that match those observed in vivo.

5.2 Spontaneous cortical traveling waves are sparse and may be a dynamic mechanism of gain modulation

In the spiking network model of Work 1, neuronal participation in the emergent traveling waves was sparse at cortically realistic values of neuronal and synaptic density. This sparseness of spiking enabled the waves to exist simultaneously with the asynchronous-irregular spiking regime, which is a hallmark of spontaneous dynamics in cortex and also has established computational benefits (Destexhe and Contreras, 2006; Destexhe et al., 2003; Renart et al., 2010; Zerlaut and Destexhe, 2017). These waves are then considered sparse with respect to the underlying spiking activity, and modulate responses to external stimuli (i.e., stimuli evoke responses modulated by the phase of the wave), consistent with the in-vivo observation of Davis et al., 2020.

The spatiotemporal dynamics of these sparse waves is only salient for large enough networks (starting at hundreds of thousands of neurons in patches of several millimeters per side). Although there are many synapses per neuron, the number of neurons in the network is large, making the connectivity sparse. Such networks produce self-sustained asynchronous-irregular dynamics thanks to the high synaptic density per neuron, which brings the synaptic conductance values nearly in line with those observed in vivo (Kumar, Rotter, et al., 2008; Kumar, Schrader, et al., 2008). In smaller networks possessing larger conductances, there is strong and biologically implausible linking of spikes with changes in synapse-level potentials, which causes what is known as *shunting* of inputs (Morrison et al., 2007). We exemplified this effect by simulating a smaller network that produced dense waves.

Lastly, we tested whether the instantaneous state of dynamics in the network responsible for sparse waves was capable of affecting the network's excitability in response to driving stimuli. Such studies have previously been performed in non-wave-generating networks for an effect known as gain modulation (Chance et al., 2002). By stimulating a small pool in the network, we showed that when the stimulus was aligned with the depolarized phase of the wave, the evoked spiking response (and thus gain modulation) was stronger than when aligned with the hyperpolarized phase, in agreement with the wave phase-dependent modulation of evoked firing rates in marmoset area MT observed in vivo by Davis et al., 2020. As a control, a smaller-scale network that resulted in dense waves was also subjected to this stimulation, and there was little phase-dependent gain modulation. These effects indicate that the propagation of the wave front of a sparse wave shifts the local excitatory-inhibitory balance that in turn modifies the local network excitability.

5.3 Evoked traveling waves may enable short-term prediction in individual visual cortical areas

In Work 3, we used the model of Work 2 (containing local spatial connectivity and distance-dependent time delays) to understand whether traveling waves generated by horizontal connections in visual cortex may play a computational role in processing natural visual inputs. With an appended learning rule, the model learned to forecast video frames of one of several different naturalistic movies at a time, such as that of a moving dot stimulus or a walking person. With the adequate amount of drive in the network due to recurrent inputs, learning successfully resulted in forecasts that extended many frames into the future, even after cutting off ground-truth inputs and instead feeding predictions as subsequent inputs in the so-called closed-loop forecasting paradigm.

In a simple spatiotemporal classification task, the network exhibited radiating traveling waves that enabled successful classification, and, importantly, in the case of forecasting, the network activity revealed evoked traveling waves in response to the input frames. For example, a moving centre-surround-type activity pattern was visible when the network learned to forecast the moving dot, and a stream of waves propagated across the network on top of the imprinted walking person. As the precise computational roles of such evoked traveling waves continue to be studied, the result in Work 2 shows that traveling waves in the present system are the superposition of individual simpler traveling waves given by the eigenmodes of the system. Hence, one can imagine these different wave components given by the eigenmodes as representing different past experiences, where the network becomes dominated by the set of modes that most closely matches the present input. In this way, the waves could serve as dynamical phenomena that enable short-term predictions based on the momentary spatiotemporal input. In a preliminary demonstration, the network was trained on two different naturalistic movies, and we found that the network could successfully switch forecasts between these two movies using a simple competitive mechanism.

5.4 Conclusion

Overall, using simulations, mathematical analyses, and machine learning, the results in Works 1, 2, and 3 contribute to a deeper understanding of spatiotemporal dynamics in mesoscopic neural systems, where the effects of heterogeneous time delays and distance-dependent connectivity are meaningful, and emergent activity patterns like traveling waves influence the computations that the network can perform. Subsequent experimental and theoretical work will help to further elucidate the mechanics and functions of this interesting regime of cortical dynamics.

Bibliography

Angelucci, A., Levitt, J. B., Walton, E. J., Hupe, J.-M., Bullier, J., & Lund, J. S. (2002). Circuits for local and global signal integration in primary visual cortex. *Journal of Neuroscience*, *22*(19), 8633–8646.

Arieli, A., Sterkin, A., Grinvald, A., & Aertsen, A. (1996). Dynamics of ongoing activity: Explanation of the large variability in evoked cortical responses. *Science*, *273*(5283), 1868–1871.

Atallah, B. V., & Scanziani, M. (2009). Instantaneous modulation of gamma oscillation frequency by balancing excitation with inhibition. *Neuron*, *62*(4), 566–577.

Benigno, G. B., Budzinski, R. C., Davis, Z. W., Reynolds, J. H., & Muller, L. (2023). Waves traveling over a map of visual space can ignite short-term predictions of sensory input. *Nature Communications*, *14*(1), 3409.

Bringuier, V., Chavane, F., Glaeser, L., & Frégnac, Y. (1999). Horizontal propagation of visual activity in the synaptic integration field of area 17 neurons. *Science*, *283*(5402), 695–699.

Brunel, N. (2000). Dynamics of sparsely connected networks of excitatory and inhibitory spiking neurons. *Journal of computational neuroscience*, *8*, 183–208.

Brunel, N., & Wang, X.-J. (2003). What determines the frequency of fast network oscillations with irregular neural discharges? i. synaptic dynamics and excitation-inhibition balance. *Journal of neurophysiology*, *90*(1), 415–430.

Budzinski, R. C., Nguyen, T. T., Đoàn, J., Mináč, J., Sejnowski, T. J., & Muller, L. E. (2022). Geometry unites synchrony, chimeras, and waves in nonlinear oscillator networks. *Chaos: An Interdisciplinary Journal of Nonlinear Science*, *32*(3), 031104.

Chance, F. S., Abbott, L. F., & Reyes, A. D. (2002). Gain modulation from background synaptic input. *Neuron*, *35*(4), 773–782.

Churchland, M. M., Yu, B. M., Cunningham, J. P., Sugrue, L. P., Cohen, M. R., Corrado, G. S., Newsome, W. T., Clark, A. M., Hosseini, P., Scott, B. B., et al. (2010). Stimulus onset quenches neural variability: A widespread cortical phenomenon. *Nature neuroscience*, *13*(3), 369–378.

Crook, S. M., Ermentrout, G. B., Vanier, M. C., & Bower, J. M. (1997). The role of axonal delay in the synchronization of networks of coupled cortical oscillators. *Journal of computational neuroscience*, *4*, 161–172.

Davis, Z. W., Benigno, G. B., Fletterman, C., Desbordes, T., Steward, C., Sejnowski, T. J., H. Reynolds, J., & Muller, L. (2021). Spontaneous traveling waves naturally emerge from horizontal fiber time delays and travel through locally asynchronous-irregular states. *Nature Communications*, *12*(1), 6057.

Davis, Z. W., Muller, L., Martinez-Trujillo, J., Sejnowski, T., & Reynolds, J. H. (2020). Spontaneous travelling cortical waves gate perception in behaving primates. *Nature*, *587*(7834), 432–436.

Demas, J., Manley, J., Tejera, F., Barber, K., Kim, H., Traub, F. M., Chen, B., & Vaziri, A. (2021). High-speed, cortex-wide volumetric recording of neuroactivity at cellular resolution using light beads microscopy. *Nature Methods*, *18*(9), 1103–1111.

Denève, S., & Machens, C. K. (2016). Efficient codes and balanced networks. *Nature neuroscience*, *19*(3), 375–382.

Destexhe, A., & Contreras, D. (2006). Neuronal computations with stochastic network states. *Science*, *314*(5796), 85–90.

Destexhe, A., Contreras, D., & Steriade, M. (1999). Spatiotemporal analysis of local field potentials and unit discharges in cat cerebral cortex during natural wake and sleep states. *Journal of Neuroscience*, *19*(11), 4595–4608.

Destexhe, A., Rudolph, M., & Paré, D. (2003). The high-conductance state of neocortical neurons in vivo. *Nature reviews neuroscience*, *4*(9), 739–751.

El Boustani, S., Pospischil, M., Rudolph-Lilith, M., & Destexhe, A. (2007). Activated cortical states: Experiments, analyses and models. *Journal of Physiology-Paris*, *101*(1-3), 99–109.

Girard, P., Hupé, J., & Bullier, J. (2001). Feedforward and feedback connections between areas v1 and v2 of the monkey have similar rapid conduction velocities. *Journal of neurophysiology*, *85*(3), 1328–1331.

Golomb, D., & Ermentrout, G. B. (1999). Continuous and lurching traveling pulses in neuronal networks with delay and spatially decaying connectivity. *Proceedings of the National Academy of Sciences*, *96*(23), 13480–13485.

Golomb, D., & Ermentrout, G. B. (2000). Effects of delay on the type and velocity of travelling pulses in neuronal networks with spatially decaying connectivity. *Network: Computation in Neural Systems*, *11*(3), 221.

Gong, P., & van Leeuwen, C. (2009). Distributed dynamical computation in neural circuits with propagating coherent activity patterns. *PLoS Computational Biology*, *5*(12), e1000611.

González-Burgos, G., Barrionuevo, G., & Lewis, D. A. (2000). Horizontal synaptic connections in monkey prefrontal cortex: An in vitro electrophysiological study. *Cerebral Cortex*, *10*(1), 82–92.

Huang, C., Pouget, A., & Doiron, B. (2022). Internally generated population activity in cortical networks hinders information transmission. *Science Advances*, *8*(22), eabg5244.

Huang, C., Ruff, D. A., Pyle, R., Rosenbaum, R., Cohen, M. R., & Doiron, B. (2019). Circuit models of low-dimensional shared variability in cortical networks. *Neuron*, *101*(2), 337–348.

Hubel, D. H., & Wiesel, T. N. (1959). Receptive fields of single neurones in the cat's striate cortex. *The Journal of physiology*, *148*(3), 574.

Jun, J. J., Steinmetz, N. A., Siegle, J. H., Denman, D. J., Bauza, M., Barbarits, B., Lee, A. K., Anastassiou, C. A., Andrei, A., Aydın, Ç., et al. (2017). Fully integrated silicon probes for high-density recording of neural activity. *Nature*, *551*(7679), 232–236.

Keane, A., & Gong, P. (2015). Propagating waves can explain irregular neural dynamics. *Journal of Neuroscience*, *35*(4), 1591–1605.

Kenet, T., Bibitchkov, D., Tsodyks, M., Grinvald, A., & Arieli, A. (2003). Spontaneously emerging cortical representations of visual attributes. *Nature*, *425*(6961), 954–956.

Kriener, B., Helias, M., Aertsen, A., & Rotter, S. (2009). Correlations in spiking neuronal networks with distance dependent connections. *Journal of computational neuroscience*, *27*, 177–200.

Kriener, B., Helias, M., Rotter, S., Diesmann, M., & Einevoll, G. T. (2014). How pattern formation in ring networks of excitatory and inhibitory spiking neurons depends on the input current regime. *Frontiers in computational neuroscience*, *7*, 187.

Kumar, A., Rotter, S., & Aertsen, A. (2008). Conditions for propagating synchronous spiking and asynchronous firing rates in a cortical network model. *Journal of neuroscience*, *28*(20), 5268–5280.

Kumar, A., Schrader, S., Aertsen, A., & Rotter, S. (2008). The high-conductance state of cortical networks. *Neural computation*, *20*(1), 1–43.

Mainen, Z. F., & Sejnowski, T. J. (1995). Reliability of spike timing in neocortical neurons. *Science*, *268*(5216), 1503–1506.

Mehring, C., Hehl, U., Kubo, M., Diesmann, M., & Aertsen, A. (2003). Activity dynamics and propagation of synchronous spiking in locally connected random networks. *Biological cybernetics*, *88*(5), 395–408.

Morrison, A., Aertsen, A., & Diesmann, M. (2007). Spike-timing-dependent plasticity in balanced random networks. *Neural computation*, *19*(6), 1437–1467.

Muller, L., Mináč, J., & Nguyen, T. T. (2021). Algebraic approach to the kuramoto model. *Physical Review E*, *104*(2), L022201.

Muller, L., Reynaud, A., Chavane, F., & Destexhe, A. (2014). The stimulus-evoked population response in visual cortex of awake monkey is a propagating wave. *Nature communications*, *5*(1), 3675.

Nandy, A., Nassi, J. J., Jadi, M. P., & Reynolds, J. (2019). Optogenetically induced low-frequency correlations impair perception. *Elife*, *8*, e35123.

Osan, R., & Ermentrout, B. (2001). Two dimensional synaptically generated traveling waves in a theta-neuron neural network. *Neurocomputing*, *38*, 789–795.

Renart, A., De La Rocha, J., Bartho, P., Hollender, L., Parga, N., Reyes, A., & Harris, K. D. (2010). The asynchronous state in cortical circuits. *science*, *327*(5965), 587–590.

Roxin, A., Brunel, N., & Hansel, D. (2005). Role of delays in shaping spatiotemporal dynamics of neuronal activity in large networks. *Physical review letters*, *94*(23), 238103.

Roxin, A., Brunel, N., & Hansel, D. (2006). Rate models with delays and the dynamics of large networks of spiking neurons. *Progress of Theoretical Physics Supplement*, *161*, 68–85.

Sato, T. K., Nauhaus, I., & Carandini, M. (2012). Traveling waves in visual cortex. *Neuron*, *75*(2), 218–229.

Senk, J., Korvasová, K., Schuecker, J., Hagen, E., Tetzlaff, T., Diesmann, M., & Helias, M. (2020). Conditions for wave trains in spiking neural networks. *Physical review research*, *2*(2), 023174.

Shadlen, M. N., & Newsome, W. T. (1994). Noise, neural codes and cortical organization. *Current opinion in neurobiology*, *4*(4), 569–579.

Shadlen, M. N., & Newsome, W. T. (1998). The variable discharge of cortical neurons: Implications for connectivity, computation, and information coding. *Journal of neuroscience*, *18*(10), 3870–3896.

Stettler, D. D., Das, A., Bennett, J., & Gilbert, C. D. (2002). Lateral connectivity and contextual interactions in macaque primary visual cortex. *Neuron*, *36*(4), 739–750.

Tsodyks, M., Kenet, T., Grinvald, A., & Arieli, A. (1999). Linking spontaneous activity of single cortical neurons and the underlying functional architecture. *Science*, *286*(5446), 1943–1946.

Van Vreeswijk, C., & Sompolinsky, H. (1996). Chaos in neuronal networks with balanced excitatory and inhibitory activity. *Science*, *274*(5293), 1724–1726.

Vogels, T. P., & Abbott, L. F. (2005). Signal propagation and logic gating in networks of integrate-and-fire neurons. *Journal of neuroscience*, *25*(46), 10786–10795.

Zerlaut, Y., & Destexhe, A. (2017). Enhanced responsiveness and low-level awareness in stochastic network states. *Neuron*, *94*(5), 1002–1009.